SQUID Instruments and Applications

R. L. Fagaly
Tristan Technologies
San Diego, CA 92121 USA

Abstract

Superconducting quantum interference devices (SQUIDs) have been a key factor in the development and commercialization of ultrasensitive electric and magnetic measurement systems. In many cases, SQUID instrumentation offers the ability to make measurements where no other methodology is possible. We review the main aspects of designing, fabricating and operating a number of SQUID measurement systems.

A qualitative description of the operating principles of SQUID sensors and the properties of materials used to fabricate SQUID sensors is presented. The difference between low and high temperature SQUIDs and their suitability for specific applications is discussed.

Although SQUID electronics have the capability to operate well above 1 MHz, most applications tend to be at lower frequencies. Specific examples of input circuits, detection coil configuration for different applications and environments along with expected performance are described. In particular, anticipated signal strength, magnetic field environment (applied field and external noise) and cryogenic requirements are discussed. Finally, a variety of applications with specific examples in the areas of electromagnetic, material property, non-destructive test and evaluation, geophysical and biomedical measurements are reviewed.

1 INTRODUCTION

There are many ways to measure magnetic fields and properties. Sensing methods have been based on the use of induction coils, fluxgate magnetometers, magnetoresistive and Hall effect magnetometers, magneto-optical magnetometers and optically pumped magnetometers. Sensitivities range from microtesla to picotesla levels. Reference [1] gives an overview of the principles and design of magnetic sensors and magnetometers. The most sensitive magnetic flux detector is the Superconducting Quantum Interference Device (SQUID). This device, operating at cryogenic temperatures with quantum limited sensitivity, has demonstrated field resolution at the 10^{-17} tesla level.

1.1 Superconductivity

At temperatures approaching absolute zero, certain materials undergo a transition to what is known as the superconducting state. In 1911, Kamerlingh-Onnes [2] discovered that the resistance of mercury when cooled below 4.2 Kelvin (K), dropped to an immeasurably small value (Figure 1a).

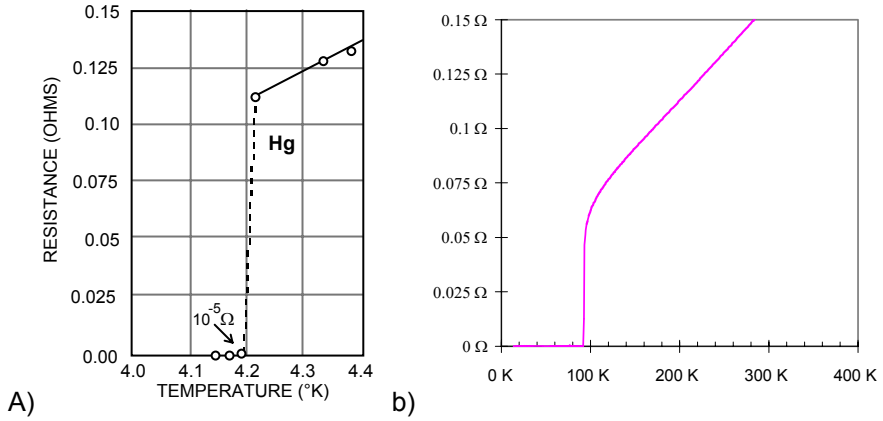

Figure 1 Resistance of mercury (a) (After: [2]) and $YBa_2Cu_3O_{7-\delta}$ (b) vs. absolute temperature.

This transition from normal resistance to resistanceless behavior takes place over a narrow temperature range—about 0.001 K for pure, strain free metals and a degree or more for alloys and ceramics. Below this temperature, known as the transition temperature (T_c), the material is characterized by a complete lack of electrical resistance. Subsequent investigations indicate a large number of materials undergo a similar superconducting transition. According to the Bardeen-Cooper-Schriefer (BCS) theory [3], the mechanism that permits superconductivity is the phonon exchange between paired electrons (Cooper pairs). The average distance between the electron pairs is the coherence length ξ. Electrons can exchange partners and they can be depaired by thermal (critical temperature - T_c), kinetic (critical current density - J_c) or magnetic (critical field - H_c) interactions. The temperature, current density and magnetic field under which the particular material is superconducting form the so-called phase space. In 1986, Bednorz and Müller [4] discovered a new class of ceramic oxides that became superconducting near 30 K—significantly warmer than any previously known superconductor. Since then, newer materials have been developed with the superconducting transition temperatures above 130 kelvin, well above the boiling point of liquid nitrogen. $YBa_2Cu_3O_{7-\delta}$ (Figure 1b) with $T_c > 90$ K (often referred to as YBCO is the most commonly used superconducting ceramic oxide. To distinguish between the types of materials used in making SQUID sensors, we denote the older metallic superconductors that typically operate at liquid helium temperatures (4.2 K) as Low Temperature Superconductors (LTS) and the newer materials that can operate at liquid nitrogen temperatures (77 K) as High Temperature Superconductors (HTS).

1.2 Meissner Effect

An interesting property of the superconducting state is observed if a superconductor is put in a magnetic field and then cooled below its transition temperature [5]. In the normal state, magnetic flux lines can penetrate through the material (Figure 2a). In the superconducting state, flux lines can not exist. This is a consequence of Maxwell's equations where an electric field gradient can not exist inside a superconductor. As the material becomes superconducting, the magnetic flux is expelled (Figure 2b). If the superconducting material forms a ring, the flux interior to the ring is trapped when the ring becomes superconducting (Figure 2c).

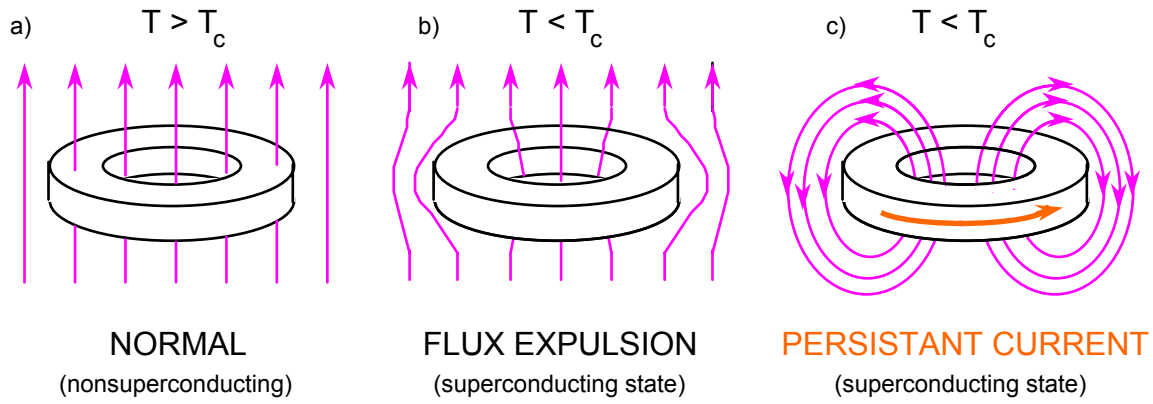

Figure 2 Meissner effect in a superconducting ring cooled in an externally applied magnetic field.

If the magnetic field is turned off, a current is induced that circulates around the ring keeping the magnetic flux ($\Phi = \int BdA$) inside constant (Figure 2d). Because of the electrical resistance, the current in a ring made of a normal (non-superconducting) metal will quickly decay. The current decay is exponential with a time constant that is related to the resistance (R) and inductance (L) of the ring, $I(t) = I_o\, e^{-tR/L}$. In a superconducting ring (R = 0), there would be no decay of the current and a persistent current ($I = -\Phi/L$) is established. The current continues to circulate as long as the ring is kept below T_c. Superconducting rings of tin have been made to carry circulating dc currents for a period much greater than a year, disconnected from any power source, without any measurable decrease in current [6]. This is equivalent to saying that the resistivity of superconducting tin is at least 17 orders of magnitude less than that of room temperature copper.

1.3 Flux Quantization

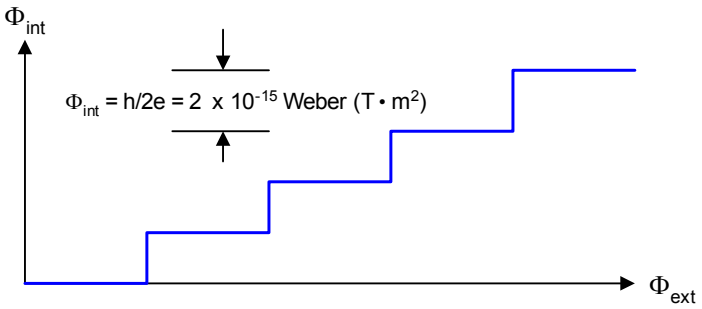

Figure 3 Flux Quantization

As long as the current persists, the magnetic flux remains "trapped". This trapped flux has some very unusual properties. First, one cannot change the level of magnetic flux in the ring in a continuous manner. One can only trap discrete levels of the magnetic flux (Figure 3). In other words, the magnetic flux is quantized [7] and exists only in multiples of the flux quantum (Φ_o = 2.068 x 10^{-15} Webers; 1 Wb/m^2 = 1 Tesla). Equivalently, for a ring with an area of 1 cm^2, the field inside the ring can only exist in discrete steps of 2.068 x 10^{-11} Tesla.

1.4 The Josephson Effect

For a loop of superconducting wire interrupted by a normal, resistive, region, one would expect it to behave the same as a continuous loop of normal metal, *i.e.*, a current flowing in the loop

would quickly decay (Figure 4a). In 1964, Josephson [8] predicted the possibility of electrons tunneling from one superconducting region to another that had been separated by a resistive (insulating) barrier, often referred to as a "weak link" (Figure 4b). For distances less than the coherence length (ξ) of the superconducting material (Table 1) and currents less than a critical current I_c that is characteristic of the weak link, a current can penetrate the resistive barrier with no voltage drop (Figure 4c).

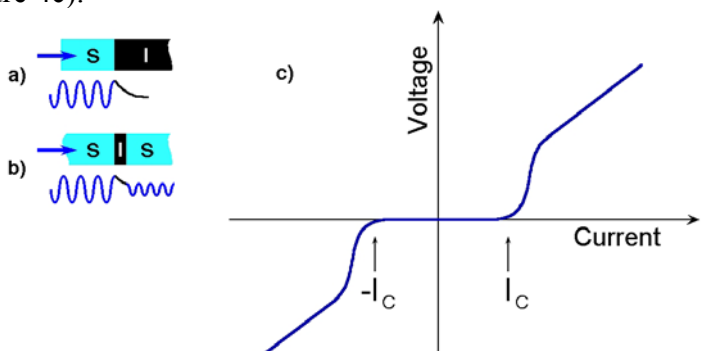

Figure 4 a) Quantum mechanical wave function of a superconducting current penetrating a normal region, showing the attenuation of the wave function as it penetrates an insulating layer b) Quantum mechanical wave function penetrating a thin normal region separating two superconducting regions; c) Current vs. Voltage curve of a Josephson tunnel junction. In an ideal Josephson junction, the transition from resistive to superconducting behavior would be a sharp vertical transition, rather than the real-world curved transition shown.

Obviously, if the Josephson junction is interrupting a superconducting loop, the amplitude of the wave function will be the same on both sides of the barrier.

There are many ways to make a weak link. The junction can be an insulating (Superconducting-Insulator-Superconducting or SIS) barrier such as a point contact where the barrier is NbO_x (Figure 5a), a normal metal (Superconducting-Normal-Superconducting or SNS) or a microbridge (Figure 5b). Present day LTS devices use tunnel junction weak links (Figure 5c). HTS devices use either intrinsic (bicrystal-Figure 5d or step edge grain boundary-Figure 5e) junctions or extrinsic (step edge SNS-Figure 5f or ramp edge-Figure 5g) structures.

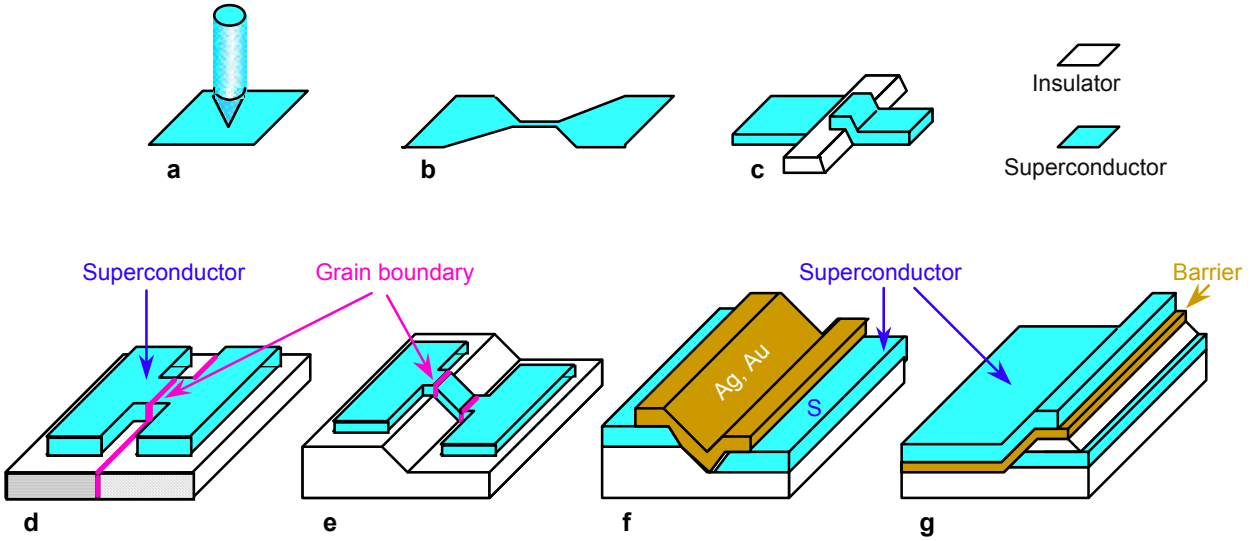

Figure 5 Different types of Josephson junctions, (a) point contact, (b) microbridge, also known as a Dayem bridge, (c) thin-film tunnel junction (the barrier can either be an insulating (SIS) or normal metal (SNS) material,

(d) bicrystal, (e) step edge grain boundary, (f) step edge superconductor-normal-superconductor, (g) ramp edge superconductor-normal-superconductor with a $PrBa_2Cu_3O_{7-\delta}$ barrier. after [16]

Bicrystal (Figure 5d) and ramp edge (Figure 5g) junctions have become popular in commercial HTS devices. This is because ramp edge junctions have a larger coherence length along the a-b plane; have good control of I_c by relatively thick barrier (which gives good reproducibility and stability; can be arbitrary placed on the substrate and used for complex circuits; and can operate in higher fields [9] because they are shielded by a top superconducting electrode. Bicrystal junctions are high ohmic devices (good for SQUIDs and microwave detectors); have good control of I_c by misorientation angle (good reproducibility and stability); like ramp edge junctions have a larger coherence length along the a-b plans and most importantly, are relatively simple to fabricate — only one HTS layer and one lithography stage is needed. Because of the higher quality and reproducibility combined with a relatively easy technology, these junction types have become most studied and better developed.

The next popular HTS junction types are the step edge (Figure 5e) junctions (cheaper than bicrystal ones, but quality and reproducibility is usually poorer) and step edge junctions with a normal metal shunt (better reproducibility for the shunt resistance (R_n), but R_n and I_cR_n are usually too low for SQUID operation).

1.5 Superconducting Quantum Interference Devices

The term SQUID is an acronym for a **S**uperconducting **QU**antum **I**nterference **D**evice that uses Josephson effect phenomena to measure extremely small variations in magnetic flux. Typically, a SQUID is a ring of superconductor interrupted by one or more Josephson junctions (Figure 6).

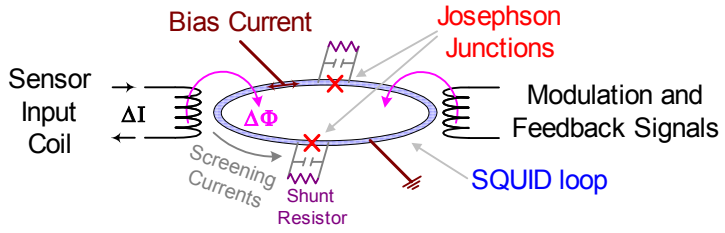

Figure 6 Dual junction (dc) SQUID loop. The capacitor represents the self-capacitance of the junction.

A bias current (I_b) is applied (2 I_b in the case of a dc SQUID) putting the operational point on the IV curve (Figure 7a) midway between superconducting and resistive behavior. Shunt resistors are used to prevent hysteretic behavior in the I-V curve [10]. Inductively coupling magnetic flux into the SQUID loop creates screening currents ($I_{loop} = \Phi_{loop}/L_{loop}$) that will increase or decrease I_c, depending on the direction of the induced flux.

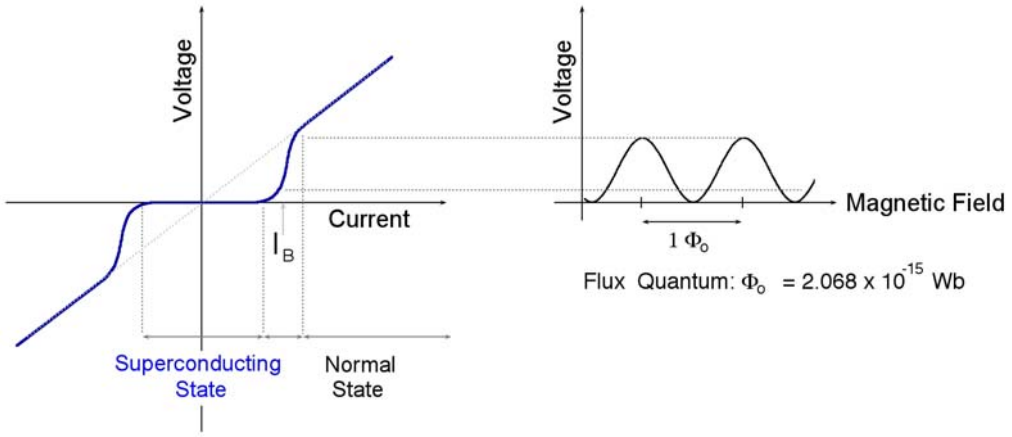

Figure 7a: bias point (I_b) for Josephson junction 7b: Voltage vs. externally applied flux at constant bias current

Fixing the current (I_b) at a slightly higher value than I_c, when an external magnetic flux ($\Phi_{ext} = B_{ext} A$) is coupled into the Josephson loop, the voltage drop across the Josephson Junction will change. As the external flux increases (or decreases), the voltage will change in a periodic manner with the period being that of the flux quantum, Φ_o (Figure 7b). Monitoring the change in voltage allows determination of the magnetic flux that has been coupled into the SQUID loop. By using external feedback (§3.1.1), it is possible to "lock" the SQUID at a unique point on the V-Φ_o curve; the feedback current (coupled into the SQUID loop-Figure 6) is then a measure of the externally applied flux. SQUIDs are normally operated at the steepest part of the V-Φ_o curve (where $\partial V/\partial \Phi$ is a maximum).

There is also the need for the feedback electronics to be able to track large changes in applied fields. For signal changes larger than $\Phi_o/4$, the electronics need to be able to apply negative feedback fast enough to keep the voltage at the operating or "lock" point. If the electronics can not change feedback current (slew) fast enough, it is possible that they could end up at a different point on the V-Φ_o curve (same V, different Φ_o). If flux jumping occurs, it may be necessary to go to faster electronics or limit the dynamic range (or bandwidth) of the input signal (source).

The theory of different types of SQUIDs is described in detail in the literature [11, 12, 13, 14]. SQUIDs are operated as either rf or dc SQUIDs. The prefix rf or dc refers to whether the Josephson junction(s) is biased with an alternating current (rf) or a dc current. Due to their lower noise (*c.f.*, §3.3), nearly all commercial SQUIDs are dc SQUIDs. As seen in Figure 6, flux is normally (inductively) coupled into the SQUID loop via an input coil which connects the SQUID to the experiment. Because the input coil is superconducting, its impedance is purely inductive. HTS SQUIDs either have the input coil as part of the Josephson loop or inductively coupled (via a flip-chip) to the Josephson loop.

2 SQUID SENSORS

There are fundamental differences between low and high temperature superconductors. LTS materials are metallic (although some non-metallic and organic compounds have been found to be superconducting at liquid helium temperatures, none have been fabricated into SQUIDs), isotropic and have coherence lengths (ξ) that are tens to hundreds of interatomic distances. HTS materials are ceramics, brittle, anisotropic (and with the exception of MgB_2) essentially planar and have coherence lengths in the c direction (perpendicular to the a-b plane) that are

significantly smaller (Table 1). Not only is there a temperature limitation to superconductivity, there is a field limitation. The material remains in the superconducting state below a critical field $H_c(T) = H_{c0} [1 - (T/T_c)^2]$ where H_{c0} is the critical field at T = 0. Type II superconductors have two critical fields, H_{c1} below which the material acts as a type I superconductor and H_{c2}, the upper limit in the type II (mixed) state

Table 1 Properties of superconducting materials

Material	T_c (K)	H_{c0} (tesla)	H_{c1} (tesla)	H_{c2} (tesla)	ξ_0 (nm)
LTS					
Lead	7.193	0.0803	-	-	90
Mercury	4.153	0.0412			
Niobium	9.25	-	0.198	0.268	40
NbTi	9.50	-		15	4
Nb_3Sn	18.1	-		24.5	3
HTS		H_{c1} (tesla)	H_{c2} (tesla)	ξ_{ab} (nm)	ξ_c (nm)
$Ba_{0.6}K_{0.4}BiO_3$	30				
MgB_2	39		18	6.5	2.5
$YBa_2Cu_3O_{7-\delta}$	95			4	0.7
$Bi_2Sr_2Ca_2Cu_2O_{10}$	110			4.5	0.2
$Tl_2Bi_2Ca_2Cu_3O_{10}$	125				
$HgBa_2Ca_2Cu_3O_{8+\delta}$	134				

2.1 Materials

Materials (typically pure metallic elements such as Hg or Pb) that totally exclude flux inside a superconductor (up to a well-defined transition temperature T_c) are referred to as type I superconductors (Figure 3a). Materials that exhibit a partial Meissner effect are referred to as type II superconductors (Figure 3b).

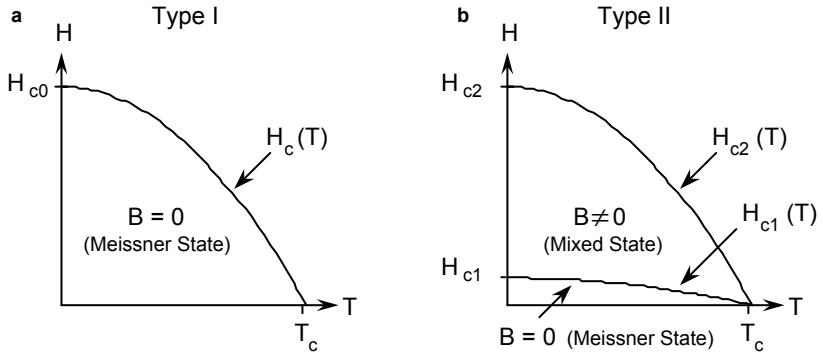

Figure 8 The H -T phase space for (a) type I and (b) type II superconductors

Below a lower critical field H_{c1}, they act as type I superconductors. Above H_{c1}, the material is (incompletely) threaded by flux lines and the material can be considered to be in a vortex state [12]. The higher the applied field, the greater number of allowed flux lines until the upper critical field H_{c2} is reached, where the entire material transitions to the normal state. Type II superconductors (*e.g.*, NbTi and Nb_3Sn) tend to be alloys or transition metals with high electrical resistivity in the normal state. All HTS materials are type II superconductors. High field superconducting magnets are fabricated from Type II materials.

LTS devices have significant advantages and one disadvantage—operating temperature—over HTS devices. Because LTS materials are isotropic and have long coherence lengths (Table 1) relative to their interatomic distances, it is possible to fabricate devices with three dimensional structures. This allows crossovers and multi-layer structures that permit higher sensitivity, *i.e.*, the ability to make multi-turn than single turn devices. HTS crossovers (needed for multi-turn coils) require larger dimensions than the coherence length of YBCO in the c-direction. The effect is that a HTS crossover acts as a Josephson or insulating junction with the addition of significant $1/f$ noise (*c.f.*, §3.5). The associated flux creep that can occur (particularly in HTS materials) by operating in the mixed (vortex) state can lead to non-linearity or hysteretic effects. While their pinning energies are somewhat lower than YBCO, bismuth and thallium compounds seem to have much lower densities of pinning sites [15]. As a result, the flux creep (and its associated resistivity) is considerably higher. Because of this, most HTS SQUIDs are fabricated from YBCO because of its sufficiently strong (and intrinsic) flux pinning at 77 K. By operating at lower temperatures (20 - 30 K), it is possible to freeze out the hysteretic effects seen in bismuth and thallium devices at 77 K, but because of the convenience of liquid nitrogen as a cryogen, all commercial HTS SQUIDs are fabricated using YBCO as the superconductor.

A significant difference between LTS and HTS materials is that LTS materials (*e.g.*, NbTi) are ductile and—in wire form—can be made into complex 3-dimensional structures such as axial gradiometers (*c.f.*, §4.5). Additionally, using NbTi (or Nb_3Sn) allows detection coils to be in high field regions, while the actual LTS SQUID sensor can be placed in a low field environment. Because of the inability to make a truly superconducting flexible 3-dimensional structure, axial HTS gradiometers are not possible (although thin film planar gradiometers are). Even if it was possible to make a separate HTS coils, the inability to make superconducting joints (or joints with contact resistances at the sub pΩ level) prevents true dc response in discrete element HTS circuits[15] (*i.e.*, the in-series resistance acts as a low frequency high pass filter).

Another advantage of LTS materials is that they are stable in air, whereas moisture degrades the HTS structure. Thus, passivation layers or overcoatings are required and add to the complexity of manufacture. Although LTS materials have superior properties, the ability to operate a device at liquid nitrogen rather than liquid helium temperatures gives HTS devices significant operational advantages and can not be discounted.

The barrier used for fabricating the weak link is critical. Early point contact LTS devices used a NbO layer formed by oxidizing the end of a Nb needle that was then pressed against a block of Nb (Figure 5a) . The first commercial dc SQUID used an amorphous SiO_2 barrier that allowed junctions with critical currents within a few percent to be easily fabricated. An unfortunate side effect was that the amorphous barrier had significant temperature dependent resistivity that caused frequency dependent noise (*c.f.*, §3.3.5). Present day LTS SQUIDs utilize AlO_x barriers with temperature independent critical currents. Reference [16] gives an excellent overview on HTS SQUIDs.

2.2 Flux Transformers

One problem with using just the SQUID loop as the detection coil is its small area and associated inductance ($\sim 10^{-10}$ H). Increasing the area of the loop or connecting a larger loop in series would increase sensitivity, but the impedance mismatch due to the increased inductance of the larger loop would negate much of the sensitivity gain. Most LTS SQUID sensors use a multilayer flux transformer to couple an externally detected flux into the SQUID loop (Figure 9).

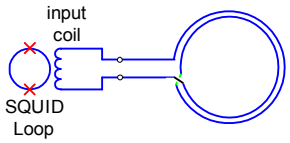

Figure 9 Flux Transformer for coupling external flux. Not to scale.

The flux transformer can either be fabricated on a separate substrate and placed directly over the SQUID loop (commonly known as a flip-chip) or it can be fabricated on the same substrate as the SQUID loop [17]. The input impedance of the flux transformer is much higher than that of the SQUID loop and typically ranges from 0.1 to 2 μH. The larger impedance of the input coil allows detection coils to be significantly larger than the SQUID loop. §4 discusses design of detection coils.

2.3 Fractional turn SQUIDs

Another way to increase sensitivity of a bare SQUID loop is to connect not just a single detection coil, but a number of coils, not in series (as is done in traditional multi-turn coils), but in parallel (Figure 10a). The critical concept is keeping the inductance of the SQUID loop itself very small, while having a large area for coupling to an external coil. This is because thermal noise puts an upper bound on the inductance of the loop itself. Referred to as a fractional turn (multi-loop) SQUID [18], this improves on sensitivity by reducing the input inductance by roughly N^2, where N is the number of turns in the SQUID loop.

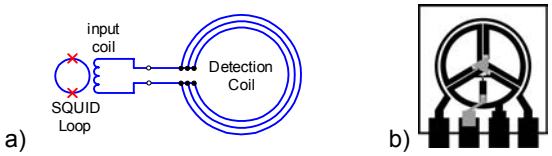

Figure 10 a) Schematic of fractional turn SQUID sensor. b) Fabricated device. The pads are for coupling in the bias and feedback currents. Fig. 10b courtesy of Hypres, Inc.

By directly coupling a fractional turn input coil, this allows a small diameter input coil to be fabricated that can match the input impedance of the SQUID loop. Devices with N = 3 (Figure 10b) to N = 16 have been fabricated with significantly reduced field noise. It should be noted that the effective measurement area of a fractional turn SQUID is less that its physical dimensions. This has an effect on the spatial resolution of fractional turn SQUIDs when used in magnetic microscopy (§9.2).

3 SQUID OPERATION AND PERFORMANCE

The major difference between rf and dc SQUIDs is that the dc SQUID may offer lower noise when compared to an rf SQUID. The cost of this increase in sensitivity can be the complexity of the electronics needed to operate a dc SQUID and the difficulty in fabricating two nearly identical Josephson junctions in a single device. From a historical viewpoint, although the LTS dc SQUID was the first type of SQUID magnetometer made, early LTS development was with rf SQUIDs. With modern thin film fabrication techniques and improvements in control electronics design, the dc SQUID offers clear advantages over the rf SQUID for many applications.

The system output voltage is the voltage drop across the feedback resistor in a negative feedback loop controlled by the SQUID electronics. The feedback signal is generated in response to changes in the output signal of the SQUID sensor. The output of the SQUID sensor is periodic in

the field coupled into the SQUID loop. Negative feedback (similar to a phase-locked loop technique) is used to maintain the system operating point at a particular (and arbitrary) flux quantum. When operated in this mode, the system is in a flux-locked loop (§3.1.1).

3.1 The rf SQUID

The rf SQUID [19] utilizes a single Josephson junction and flux is normally (inductively) coupled into the SQUID loop via an input coil which connects the SQUID to the experiment and an "rf" coil that is part of a high-Q resonant (tank) circuit to read out the current changes in the SQUID loop (Figure 11).

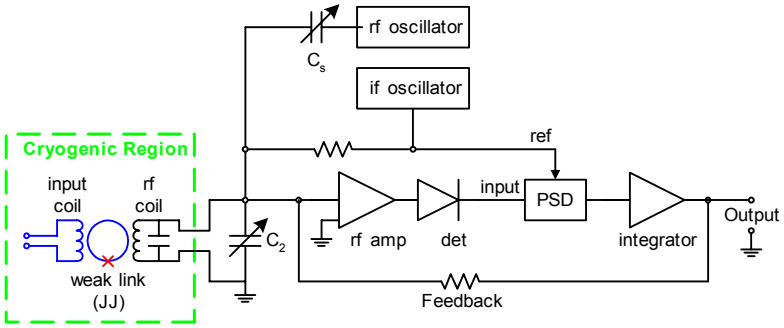

Figure 11 Block diagram of SQUID input and electronics for locked-loop operation of an rf SQUID. The input circuitry from the experiment (*e.g.*, a detection coil which would be connected to the input coil) is omitted for clarity.

This tuned circuit (in this example, operated at 19 MHz) is driven by a constant current radio-frequency oscillator that is weakly coupled to the SQUID loop. As the oscillator drive amplitude is increased, the (peak) detected output of the rf amplifier increases until a critical level is reached. That is, an increase in drive amplitude produces a very small increase in output. The rf drive is set so that the SQUID operates on this plateau, where the detected output depends on the current flowing in the input coil. Any changes in the input coil current will induce a change in the current flowing in the SQUID ring. This shielding current causes the total flux linking the SQUID ring to remain constant as long as the ring remains superconducting. Another contribution to the total flux in the SQUID (and to the shielding current) comes from the rf current in the (19 MHz) tuned circuit. Thus we can consider the shielding current to consist of an ac component and a dc component which biases the junction. When the amplitude of the ac component increases, the critical current of the weak link will be reached and a transition occurs changing the flux state of the SQUID by a single flux quantum. This transition temporarily reduces the level of oscillation in the rf coil, which then builds up again to its maximum value and the process repeats itself. Just after the transition, the weak link again becomes a superconductor and the shielding bias current due to the current in the input coil reestablishes itself to quantize the flux in the SQUID. When the rf oscillations have been reduced sufficiently, the Josephson junction will again be superconducting and the amplitude of the rf oscillations will begin to increase again. This behavior in the high-Q tank leads to the very characteristic triangles shown in Figure 12 (quite unlike the transfer functions seen with the dc SQUID).

If the dc current in the input coil is changed, the dc bias of the shielding current in the SQUID is changed so that the rf induced transition occurs at a different level of oscillation in the rf coil. The detected rf output is a periodic function of the applied flux (Figure 12).

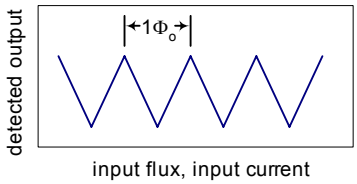

Figure 12 Triangle pattern showing detected output (rf) voltage vs. flux coupled into the SQUID

While it might be possible to measure the change in input coil current by simply counting the number of periods produced in the detected rf output, it may not be easy to tell if the external field is increasing or decreasing. In any case, the field resolution would be limited to 1 Φ_o.

3.1.1 The Flux-Locked Loop

A more commonly used mode of operation is a feedback scheme (Figure 11) which locks in on either a peak or a valley in the triangle pattern output from the rf peak detector (Figure 12). A feedback flux is applied to the SQUID through the rf coil that just cancels the change in flux from the input coil. This allows flux resolution to $\mu\Phi_o$ levels.

An audio frequency oscillator (IF OSCILLATOR in Figure 11) provides a reference for a phase-sensitive detector and also modulates the flux linking the SQUID due to the rf coil by an amount $\Phi_o/2$ (peak-to-peak). This low-frequency flux modulation, typically several tens of kHz, modulates the detected rf output. The amplitude of the rf modulation is zero when the total flux in the SQUID corresponds to a peak or valley (Figure 7b or Figure 12) and increases linearly to a maximum as the flux departs from an extremum one-fourth of the period ($\Phi_o/4$). A change in flux in the SQUID results in an output from the phase-sensitive detector, which is fed back through a resistor to the rf coil. The feedback current through the rf coil counters the flux change from the input coil, and maintains the flux in the SQUID locked at a value corresponding to an extremum in the rf response. This manner of operation is called a flux-locked loop.

It should be noted that the rf and input coils (Figure 11) are not wound around the SQUID loop, but inductively coupled to the SQUID loop. A minor advantage of the rf SQUID is that connections from the SQUID sensor to the room temperature electronics are simple—only a single coax or a single twisted pair of leads are needed.

3.2 The dc SQUID

The dc SQUID differs from the rf SQUID in the manner of biasing the Josephson junction and the number of junctions. Since there are two junctions, they need to be matched within a few %, as do the shunt resistors. It may be possible to operate SQUIDs with mismatched junctions, but performance (if any) would be significantly degraded. The ideal shunt resistor should have a temperature independent resistivity. The use of normal metal resistors such as Pd is preferred over amorphous materials or materials with superconducting transitions which would prevent operation of LTS devices below T_c (*e.g.*, 0.915 K in the case of a molybdenum shunt resistor).

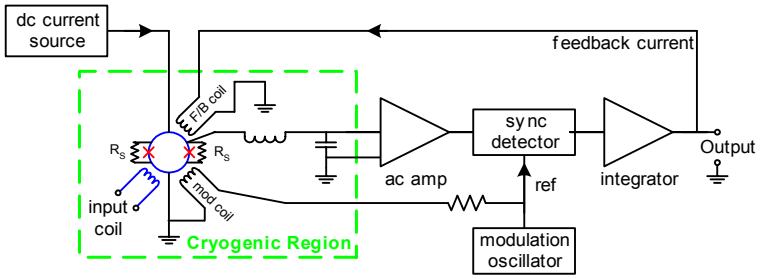

Figure 13 Block diagram of a typical dc SQUID. The detection coil (connected to the input coil) is omitted for clarity.

Figure 13 shows a schematic of a typical dc SQUID. Like the rf SQUID (Figure 11), the input, feedback and modulation coils are not wound around the SQUID loop, but inductively coupled to it. It is biased with a dc current approximately equal to twice I_c and develops a dc voltage across the junctions (and shunt resistors). A change in the magnetic flux applied through the SQUID loop induces a wave function phase change that enhances the current through one Josephson junction ($I_{total} = I_b + I_{screen} > I_c$) and reduces the current through the other ($I_{total} = I_b - I_{screen} < I_c$). As the external flux (Φ_{ext}) increases (or decreases), the voltage will change in a periodic manner with the period being that of the flux quantum, Φ_o (Figure 7b). The voltage, which is periodic in Φ_o, is used to provide a feedback current that nulls the flux penetrating the SQUID loop. Like the rf SQUID, this feedback current (presented as a voltage at the output) is a direct measure of changes in flux applied to the SQUID. Unlike the rf SQUID (Figure 12), the V-Φ curve is sinusoidal in nature. Additional details on the operation of dc SQUIDs may be found in reference [20]. The dc SQUID typically requires at least four pair of leads (bias, modulation, signal, feedback) between the SQUID and its electronics. A heater circuit (to momentarily drive the temperature of the SQUID above T_c) is useful to remove trapped flux.

3.2.1 Alternate modulation schemes

The flux-to-voltage gain of the SQUID can be increased by shunting the device with a resistor in series with an inductor coupled mutually to the SQUID loop [21]. This additional positive feedback (APF) enhances the output voltage gain of the SQUID and enables the use of a direct read-out, circumventing the conventional modulation scheme and increasing the bandwidth more than one order of magnitude to above 3 MHz [22]. Reference [23] discusses APF and other concepts such as two-stage SQUIDs, SQUID series arrays, relaxation oscillation SQUIDs and digital SQUIDs that have been used for SQUID readouts.

3.3 Noise & Sensitivity

SQUID noise is often presented as the spectral density of the equivalent flux noise $S_\Phi(f)$ as a function of frequency or noise energy per unit bandwidth $E_N(f) = S_\Phi(f)/2L$ where L is the inductance of the input coil. To allow devices with differing input inductances to be directly compared, the sensitivity of SQUID devices is best discussed in terms of the energy sensitivity:

$$E_N = L_{input} I_N^2 = \frac{\Phi_N^2}{L_{input}} \qquad \text{Equation 1}$$

where L_{input} is the input inductance of the device, I_N is the current noise and Φ_N is the flux sensitivity. E_N is often expressed in terms of Planck's constant $h = 6.6 \times 10^{-34}$ J/Hz.

Noise characterization may also be presented as the spectral density of the equivalent flux noise $S_\Phi(f)$ as a function of frequency or noise energy per unit bandwidth $E_N(f) = S_\Phi(f)/2\,L$ where L is the inductance of the input coil. Figure 14 shows typical energy sensitivities for LTS and HTS SQUIDs. As can be seen, the noise can be described as the sum of frequency independent (white) and frequency dependent ($1/f$) terms.

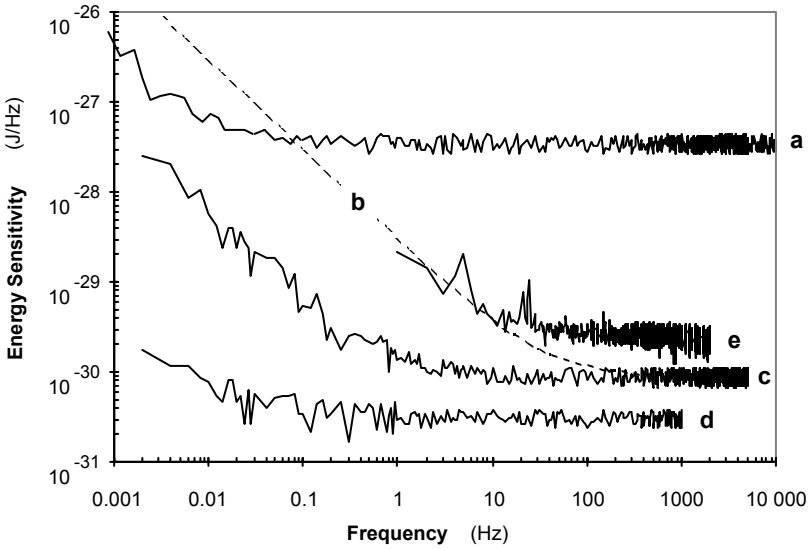

Figure 14 Energy sensitivity vs. frequency for a number of different SQUID devices. (a) is a LTS rf SQUID operated at a bias frequency of 19 MHz, (b) is a dc biased LTS dc SQUID with amorphous silicon barriers, (c) is (b) using ac biasing, (d) is a dc biased LTS dc SQUID with AlO_x barriers, and (e) is an ac biased HTS dc SQUID utilizing a ramp edge junction (Figure 5g). (a) – (d) were operated at 4.2 K, (e) was at 77 K.

Magnetometers are often discussed in terms of field sensitivity. However, because the field sensitivity is as much dependent on the geometry of the detection coil geometry (area, number of turns, etc.) as the SQUID itself, energy sensitivity allows comparison of devices independent of coil geometry. Calculation of magnetic field sensitivity is discussed in §4.4.

3.3.1 White Noise

3.3.1.1 rf SQUIDS

The rf SQUID can be modeled [24] as an ideal (lossless) parametric up-converter where $E_N \propto k_B T_N/hf_B$, where T_N is the noise temperature of the rf amplifier (Figure 11) and f_B is the bias frequency used to excite the tank circuit. This results in the current (or field) noise in rf SQUIDs is proportional to $1/\sqrt{f_B}$. For a LTS rf SQUID operating at 19 MHz [25], typical white noise is 10^{-28} J/Hz (Figure 14a). Increasing the bias frequency to 180 MHz [26] has been shown to reduce the white noise by a factor of three. As f_B increases, the complexity of the electronics also tends to increase. With the discovery of high temperature superconductivity, the first HTS SQUIDs were single junction rf SQUIDS. As it is not known (at least theoretically) if there is a fundamental limit to the white noise of rf SQUIDs, at 1 GHz, an rf HTS SQUID could be quieter than a dc HTS SQUID.

3.3.1.2 dc SQUIDs

The minimum noise energy (E_N) for a dc SQUID is given by [10]:

$$E_N \approx 4 k_B T \sqrt{\pi L_{loop} C} \qquad \text{Equation 2}$$

where k_B is Boltzmann's constant, T the temperature of the SQUID, L_{loop} is the inductance of the SQUID loop and C the self-capacitance of the junction. Substituting appropriate numbers indicates that E_N for a dc SQUID is on the order of $h/2$ and devices with these sensitivities have been constructed [27]. These extremely low noise levels are achieved by limiting dynamic range and avoiding feedback. The need for practical (useful) devices requires that feedback be used and that the SQUID electronics has a reasonable dynamic range. Commercially available dc SQUIDs have noise levels of 10^{-31} J/Hz.

3.3.2 Temperature Dependence

Due to the strong temperature dependence of superconducting properties, such as energy gap ($\Delta(T)$—the energy needed to decouple the paired electrons), critical current (I_c), surface resistivity (R_S), etc.—especially near T_c—we find that basic SQUID parameters such as bias and modulation drive will experience variations as a function of temperature.

The best noise performance is obtained when the SQUID is operated at or below ½T_c. A niobium LTS SQUID operating at 4.2 K has $T/T_c = 0.44$ while a YBCO SQUID at 77 K has $T/T_c = 0.83$. Operating at lower temperatures also means potentially lower noise (*c.f.*, eq. 2). A significant temperature variation may require retuning for optimum performance. A typical LTS SQUID (*e.g.*, Figure 14c and Figure 14d) will have a temperature variation of ~ 0.1 Φ_o/K, a HTS device (Figure 5f) has $d\Phi/dT \approx 0.015\ \Phi_o$/K. Because liquid cryogens are normally used to cool SQUID devices, ambient pressure and pressure variations can change the cryogen temperature with a commensurate change in SQUID operating parameters. For example, geophysical applications may require operation in deep mines, underwater or at altitude (airborne). A one torr pressure variation at 760 torr is equivalent to a 1.5 mK change in the temperature of a liquid helium bath and a 11 mK change in the temperature of a liquid nitrogen bath. Use of a closed-cycle refrigerator (cryocooler) can cause significant temperature variations (± ½ K at 1 Hz for a 4 kelvin G-M cycle cryocooler). A temperature controller or a large thermal mass (or both) may be needed to smooth out these variations.

3.3.3 Field Dependence

In normal operation, LTS SQUIDs are operated in the Earth's magnetic field (~50 μT) or lower environments. LTS experiments requiring operation in high fields usually employ coils that transport the measured flux or currents to the LTS SQUID sensor located in a low field region of the cryostat (typically less than 10 mT).

Because HTS coils are located on the same substrate as SQUID itself (or next to in the case of a flip-chip design [9]), the HTS SQUIDs are subjected to the environment being measured. It should be noted that some bicrystal SQUIDs have $I_c(H)$'s that oscillate with $\Phi_o/2$ [28]. Some HTS devices simply will not function in fields exceeding tens of μT. In addition, the decreased flux pinning in HTS devices at high fields results in reduced slew rates. The development of ramp edge junctions [9] has allowed HTS devices to operate in fields up to 0.1 T with white noise scaling as √H.

Both LTS and HTS devices should be operated in very stable fields. For LTS sensors, placing them inside a niobium can provides a highly stable local field environment. Since HTS devices

are usually configured for measuring external fields, it is not realistic to place a HTS SQUID in a HTS shield (unless it is large enough to encompass the entire object being measured [29]. Instead, attention must be paid to reducing external field influences on the SQUID sensor (*e.g.*, §4.2).

3.3.4 1/*f* Noise

Along with white noise, there exists a frequency dependent contribution that increases as the frequency decreases (Figure 14; note that the variation is $1/f$ in energy, not field). The onset of this "$1/f$" noise can be dependent on the ambient magnetic field when the SQUID sensor is cooled. Cooling the SQUID sensor in low ambient magnetic fields (less than 1 μT) may significantly improve the $1/f$ performance, particularly with HTS SQUIDs using grain boundary junctions. It should be noted that measurements of $1/f$ noise, usually taken at frequencies well below 1 Hz, are difficult. The SQUID sensor should be placed in a superconducting can which is itself inside mu-metal shielding. Care should be taken to eliminate any potential mechanical motion. As vibration often appears as a $1/f^2$ contribution, excessive low frequency noise may be identified by its spectral content.

3.3.5 Sources of 1/*f* noise

Thermally activated critical current fluctuations due to trapping and release of electrons in the barrier produce fluctuations in the (Josephson) energy gap - $\Delta(T)$ with variations in I_c. A large contribution to this noise in some dc SQUIDs can arise from the presence of the dc current bias. By chopping the dc bias (Figure 15) in combination with the conventional flux modulation techniques, it is possible to reduce this added $1/f$ noise.

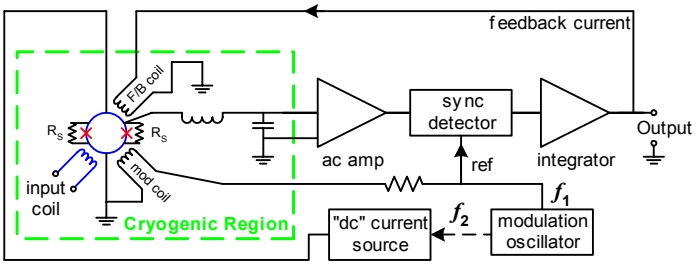

Figure 15: ac biasing. The modulation oscillator is used to chop the dc bias current at a frequency typically twice that of the modulation frequency (here $f_2 = 2\ f_1$).

This ac bias reversal approach [30], sometimes referred to as Dynabias, separates the original signal waveform from the noise associated with the dc bias, and can reduce $1/f$ noise at very low frequencies (Figure 14b & Figure 14c). As mentioned in §2.1, the first commercial dc SQUIDs exhibited excessive $1/f$ noise. The use of ac biasing lowered the $1/f$ knee by nearly two orders of magnitude. Present day LTS SQUIDs use AlO_x barriers that do not exhibit this excessive $1/f$ noise. HTS SQUIDs exhibit temperature dependant critical currents and flux noise that arises from motions of flux lines trapped in the HTS material. Both of these effects cause $1/f$ noise. The $1/f$ noise due to critical current variations can be significantly reduced by the use of ac biasing. Flux noise fluctuations have not been able to be reduced by any known modulation scheme.

The modulation signal can be distorted due to time delays, phase shifts and attenuation from circuit elements between the modulation oscillator and the modulation coil on the SQUID chip. This can increase noise and reduce bandwidth. Many commercial SQUID electronics have a

skew control that adds a small phase shifted signal at the same frequency as the modulation signal. This (skew) signal can be used to symmetrize the modulation signal presented at the SQUID loop improving system performance. It should be noted that bias reversal limits the maximum bandwidth to less than half the bias reversal frequency.

Temperature variations of the SQUID can also cause 1/*f* behavior (via $d\Phi/dT$, *c.f.*, §3.3.2) . If the SQUID is directly immersed in a liquid cryogen, stabilizing the bath temperature can be critical to minimizing temperature variations. Convection cells in the helium can be a major problem at low frequencies [31]. Movement of liquid cryogens can also induce temperature instabilities. One liquid nitrogen dewar was found to have a temperature stability best described as $\delta T = (1.9 \times + 1.9/T) \times 10^{-4}$ K/√Hz [32]

3.4 Control Electronics

One important factor of SQUID design is such that the feedback electronics be able to follow changes in the shielding currents. If the shielding current changes so fast that the flux in the SQUID loop changes by more than $\Phi_o/2$, it is possible that the feedback electronics will lag behind the rapidly changing flux. When the electronics finally "catch up", they can lock on an operating point (Figure 8) different from the original. In this case, the SQUID has "lost lock" because the SQUID has exceeded the maximum slew rate of the electronics. This places an upper limit on the bandwidth of the system. The typical bandwidth of commercially available SQUID systems is dc to 50+ kHz. Custom electronics have been built extending bandwidths above 3 MHz [22]. Typical slew rates for commercial electronics are in the range of 10^5 ~10^6 Φ_o/sec for a single pure frequency. Complex waveforms may generate intermodulation distortion that will have the effect of reducing the effective slew rate. It should be noted that slew rates for HTS devices can be significantly less (1/10 – 1/100) than theoretically possible. This may be due to flux motion and other limitations inherent to HTS materials.

Even though one may not need or want to observe rapidly changing signals, situations may arise when ambient noise (*e.g.,* 60 Hz) may determine the slew rate requirements of the system. To recover a signal from such interference, it is necessary that the system be able to track all signals present at the input, including the noise. When system response is sped up to handle very fast signals, sensitivity to rf interference and spurious transients is also increased. Since ability to remain locked while subjected to strong electrical transients is greatest when the maximum slew rate is limited (slow), while ability to track rapidly varying signals is greatest when the maximum slew rate is greatest (fast), it is desirable to be able to match the maximum slew-rate capability to the measuring situation. As a matter of convenience, many commercial SQUID systems offer user selectable slew rates along with high-pass and low-pass filters for noise reduction.

3.5 Limitations on SQUID Technology

When utilizing SQUID-based measurement systems and data reduction algorithms, it is important to bear in mind several fundamental limitations:

1) SQUIDs are sensitive to *relative* (field or current) changes only. This is a consequence of the fact that the output voltage of a SQUID is a periodic function (Figure 7b) of the flux penetrating the SQUID loop. The SQUID is "flux-locked" on an arbitrary point on the V–Φ curve and the SQUID output is sensitive to flux changes relative to this lock point.

2) If the signal changes faster than the feedback electronics can follow (*i.e.*, the slew rate is exceeded) and the total signal change exceeds ½ Φ_o, it is possible for the operating point to shift by one or more flux quanta (Figure 7). If high bandwidths are needed, it is possible to operate the electronics in a limited range mode where the raw output is amplified without use of a feedback signal. Although the SQUID has an intrinsic bandwidth of several GHz, when operated with standard flux-locked loop electronics using ac flux modulation, the maximum usable bandwidth of most commercially available electronics is typically 50 - 100 kHz.

3) Another limitation is the presence of $1/f$ noise. The use of ac biasing in HTS SQUIDs limits their maximum bandwidth to less than half the bias reversal frequency. If the bias reversal frequency is too high, noise can be induced due to voltage spikes in the transformer coupled preamplifier input circuit. Because of this, the maximum bandwidth of commercially available HTS SQUIDs is usually limited to ~50 kHz. If MHz bandwidths are required, the ac bias is not used; however, there will be excess noise below 1 kHz.

4) SQUID magnetometers are vector magnetometers. For a pure magnetometer operating in the Earth's magnetic field, a 180° rotation will sweep out a total field change of ~100 μT. If the magnetometer has a sensitivity of 10 fT/√Hz, tracking the total field change requires a dynamic range of 100 μT/10 fT = 200 dB, well beyond the capabilities of current electronics. In addition, the rotational speed must not cause the current flowing through the SQUID sensor to exceed its slew rate limitations. Pure gradiometers (§4.6) are insensitive to uniform fields and do not suffer this dynamic range limitation.

4 INPUT CIRCUITS

4.1 Packaging

Although it is possible to couple magnetic flux directly into the SQUID loop, environmental noise considerations (*c.f*, §6) make this difficult, if not impossible, in an unshielded environment. In addition, the area ($A = \pi r_{coil}^2$) of a typical SQUID loop is small (< 0.1 mm^2) and its resulting sensitivity to external flux changes ($\Delta\Phi = A \cdot \Delta B$) small. Although a larger loop diameter would increase the SQUID's sensitivity to external flux, it would also make it much more susceptible to environmental noise. For this reason, external flux is normally inductively coupled to LTS SQUID loops by a flux transformer. Because HTS devices have the detection coil grown on the same substrate, the Josephson loop is exposed to the environment being measured. This limits the ability of HTS devices to operate in high fields (*c.f*, §3.3.3).

The packaging of the sensor should be sufficiently rugged to allow use under adverse conditions. A niobium can will shield LTS devices from external fields > 20 mT. If an experiment requires high fields, it is desirable to use a magnet with a compensation coil that generates a null (< 200 gauss) field region. The SQUID sensor is placed there and connected to the experiment by twisted pair(s) of NbTi leads for fields < 10 T. Nb_3Sn leads may permit superconducting connections in fields above 20 T. When stored at room temperature, HTS devices require isolation from humid environments to prevent degradation of the YBCO film. Normally a surface passivation layer over the YBCO is combined with encapsulating the HTS SQUID in a gas filled sealed G-10 or plastic enclosure.

To improve immunity to external sources in LTS systems, it is advisable to run the connecting leads (between the detection coil(s) and SQUID input through superconducting tubes. While Nb tubing can be used, a much less expensive method is to remove the rosin core center of 60/40 lead-tin tubing. The hollow tubing can be used as a superconducting shield below 6 K. For HTS devices—if large coils are part of the device's structure—designing YBCO ground planes above and below the interconnects will help to reduce extraneous pickup (and improve balance (§4.6) in the case of planar gradiometers).

Today, SQUIDs are fabricated as planar devices rather than the point contacts (Figure 5a) or Dayem Bridges (Figure 5b) used to fabricate early rf SQUIDs. In this configuration, the superconducting loop, Josephson junctions and coils (input, feedback and modulation) are patterned on the same device. Multilayer deposition techniques are used (primarily in LTS devices) and coils are normally in the form of a square washer [17]. The planar configuration leads to quite small devices, occupying only a few mm^3 compared to 5+ cm^3 (1.2 cm diam. x 5 cm) for older toroidal rf SQUIDs [33]. Another advantage of the planar device is that it is possible to have the detection coils as part of the SQUID sensor, eliminating the need for separate (three-dimensional) detection coils. Such an integrated sensor can significantly reduce the complexity of multichannel systems.

4.2 External feedback

Normally, SQUID electronics utilize an internal feedback technique to cancel changes in magnetic flux. An alternate approach to feedback may be made by coupling the feedback signal to the input coil (Figure 16a) rather than to the Josephson loop. This can avoid large feedback currents (*e.g.*, due to 50 or 60 Hz) that would exceed I_c for the Josephson junction(s).

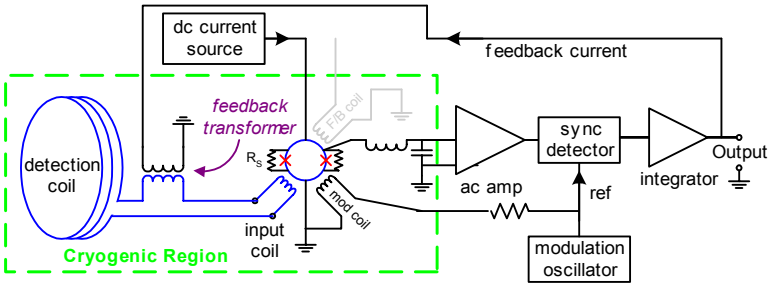

Figure 16 External feedback circuit. Note that the internal feedback circuitry (shown in Figure 13) is not used

A second method (Figure 17) uses an externally generated signal in addition to the SQUID feedback electronics. One example is a circuit to compensate for an external ac field being applied near the detection coil(s) in a susceptibility experiment.

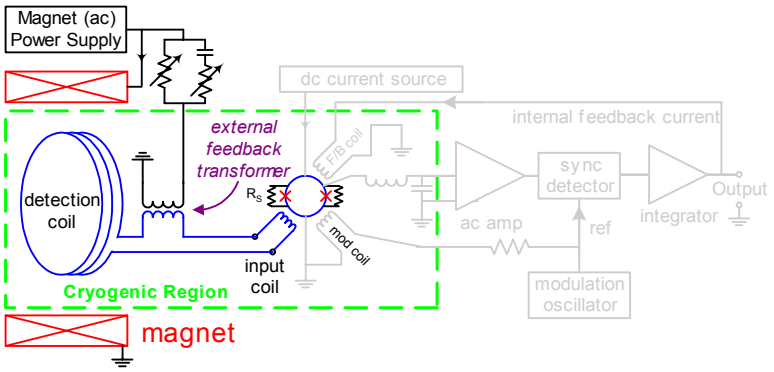

Figure 17 ac susceptibility system using external feedback. The external feedback signal is generated (in parallel to the internal feedback in this example) to the magnet power supply and then attenuated before being fed into the input circuit. The capacitive circuit element generates the quadrature signal.

Another variation is where a external feedback signal (for real-time noise reduction) is generated by the output of reference channels (§4.7). This method is normally used in parallel with internal feedback. When this technique is used, it may be necessary to null both the in-phase and quadrature feedback signals. This can be done manually or by computer control.

When calculating the sensitivity of the detection coil, the portion of the external feedback coil that is in series with the detection and input coils must be added to calculate the total inductance (*e.g.*, eq. 5). Care must be taken in constructing the external feedback coil and the leads that connect the coil. The major consideration is to avoid the introduction of potential rf interference into the external feedback coil. Shielding the leads, magnetically isolating the external feedback coil from the signal (or potential noise sources) and proper attention to grounding will reduce the chances of problems.

4.3 The SQUID as a Black Box

Whether an rf or dc SQUID, a SQUID system can be considered as a black box that acts like a current (or flux)-to-voltage amplifier with extremely high gain. In addition, it offers extremely low noise, high dynamic range (> 140 dB), excellent linearity (> 1:10^7) and a wide bandwidth that can extend down to dc. A SQUID can also be used as a post-amplifier stage [34] offering superior performance to conventional field effect transistors at frequencies as high as 500 MHz.

Conceptually, the easiest input circuit to consider for detecting changes in magnetic fields is that of a SQUID sensor connected to a simple superconducting coil (Figure 18).

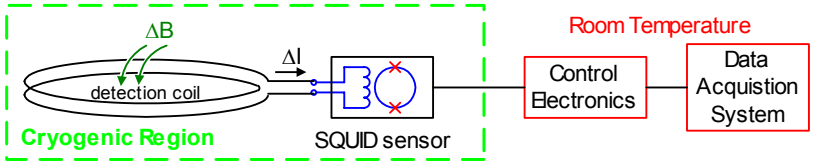

Figure 18 Schematic diagram of typical SQUID input circuit

Since the total flux in a superconducting loop is conserved, any change in external field through the signal coil will induce a current in the flux transformer which must satisfy:

$$\Delta\Phi = NA\Delta B = (L_{coil} + L_{input})\Delta I \qquad \text{Equation 3}$$

where ΔB is the change in applied field; N, A, and L_{coil} are the number of turns, area, and inductance of the detection coil; L_{input} is the inductance of the SQUID input coil; and ΔI is the change in current in the superconducting circuit. If the lead inductance is not negligible, it must be added to L_{coil} and L_{input}. Typically, twisted pair 0.005" NbTi wire has $L_{lead} \approx 0.3$ μH/meter.

4.4 Sensitivity

Maximum sensitivity is almost never the optimum sensitivity. Nevertheless, an understanding of the techniques used to maximize sensitivity is essential to any discussion of optimum sensitivity. Since the SQUID system has an output that is proportional to the input current, maximum sensitivity is obtained by using the input circuit that provides the maximum current into the SQUID and satisfies all other constraints of the experimental apparatus.

A common constraint is the physical size of the detection coil. As is seen in eqs. (3) and (4), it is clear that maximum sensitivity to uniform fields is obtained with an infinitely large coil. Infinitely large coils fit quite nicely into dewars with infinitely large necks, but they have the serious disadvantage of boiling off liquid cryogens at an infinitely fast rate. If ultimate sensitivity is needed, common practice would be to build the largest diameter detection coil that will fit in a physically realistic dewar neck.

Another constraint on coil design is spatial resolution which is dependent on the nature of the source, the geometry of the detection coil and the distance between the coil and the source. If nearby objects are to be measured (*e.g.*, biomagnetism or magnetic microscopy) then spatial resolution may be more important than absolute sensitivity.

In the near field region, where the distance to the detection coil is less than a coil diameter from the detection coil(s), the spatial resolution can be better than $1/10^{th}$ the coil diameter. Multiple or higher order (quadruple, etc.) sources may have spatial resolution on the order of the coil diameter. One rule of thumb is not to have the coil diameter significantly less than the distance between the coil and the source. This distance includes the tail spacing (gap) of the dewar (Figure 25) used to provide the cryogenic environment. Application specific analyses are given in §9.2 and §10.2.

In the far field approximation, where the distance from the detection coil is many coil diameters, spatial resolution may be multiples of the coil diameter. In that situation, larger coils are

recommended. However, it makes no sense to design coils for significantly higher sensitivity than environmental constraints (noise) permit.

To calculate the sensitivity and noise level of a simple detection coil system, the inductance of the detection coil must be known. The inductance of a flat, tightly wound, circular multi-turn loop of superconducting wire is given (in MKS units) by [35]:

$$L = 0.4\times10^{-6}\,N^2\,\pi\,r\left[\log_e\left(\frac{8\,r_{coil}}{r_{wire}}\right)-2\right] \qquad \text{Equation 4}$$

where r_{coil} is the radius of the detection coil and r_{wire} is the radius of the (superconducting) wire. Knowing the coil inductance L_{coil}, we can rewrite eq. (4) as

$$\Delta B = (L_{coil} + L_{input})\Delta I/NA \qquad \text{Equation 5}$$

Since the SQUID system has an output proportional to the input current, maximum sensitivity is obtained by using the input circuit that provides the maximum current into the SQUID and satisfies all other constraints of the experimental apparatus. For a pure magnetometer of a given diameter, the maximum sensitivity will occur when the impedance of the detection coil matches that of the SQUID sensor ($L_{coil} = L_{input}$).

Much higher sensitivity (10^{-17} tesla/√Hz) in a limited bandwidth (100 Hz in this case) has been achieved by incorporating an rf SQUID (Figure 14a) into a parametric amplifier circuit [36]. Substituting a present day dc SQUID sensor could yield a sensitivity of $< 3 \times 10^{-18}$ tesla/√Hz

4.5 Detection Coils

Several factors affect the design of the detection coils [37]. These include the desired sensitivity of the system, the size and location of the magnetic field source and the need to match the inductance of the detection coil to that of the SQUID. The ability to separate field patterns caused by sources at different locations and strengths requires a good signal-to-noise ratio. At the same time, one has to find the coil configuration that gives the best spatial resolution. Unfortunately, these two tasks are not independent. For example, increasing the signal coil diameter improves field sensitivity, but sacrifices spatial resolution. In practice, system design is restricted by several constraints: the impedance and noise of the SQUID sensors, the size of the dewar, the number of channels, along with the distribution and strength of noise sources.

It is extremely important for dc response that the detection coil(s) be superconducting. Resistance in the detection circuit has two effects: 1) attenuating the signal, and 2) adding Nyquist noise. Resistive attenuation is important only below a frequency f_o, such that the resistive impedance is equal to the sum of the inductive impedances in the loop (*e.g.*, $f_o \approx R/L_{tot}$, where L_{tot} is the total inductive impedance of the loop). Resistive noise is only important if it becomes comparable to other noise sources or the signal ($<10^{-30}$ J/Hz for biomagnetism, $<10^{-26}$ J/Hz for geophysics). For a SQUID with $E_N \sim 10^{-30}$ J/Hz, the total resistance of the circuit, *including any joints*, must be less than 10^{-13} Ω [15]. Thus it is very important that all solder joints, press-fits or connections have as low a joint resistance as possible.

Figure 19 displays a variety of detection coils. The magnetometer (Figure 19a) responds to the changes in the field penetrating the coil. More complicated coil configurations provide the

advantage of discriminating against unwanted background fields from distant sources while retaining sensitivity to nearby sources.

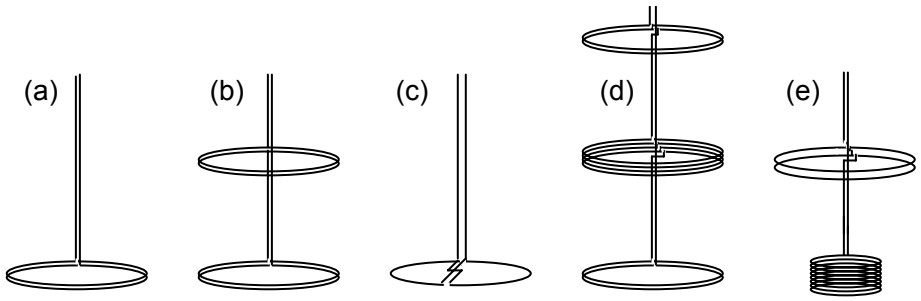

Figure 19 a) magnetometer b) 1st derivative gradiometer c) planar gradiometer d) 2nd derivative gradiometer e) 1st derivative asymmetric gradiometer

Because of the present inability to make flexible (*i.e.*, small bending radius) wire or make true superconducting joints in HTS materials, commercially available HTS devices are currently in the form of magnetic sensing rather than current sensing devices.

4.6 Gradiometers

Magnetometers are extremely sensitive to the outside environment. This may be acceptable if one is measuring ambient fields. If what is to be measured is close to the detection coil and weak, outside interference may prevent measurements at SQUID sensitivities. If the measurement is of a magnetic source close to the detection coil, a gradiometer coil may be preferred. Since $B_{dipole} \propto 1/z^3$, where z is the distance beneath the coil, it follows that the field from a distant source is relatively uniform in direction and magnitude at the sensor. If we connect in series two identical and exactly parallel loops wound in opposite senses, separated by a distance b (the baseline), we obtain a coil (Figure 19b) that will reject uniform fields.

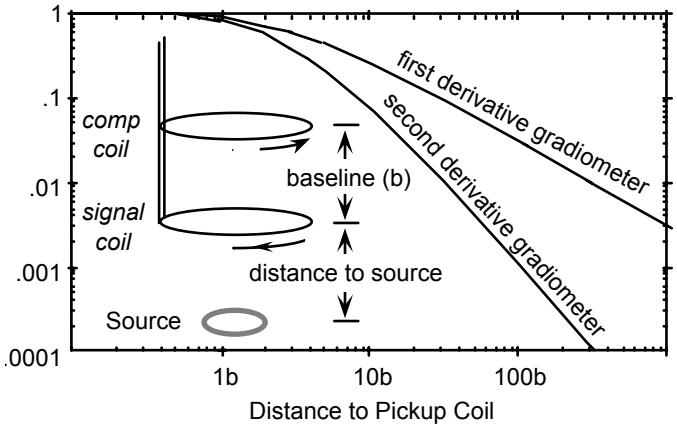

Figure 20 Response of gradient coils relative to magnetometer response ($1/z^3$ suppressed)

Since the response of a single coil to a magnetic dipole goes as $1/z^3$, an object that is much closer to one coil than the other will couple better to the closer coil than the more distant. Sources that are relatively distant will couple equally into both coils. For objects that are closer than 0.3 b, the gradiometer acts as a pure magnetometer, while rejecting more than 99% of the influence of objects more than 300 b distant (Figure 20). In essence, the gradiometer acts as a compensated magnetometer. It is possible to use two gradiometers connected in series opposition (Figure 19d)

to further minimize the response of the system to distant sources. This can be extended to higher orders by connecting in series opposition two 2nd order gradiometers, etc. Doing so, however, reduces the sensitivity of the instrument to the signal of interest (Figure 21) and may not significantly improve the signal-to-noise ratio.

Rejection of distant noise sources depends on having a precise match (or balance as it is sometimes referred to) between the number of area-turns in the coils. A symmetric gradiometer (Figure 19b) requires that $N_{\text{signal}} A_{\text{signal}} = N_{\text{comp}} A_{\text{comp}}$ where N is the number of turns and A the area of the signal and compensation coils respectively. Thus L_{coil} in eq. (5) becomes ($L_{\text{signal}} + L_{\text{comp}}$). An asymmetric design (Figure 19e) has the advantage that the inductance (L_{signal}) of the signal coil(s) can be much greater than the compensation coils (L_{comp}); greater sensitivity is achieved than with a symmetric design. Another advantage is that the signal coil diameter is reduced, leading to potentially higher spatial resolution. Another way to reduce the inductance of the compensation coils is to physically separate the windings of the compensation turns so that they act as N single turns ($L_{comp} \approx \text{N}\, L_{single\ turn}$) in series rather than a single tightly packed coil ($L_{comp} \approx \text{N}^2\, L_{single\ turn}$). The optimum conditions for the number of turns in an asymmetric signal coil is given by [38]:

$$\left(L_{signal} + L_{comp} + L_{input} + L_{leads}\right) - N_{signal} \frac{\partial}{\partial N_{signal}} \left(L_{signal} + L_{comp} + L_{input} + L_{leads}\right) = 0$$

Equation 6

If the gradiometer is perfectly made (balanced), it will reject uniform fields. However, if one coil has a larger effective diameter than the other, the response will not be that of a perfect gradiometer, but that of a gradiometer in series with a "smaller" magnetometer. Mathematically, the balance, β, can be defined as $V_t \propto G + \beta \cdot \boldsymbol{H}$, where V_t is the system response, G is the coil's response to a gradient field (*e.g.*, dB_z/dz), and $\boldsymbol{H}$ is the applied uniform field. If the coils are coplanar, there should not be any x or y field components detected. However, the reality of fabrication, (*e.g.*, tilt due to coil forms constructed from multiple pieces, imperfect machining, etc.) is such that there may be β's with x and y components.

Typically, coil forms used to wind gradiometers can be machined (grooved) to achieve balances that range from $\beta = .01 \sim .001$. Planar devices, fabricated using photolithography, can achieve significantly higher balances — a factor of 10 or better. Superconducting trim tabs [39] placed within the detection coils can improve β to the ppm level. High degrees of balance can allow a SQUID gradiometer to operate in relatively large (mT) ambient fields while maintaining sensitivities in the tens of fT. The use of electronic balancing (§4.7) can provide balance ratios at the ppm level [40].

4.6.1 Sensitivity

To use a SQUID magnetometer or gradiometer as a quantitative instrument, it is necessary to properly calibrate the output voltage-measured magnetic field relationship. A small coil located under the detection coil (*e.g.*, the "source" in Figure 20) can easily be used for calibration purposes. Other possible calibration sources include a large coil or straight wire [41]. A meander path of two small diameter wires next to each other with current flows in opposite directions can be used to determine spatial resolution in magnetic microscopes (§9.3).

4.6.2 Other design considerations

The design of the detection coil is dependant on the sensitivity and the spatial resolution required to measure the object(s) of interest. Coil optimization is not just that coil which gives the maximum magnetic field sensitivity.

Use of field sensitivity is a good metric if the object is in the far field approximation (source distance >> coil diameter). Geophysical measurements (*e.g.*, magnetotellurics - §8.1) is an example where field sensitivity is the determining measurement parameter.

If spatial resolution is important (*e.g.*, in non-destructive testing-§9 or biomagnetism-§10), then the object must be in close proximity to the detection coil(s). Near field analysis should be performed to determine the optimum coil design. Optimization for magnetic dipoles is discussed in §9.2; optimization for current dipoles is discussed in §10.2.

In addition to determining the optimum coil diameter and sensitivity, environmental noise considerations (§6) may require the use of gradiometers. Normally, gradiometers suffer from a loss in sensitivity due to the added inductance of the compensation coil (Figure 20). It should be noted that, for small diameter coils where the inductance of the coil is significantly less than that of the SQUID sensor, a gradiometer may have nearly the same sensitivity as a magnetometer. This may be of interest in situations where ultimate sensitivity is less important than noise rejection. Figure 21 shows the relative sensitivities for a magnetometer along with 1st and 2nd order symmetric gradiometers where the number of turns (at a given diameter) is optimized to match the total coil inductance to that of the SQUID sensor (eq. 5).

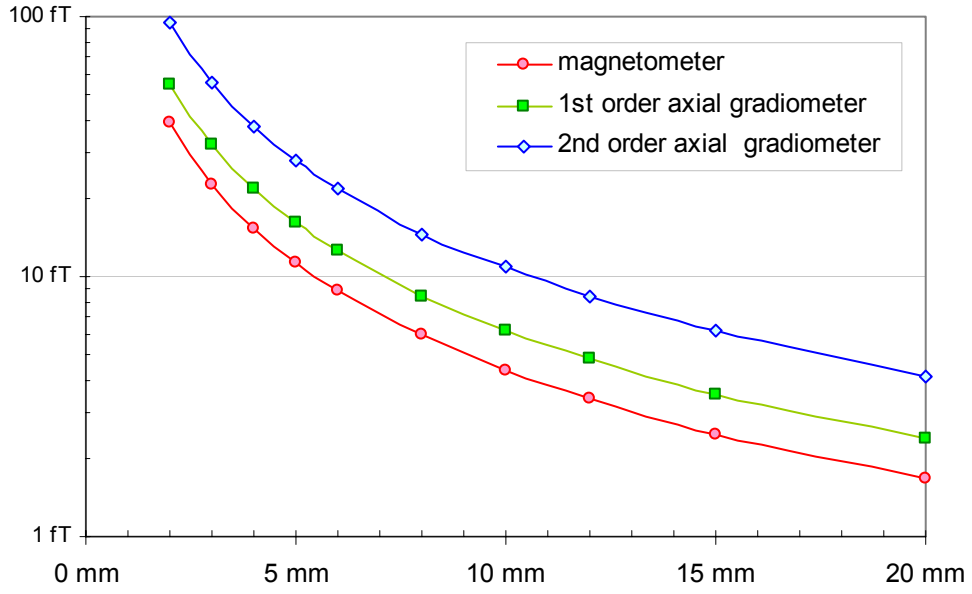

Figure 21 Sensitivity/√Hz vs. coil diameter for different detection coil designs. L_{SQUID} = 2 μH, Φ_{noise} = 5 Φ_o/√Hz, baseline = 5 x coil diameter, lead length (from SQUID sensor to detection coil) = 300 mm.

As can be seen, a larger diameter yields greater sensitivity. However, larger diameter coils will have poorer spatial resolution. An asymmetric 1st order gradiometer (Figure 19e) would lie between the magnetometer and the (symmetric) 1st order gradiometer.

4.6.3 HTS Gradiometers

Because of the inability to make flexible wire or make superconducting joints in HTS materials, present day HTS magnetometers are fabricated as planar devices and are available as pure magnetometers (Figure 19a) and planar gradiometers (Figure 19c). It is possible to use a thick film patterned (as a planar gradiometer) HTS tape and bend it (Figure 22) to form an axial gradiometer [42].

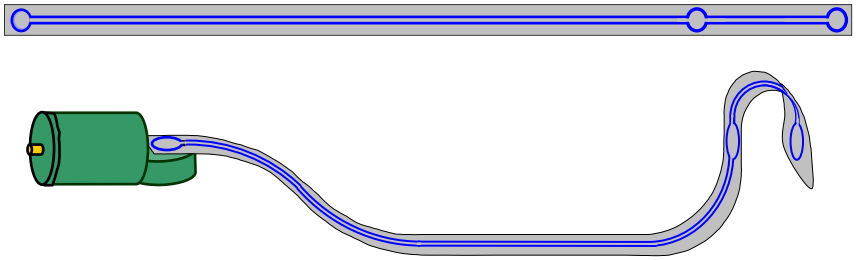

Figure 22: HTS patterned tape on flexible substrate (upper). HTS tape bent into axial gradiometer configuration. The flux is transported and inductively coupled to a 90° oriented HTS SQUID magnetometer (lower).

4.7 Electronic Noise Cancellation

Portions of (additional) magnetometer reference channel response(s) can be summed electronically with the gradiometers' input to balance out its effective magnetometer response. The simplest scheme is to use a second B_z magnetometer coil and subtract its output, $V(B_z)$ from the output of the gradiometer, V_t. The actual output is attenuated (by a factor b) as to exactly cancel the imbalance (β) of the gradiometer. By adjusting b $V(B_z)$ to equal $\beta \cdot \boldsymbol{H}$, the net result goes to G. Since there can be imbalance in the x and y components, a three axis set of coils (Figure 23) allow compensation of the B_x, B_y and B_z components.

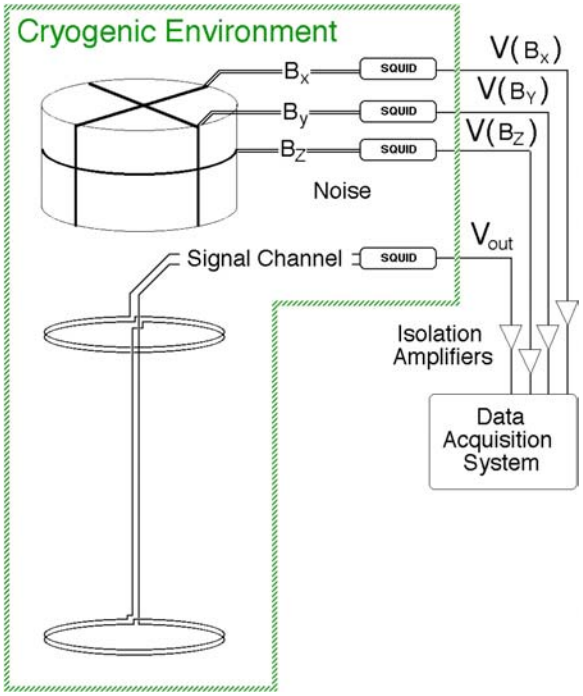

Figure 23 First order gradiometer with three noise cancellation channels

In addition to field noise, gradient fields generated by distant sources can be large enough to mask the signals being measured. Additional improvement can be achieved by the addition of a second gradiometer compensation channel. Thus the system output can be described as:

$$V_{out} \propto \boldsymbol{G} + \beta \cdot \boldsymbol{H} + b_1\, V(B_x) + b_2\, V(B_y) + b_3\, V(B_z) + g_4\, V(G_z) \qquad \text{Equation 7}$$

where b_1 is the weighting for the B_x component, b_2 is the weighting for the B_y component, b_3 is the weighting for the B_z component and g_4 is the weighting for the gradient reference component G_z (dB_z/dz).

As an example, the use of 3 reference magnetometers (B_x, B_y, B_z) gave an attenuation of externally generated noise of 12 dB for an axial gradiometer (Figure 23) [43]. The addition of an external gradient reference channel improved noise rejection to better than 40 dB. The gradient channel should be located sufficiently far from the sources being measured as not to detect significant signal, but close enough so that it sees the same gradient noise. Moving the reference gradiometer 1 meter away from the signal coil reduced noise rejection by a factor of 4 (12 dB).

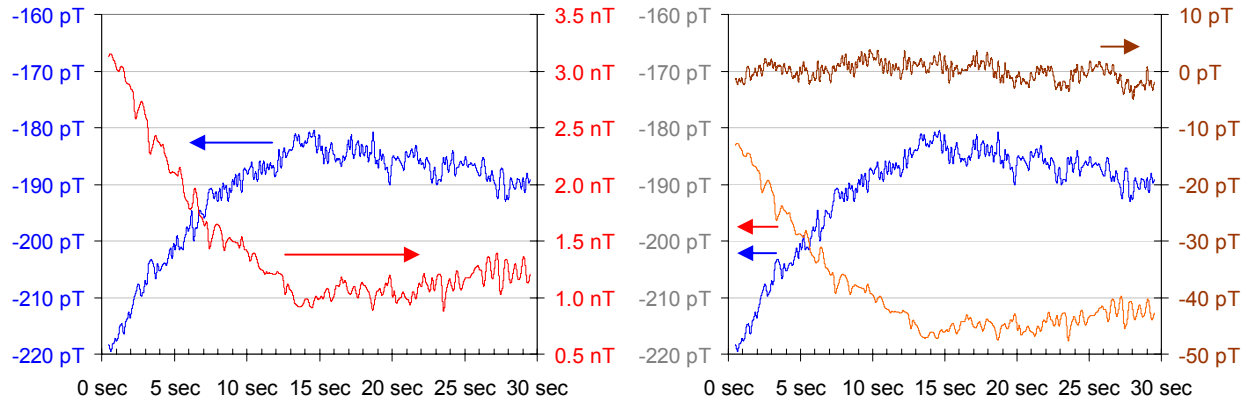

Figure 24 a) 1st order gradiometer (dB_z/dz) low frequency drift (blue); reference (B_z) magnetometer (red), b) gradiometer (blue), reference magnetometer (orange) attenuated by 65x and dc shifted by 135 pT, difference trace (brown) between gradiometer and reference magnetometer.

Even simple subtraction algorithms can give improvements in removing common mode noise. Figure 24 shows the result of a simple subtraction algorithm ($B_{net} = B_{grad} - B_{ref}/65$).

Improvement in signal to noise is inversely related to the degree of balance of a gradiometer detection coils. A well balanced gradiometer detection coil will show less improvement than a poorly balanced one. Efforts in improving intrinsic gradiometer balance can have significant benefits in reducing the need for electronic noise cancellation. Since the detection coil is not perfectly balanced, ideally, one should subtract all field and gradient components [expanding eq. (7)]. To do this would require eight "noise" channels, *e.g.,* B_x, B_y, B_z, dB_x/dx, dB_y/dy, dB_x/dy, dB_x/dz, and dB_y/dz. From these components, all nine elements of the gradient tensor can be created and used to compensate for any imbalance of the detection coil(s). The use of 8-element tensor arrays as reference channels can further improve external noise rejection, with rejection values exceeding 60 dB [40]. A major advantage of electronic balancing is significant improvement in immunity to low frequency environmental noise.

The simplest way to perform the noise cancellation is to simultaneously take data from the detection coil(s) and the noise channels. Then, in post-processing, digitize the data and determine the weighting factors for each noise channel to minimize any common mode "noise".

One can also include time derivatives of the field and gradient components or frequency domain components [44] into the cancellation algorithm to minimize effects of eddy current noise. If there is sufficient processing power, it may be possible to do real-time processing of the noise contribution by way of injection of the cancellation signals via external feedback (§4.2).

While electronic noise reduction may be necessary, initial attention should be paid to gradiometer balance. Improvement in signal to noise is inversely related to the degree of balance of a gradiometer detection coils. A well balanced gradiometer detection coil will have less benefit from electronic noise reduction than a poorly balanced one. Efforts in improving intrinsic gradiometer balance can have significant benefits in reducing the need for electronic noise reduction.

5 REFRIGERATION

The major advantage of high temperature superconductivity is the simplified cryogenics and reduced spacing between cryogenic regions and room temperature. The thermal load (due to conduction and black body radiation) is less and the heat capacity of what needs to be cooled is larger (implying smaller temperature variations for a given heat load). Since the latent heat/unit volume of liquid nitrogen is ~60 times larger than liquid helium, hold times become months rather than days for an equivalently sized dewar.

5.1 Dewars

The superconducting nature of SQUIDs requires them to operate well below their superconducting transition temperature (9.3 K for niobium and 93 K for $YBa_2Cu_3O_{7-\delta}$). Ideally, the cryogenic environment should provide stable cooling (mK or μK depending on $d\Phi/dT$ of the sensor, *c.f.* §3.3.2), have no time varying magnetic signature, be reasonably compact and reliable and, if mechanical in nature, introduce neither mechanical vibration nor a magnetic signature into the detection system. The thermal environment for the SQUID sensor and detection coil has typically been liquid helium or liquid nitrogen contained in a vacuum insulated vessel known as a dewar (Figure 25). The cryogen hold time depends on the boil-off rate (a heat load of 30 mW boils off ~1 liter LHe/day) and the inner vessel volume.

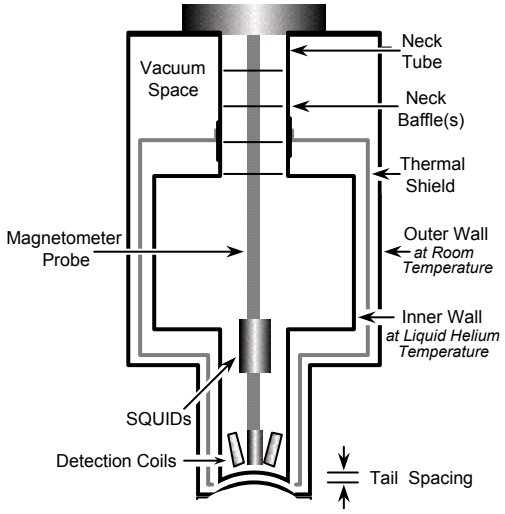

Figure 25 Typical design of a fiberglass dewar used for biomagnetic measurements, superinsulation not shown.

The space between the inner and outer walls is evacuated to prevent thermal conduction between room temperature and the cryogen chamber. Within the vacuum space, a thermal shield (anchored to the neck tube) acts to reduce heat transfer by thermal (blackbody) radiation. The thermal shield can be either vapor cooled (Figure 25)—using the enthalpy of the evaporating helium or nitrogen gas—or having the shield thermally connected to a liquid nitrogen reservoir. The evaporating gas can also be used to cool electrical connected to the SQUID sensors if the probe is immersed in the liquid cryogen (Figure 26a). Dewars with removable sections (*e.g.*, tails) use liquid nitrogen cooled shields. Having a shield at 77 K effectively reduces the blackbody radiation by a factor of $(300/77)^4 \approx 230$ (*c.f*, eq. 8). Multiple layers of highly reflective aluminized Mylar® (often referred to as superinsulation) are placed between the inner and outer walls and the thermal shields to further reduce blackbody radiation.

If the experiment involves measurements interior to the dewar (*c.f.*, Figure 33a, c - e), then a metallic dewar is preferable. Metallic dewars offer significant shielding from environmental noise at frequencies above 10 ~ 100 Hz. If the system is to measure magnetic fields exterior to the dewar, the dewar must be magnetically transparent and metallic construction is not appropriate. Dewars for external field measurements (Figure 25) are normally constructed of non-metallic, low susceptibility materials to minimize their magnetic interactions with the SQUID sensors and detection coils. Materials used are typically glass-fiber epoxy composites such as G-10. To get the detection coil(s) as close as possible to the object being measured, a "tailed" design is often used. This decreases the forces on the bottom of the dewar and allows the use of thinner end pieces (closer tail spacing). Dewars for biomagnetic measurements often have curved tails to get closer to the head, chest or abdomen.

5.1.1 Fabrication

Most dewars are built from glass/epoxy composite tubes and plates. Typically, a G-10 glass composite (similar to the material used in computer circuit boards) is used. It should be noted that properly made dewars can last well over a decade while undergoing multiple thermal cycles. If using a mechanical or diffusion pump when pumping out the vacuum space in the dewar walls (Figure 25), be sure that the pumping line has a LN_2 trap to avoid backstreaming the oil into the dewar. Oil can significantly degrade the ability of superinsulation to reduce black body radiation (§5.1.1.1).

Because the vacuum space between the dewar walls are evacuated, convection is not a significant heat load. There are three main sources of heat flux into a dewar (besides the thermal conduction due to the SQUID lead cabling): Black-body radiation impinging on the inner portion of the dewar vessel containing the liquid cryogen, thermal conduction down the neck tube, and 300 K black-body radiation down the neck tube.

5.1.1.1 Black body radiation

Black body radiation ($Q_{blackbody}$) is normally the dominant heat load on a dewar. Since the net load goes as the 4th power of the temperature (eq. 8), having a radiation shield at an intermediate temperature reduces the blackbody radiation by more than an order of magnitude.

$$\dot{Q}_{blackbody} = \varepsilon \sigma A \left(T_H^4 - T_L^4 \right) \qquad \text{Equation 8}$$

where ε is the emissivity of the radiating surface of the radiating surface, σ is the Stefan-Boltzman constant (5.67×10^{-8} W/m^{2}K^4), T_H is the hotter temperature and T_L the colder temperature. The use of multilayer superinsulation (MLI) can give significant reductions in blackbody radiation by providing tens to hundreds of additional highly reflective, low emissivity surfaces between the hotter and colder surfaces. If superinsulation is used, eq. 8 becomes [45]:

$$\dot{Q}_{MLI} = \frac{\sigma A \left(T_H^4 - T_L^4 \right)}{2\left(\frac{1}{\varepsilon} + \frac{1}{\varepsilon_{MLI}} - 1 \right) + \frac{(N-1)(2-\varepsilon_{MLI})}{\varepsilon_{MLI}}} \qquad \text{Equation 9}$$

where ε_{MLI} is the emissivity of the superinsulation and N is the number of superinsulation layers. In the limit where $\varepsilon_{MLI} << \varepsilon$, eq. 9 goes as $\dot{Q}_{MLI} = \varepsilon_{MLI}\, \sigma\, A \left(T_H^4 - T_L^4 \right) / \left[N(2 - \varepsilon_{MLI}) \right]$. Care must be taken during fabrication to avoid contamination of the reflecting surfaces. Thumb prints

or oil contamination can raise the emissivity of aluminized Mylar® superinsulation from ε_{MLI} = 0.03 to near that of oxidized copper ($\varepsilon \approx 0.6$).

5.1.1.2 Thermal conduction down the neck tube and magnetometer probe

Because most cryogenic inserts are loaded from the top of the cryostat, a sufficiently large neck tube is needed, not only to allow passage of the insert, but to support the weight of the inner vessel and liquid cryogen. The larger the neck diameter, the greater the thermal load (eq. 10).

$$\dot{Q}_{conduction} = \int_{T_L}^{T_H} \kappa \frac{A}{\ell} dT \qquad \text{Equation 10}$$

where $\kappa(T)$ is the thermal conductivity, A is cross-sectional area and ℓ is the length of the conductor

Since $Q_{conduction}$ is a function of the thermal conductivity of the neck tube, it is advisable to use low conductivity materials such as G-10 rather than stainless-steel. Thermal conduction down the neck tube can be reduced by using the enthalpy of the cold evaporating gas to cool the neck wall. This contribution can be essentially reduced a factor of 5~6 by proper design. As a rule of thumb, a G-10 neck tube has a roughly linear thermal profile from cold to hot. Additionally, a vapor cooled neck tube gives the designer a place to attach a black-body radiation shield. Because there is no superinsulation down the neck tube, black-body radiation from room temperature down the neck (Figure 25) can be a significant thermal load. Most of this load can be absorbed by placing 2 - 4 vapor-cooled horizontal baffles 4 - 5 cm (vertically) apart [46]. For a liquid helium dewar, the baffles should be positioned about where the 77 K region would be one third to one quarter of the way up the neck tube). Any holes (*e.g.*, for wiring, etc.) in the baffle(s) should be plugged or taped over.

The thermal head load of any cabling (*e.g.*, SQUID leads, magnet current leads, level detector leads, etc.) leading into the cryostat must also be taken into account. Vapor cooling of the cabling can significantly decrease its thermal load.

One problem with plastic neck tubes is that—while warm—helium gas can diffuse through them and into the vacuum space. A very thin layer of aluminum or other metallic foil can be placed in the neck tube to act as a diffusion barrier; this permits thinner neck tubes. If the dewar exhibits excessive boil-off after a period of time, it may be worthwhile to warm it up and check the vacuum. If the pressure is above 50-100 milliTorr, pumping out the vacuum space is recommended. Using a mass spectrometer leak detector can give insight into if the pressure is due to a small helium (or nitrogen) leak or outgassing.

The practice of putting polystyrene or polyurethane foam plugs instead of baffles is not recommended. While the initial boil-off is low, as soon as the foam is saturated by the evaporating cryogen, the thermal conductivity of the plug becomes greater that the vapor alone and the overall thermal load on the dewar increases. A set of gold plated copper baffles *without foam baffles* may give the best results.

5.1.2 Tail spacing (gap)

In situations where external properties (such as magnetic fields of nearby objects, *e.g.*, NDE or biomagnetism) are to be measured, the smallest possible distance between detection coil(s) and room temperature is desirable. This distance (sometimes referred to as the tail gap) is primarily

dependent on the diameter of the dewar tail. The inner and outer tail pieces must be thick enough such that they do not deform (bow in or out) due to differential atmospheric pressure. For example, on a 25 cm diameter disk, a 1 atmosphere differential is equivalent to a force of ~½ ton! The thickness of the tail pieces is determined by the amount of deflection (bend) that that is acceptable. Typically, for a flat plate, bends of more than a tenth of a mm are to be avoided. The thicker the plate, the smaller the deflection. For large i.d. dewars, thicknesses become quite large.

Since most dewar materials shrink as they get cold, the distance between the inner and outer tail sections (tail gap) will increase. For G-10, the thermal contraction from 300 K to 4.2 K is ~0.3%. Thus a 1 meter high flat bottom dewar whose inner and outer tails are nearly touching (when warm) would have an additional 3 mm separation when the inner vessel is at liquid helium temperature. There are a number of different mechanisms to decrease the spacing.

5.1.2.1 Adjustable gap mechanisms

By placing a bellows (or similar vacuum tight mechanism) in the outer tail section (Figure 26b), it is possible to reduce the coil-to-sample spacing (and eliminate the thermal contraction).

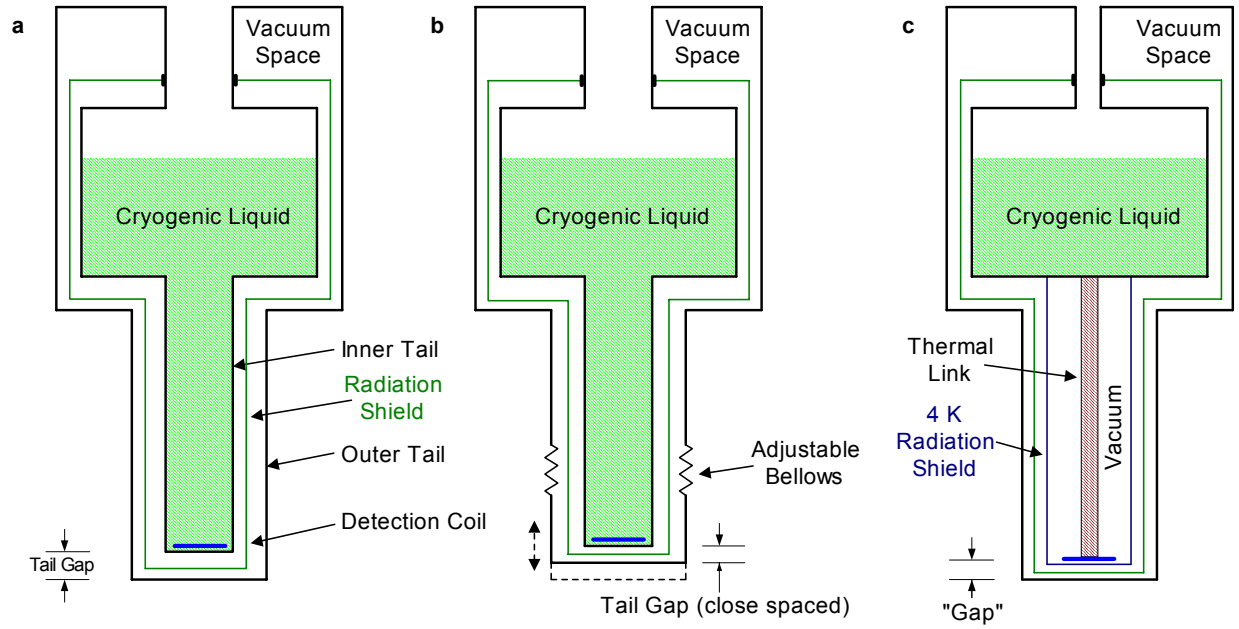

Figure 26 Different methods of achieving close dewar tail spacing. Thermal shielding is omitted for clarity.

The minimum achievable distance is dependant on the coil diameter and number of channels. Gaps (this includes the thicknesses of the inner and outer tail pieces) as small as 2 mm (Figure 45) have been achieved for liquid helium dewars with 3 mm detection coils. Gaps of ~100 μm have been achieved for LN_2 dewars using coil-in-vacuum construction [47]. Care must be taken to increase the "gap" prior to warming up the dewar, or the inner tail may push against the outer tail and damage or destroy the dewar.

5.1.2.2 coils in vacuum

Rather than placing the detection coil(s) in liquid, coil-in-vacuum technology connects the detection coil(s) to the cryogen bath by a thermal link (Figure 26c). This eliminates the need for an inner tail section and reduces the minimum distance between the detection coil(s) and room

temperature. Typically the thermal link is constructed from a high thermal conductivity material such as copper or sapphire. By thermally anchoring the SQUID sensor(s) to the dewar belly, the detection coil(s) need only be kept below their superconducting transition temperature (9.3 K in the case of NbTi). This reduces the amount of MLI (§5.1.1.1) and allows even closer spacing. Like liquid immersion dewars, coil-in-vacuum cryostats can also benefit from adjustable tail mechanism. An alternate method, rather that adjusting the eternal tail section, is to have an adjustable mechanism at the thermal link [48] that allows the coils to be moved up and down. Both gear and lever mechanisms [49] can allow adjustments at the tens of μm level.

Since the probe does not need to be inserted down the neck tube, coil-in-vacuum dewars can have significantly smaller neck tubes (Figure 26c). This reduces the heat load and allows longer hold times. The disadvantages include significantly more complex construction, ensuring that all SQUID leads are thermally anchored (rather than being cooled by the cryogen vapor as in liquid immersion dewars), and that the SQUID sensors and detection coils are part of the dewar and can not be removed without disassembly of the dewar.

5.2 Closed Cycle Refrigeration

As an alternative to the use of liquid cryogens, closed cycle refrigeration [50] would be desirable for several reasons. These include reduction of operating costs, use in remote locations, operation in non-vertical orientations, avoiding interruptions in cryogen deliveries, safety, and the convenience of not having to transfer every few days. Parameters governing suitability include physical size, absence of periodic replacement of cryogenic fluid and most importantly vibration and magnetic signature. There are two main obstacles to using closed cycle refrigeration with SQUIDs. The first is the mechanical movement that (ultimately) causes the detection coils to move in the Earth's magnetic field. The second is the magnetic signature due to the moving parts of the cryocooler's cold head and compressor. Moving the compressor far away will reduce its relative signature. While cryocoolers [51] can have large cooling capacities, unless hundreds of channels are involved, only mW's of cooling capacity are needed to maintain SQUID sensors at their operating temperatures.

The first practical cryocooled SQUID system was the BTi CryoSQUID (Figure 27). Based on a two stage Gifford-McMahon (G-M) refrigerator, the use of a Joule-Thompson (JT) stage allowed 4 K operation with reduced vibration. An electronic comb filter was required to filter the ~1 Hz compressor vibration from the output of the dc SQUID electronics to achieve system performance of 20 fT/√Hz. However, the acoustic (audible) noise from the compressor prevented its use in auditory evoked brain measurements.

There are two main obstacles to using closed cycle refrigeration with SQUIDs. The first is the mechanical movement that (ultimately) causes the detection coils to move in the Earth's magnetic field. The second is the magnetic signature due to the moving parts of the cryocooler's cold head and compressor. Moving the compressor far away will reduce its relative signature. By moving the valving from the top of the cryocooler (*i.e.*, a split head) to a meter away will reduce its signature. The remaining contributions to magnetic signature and vibration are the movement (for a G-M cycle) of the heat-exchanger and the stretching of the tubes generated by gas compression and expansion [52].

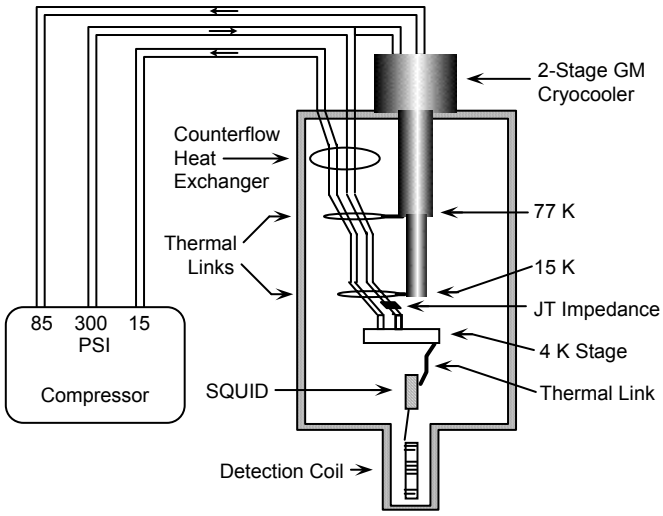

Figure 27 CryoSQUID components (*c.f.*, ref. [48])

Although multichannel cryocooled systems [53] have been built, the vibration and magnetic signature of closed cycle refrigerators kept them from widespread use. If G-M refrigerators are to be used, it may be necessary to electronically subtract (*e.g.*, §4.7) out the synchronous noise (from the compressor and valve head) in order to get usable data. The development of pulse tube refrigerators [54] offers promise for magnetometer operation with significantly reduced vibration (a factor of ten better than a standard GM cycle cryocooler). Two stage pulse tube refrigerators have demonstrated 1 watt cooling power at 4.2 K with a minimum achievable temperature of 2.5 K. Single stage pulse tube refrigerators have demonstrated 12 watts cooling power at 77 K with a minimum achievable temperature of 40 K.

When considering the use of a closed cycle refrigeration system, both thermodynamic and operational parameters must be taken into consideration. The first consideration is usually the required operating temperature, followed by the available refrigeration capacity.

System performance is also determined by the total mass to be cooled, the total volume, and the cool down time. For systems that are used to cool sensors, mechanical vibration, electromagnetic emission and magnetic signature must be taken into account. For split systems (where the compressor head is remote from the top of the dewar), one must be concerned about flexible vs. inflexible leads and the thermal influence of warm and cold leads to the cryogenic region.

Other considerations include reliability and operating life (mean time before failure and mean time before maintenance), cost, if an external (water or air) cooling system is needed for the compressor, tolerance to vibration and acceleration, and orientation problems (must the cryocooler be in a specific orientation?).

6 ENVIRONMENTAL NOISE

The greatest obstacle to SQUID measurements is external noise sources (Figure 28). If the object being measured is within the cryostat (such as is typical in most laboratory experiments), metallic shielding can minimize external noise (*e.g.,* act as a low pass eddy current shield). The use of gradiometer detection coils (§4.6) can significantly attenuate the effect of distant noise sources. Superconducting shields essentially eliminate all external field variations. This assumes that any electrical inputs to the experimental region have been appropriately filtered. Interference at powerline or microprocessor clock frequencies can severely degrade performance. Unfortunately, if external objects are to be measured, superconducting shields are not appropriate.

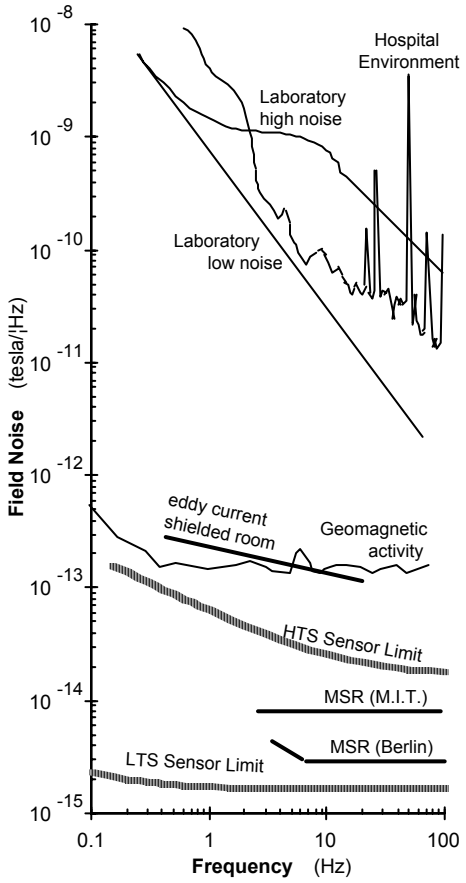

Figure 28 rms field noise spectra in various environments as a function of frequency (After [55]).

When measuring external fields, the SQUID magnetometer must operate in an environment — the magnetic field of the Earth — that can be 10 orders of magnitude greater than its sensitivity (Figure 28). The magnetic field at the surface of the Earth is generated by a number of sources. There exists a background field of ~50 μT with a daily variation of ± 0.1 μT. In addition, there is a contribution (below 1 Hz) from the interaction of the solar wind with the magnetosphere. The remaining contributions to external magnetic fields are primarily man-made. These can be caused by structural steel and other localized magnetic materials such as furniture and instruments that distort the Earth's field and result in field gradients, moving vehicles that

generate transient fields, electric motors, elevators, radio, television, and microwave transmitters, and the ever present powerline electromagnetic field and its harmonics.

6.1 Gradiometers for noise reduction

If the purpose of the measurement is to detect the magnetic field of a relatively close object, the detection coil(s) can be configured as a gradiometer (*c.f.*, §4.6) whose baseline is larger than the distance from the coil(s) to the object. This can allow rejection of external noise by more than 120 dB with less than a dB loss of signal. It is standard practice to configure SQUID measurement systems for biomedical and non-destructive evaluation measurements as gradiometers.

6.2 Magnetic Shielding

Attenuation of external magnetic fields can be accomplished by induced current shielding or flux shunting. Faraday's law ($\nabla \times \mathbf{E} = -\partial\mathbf{B}/\partial t$) states that an electric field is induced in a material when it is exposed to a time dependent magnetic field. If the material is conducting ($\rho << \infty$), the electric field induces a current that generates a magnetic flux to oppose the externally applied field. This effect, which is frequency dependent, can be used to create an eddy current shield to attenuate electromagnetic interference. The behavior of the magnetic field and magnetic flux density is governed by Ampere's law which requires that $H_{tangental}$ be continuous and Gauss' law which requires the B_{normal} also be continuous at the interface between materials of differing magnetic permeability. The effect for materials with high magnetic permeabilities ($\mu >> 1$) is that magnetic flux is "pulled" towards a shielding material, "shunted" within the material and then "released" back into the air (or vacuum), on the external surface of the shielding material [56]. Flux shunting is effecting even at dc. The amount of flux shunting is dependent on μ. The Meissner effect (§1.2) can also be used to make superconducting shields that shield external fields independent of frequency. These effects can be used individually or in combination to significantly reduce the effects of environmental noise.

6.2.1 Induced current shielding

One method to attenuate external noise sources is with an eddy current shield that generates fields that act to cancel the externally applied fields within the conducting material. The shielding effect is determined by the skin depth, λ—the distance where the field is attenuated by a factor 1/e. For a sinusoidal varying wave,

$$\lambda = \sqrt{\rho/\pi\mu_o f} \qquad \text{Equation 11}$$

where f is the frequency of the applied field, ρ the electrical resistivity and μ_o is the magnetic permeability of free space. In situations where the wall thickness $t << \lambda$, external fields are attenuated by

$$\frac{H_{internal}}{H_{external}} = \frac{1}{1+\left(2\pi f L/R\right)^2} \qquad \text{Equation 12}$$

where L is the inductance of the enclosure and R is the resistance along the path of current flow. Unfortunately, induced currents in the shield generate noise. For a right circular cylindrical shape at a temperature T, the field noise internal to the can is given by:

$$B_{rms} = \sqrt{\frac{32\,\pi\,k_B\,T\,t}{\ell\,d\,\rho\times 10^{12}}} \qquad \text{Equation 13}$$

where ℓ is the length and d the diameter of the can in MKS units. The cut-off frequency is given by $f_{-3dB} \approx \rho / 4\,\pi\,t\,d \times 10^5$ (again MKS units). Because of noise considerations, eddy current shields that are to be placed near the detection coils should be made from relatively poor conductors such as BeCu.

Another approach is to use eddy current shielding to shield the entire measurement system. An eddy current room (2.4 m x 2.5 m x 3.6 m) constructed with 2 cm, high purity aluminum walls can achieve shielding > 40 dB at 60 Hz with improved performance at higher frequencies [57]. The equivalent field noise was less than 200 fT/√Hz at frequencies above 1 Hz.

In the situation where $t >> \lambda$, the attenuation goes as $(r/\lambda)e^{t/\lambda}$. If pure eddy current shielding is used, this would require wall thicknesses that could exceed one meter or more to achieve reasonable attenuation below 1 Hz.

6.2.2 Flux shunting

The need for shielding at lower frequencies down to dc has led to the use of high permeability materials for shunting magnetic fields external to the experimental region. For a ferromagnetic material, the permeability of the material [$\mu = \mu_o(1 + \chi)$] replaces μ_o in eq. (11). The shielding is due to the fact that flux prefers the path with the highest permeability. Since magnetically "soft" materials (*e.g.*, mu-metal) can have permeabilities that exceed 10^4, the external magnetic flux is shunted through the mu-metal walls, reducing the magnetic flux intensity (**H**) inside the shield.).

Figure 29 Commercial magnetically shielded room showing first layer of mu-metal shielding and rigid aluminum frame. Courtesy of Vacuumschmelze GmbH.

For biomagnetic measurements (§10), it may be necessary to enclose not only the sensing device, but the subject in a magnetically shielded room (MSR) with large interior dimensions (*e.g.*, 2 m x 3 m x 2 m). The first MSR used for SQUID measurements was built at the MIT

Magnet Lab [58] and had an octagonal shape. This room was used for the first magnetocardiogram [59] (§10.4) and magnetoencephalogram [60] (§10.3) recordings. The use of multiple shields can act to further shield the interior of a MSR (Figure 30). For the six layer Berlin MSR [61], shielding factors exceeded 80 dB at frequencies above 0.01 Hz with noise levels below 3 fT/√Hz. All commercial MSRs combine multiple mu-metal for low frequency and aluminum walls for high frequency shielding (Figure 29). Reference [62] give a good overview of MSR design.

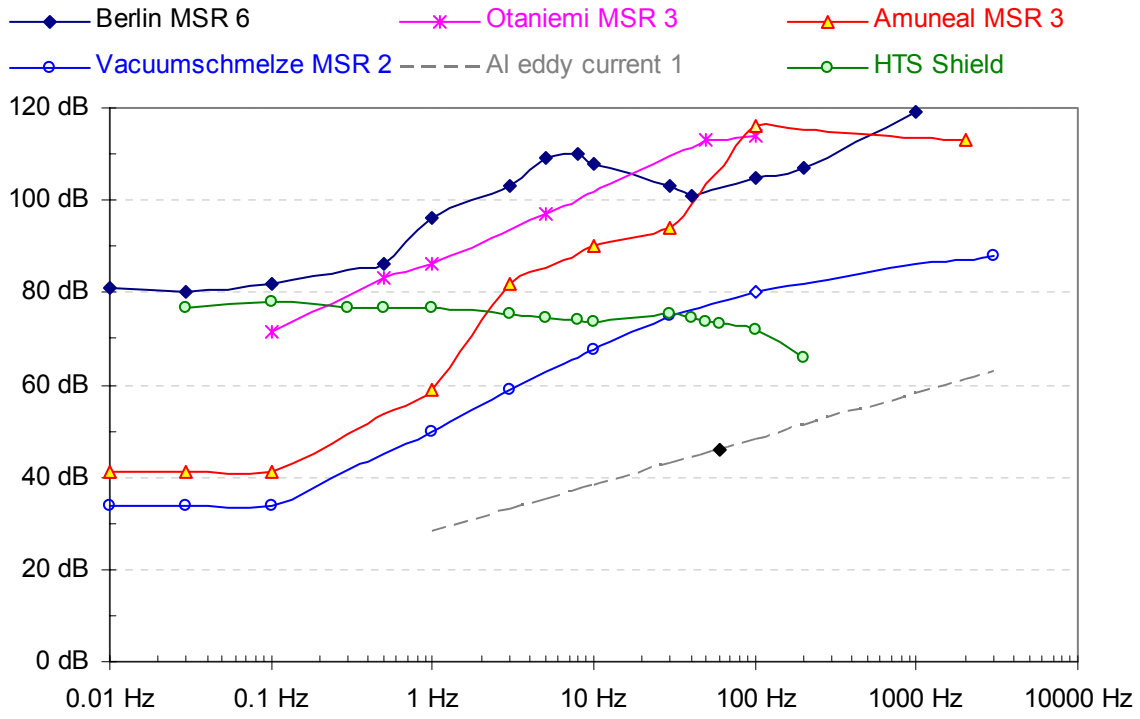

Figure 30 Shielding factors for various shielded rooms. The trailing number refers to the number of mu-metal layers. The dashed line is the shielding factor for an aluminum eddy current room [57].

The ideal shield would be a superconducting shield because of its ability to provide complete shielding down to dc. A completely enclosed (*e.g.*, six sided) superconducting MSR would be unrealistic. The use of HTS superconductors such as $Bi_2Sr_2Ca_2Cu_2O_{10}$ have allowed the construction of cylindrical shields [29] with attenuation that approach that of the Berlin six layer MSR (Figure 30).

6.2.3 Shielding factors

The attenuation of the transverse magnetic field at dc (ignoring end effects) for a single layer closed cylindrical shield where $\mu >> 1$ is given [63] by $A \approx \mu t/d$, where t is the wall thickness and d is the outer diameter of the shield. The use of multiple layer shields with gaps between the shields can further improve shielding (and provide low field environments. For a two layer shield, $A \approx A_{inner} + A_{outer} + A_{inner}A_{oute}\,[1 - (d_{inner}/d_{outer})^2]$. For particularly noisy backgrounds or experiments where sub-picotesla environments are needed, three or four layer shields may be necessary.

In many situations, it is not possible to completely enclose the detection coils. An open ended tube of high permeability or superconducting material can still provide significant attenuation of external fields. Table 2 gives the attenuation for both axial and transverse fields for semi-infinite tubes ($\mu = \infty$ for normal metals, $\mu = -1/4\pi$ for superconductors).

Table 2: Relative attenuation along the axis of ideal semi-infinite superconducting cylinder [64]. *z* is the distance measured from the open end of the can and *d* is the diameter of the can.

	H_{axial}	$H_{transverse}$
Superconducting ($\mu = -1/4\pi$) tube	$e^{-7.664\ z/d}$	$e^{-3.68\ z/d}$
mu-metal ($\mu = \infty$) tube	$e^{-4.81\ z/d}$	$e^{-7.664\ z/d}$

If the shield has a finite length (*h*) and the measurement point is at the midpoint of the tube (*h*/2), the shielding factor would be half that of a single semi-infinite tube. For example, taking the dimensions of the cylindrical shield described in reference [29] (d = 65 cm, z (half the length of the tube) = 80 cm), gives a theoretical attenuation of $H_{axial}/H_{external} = ½\ e^{-7.664*80/65} = -88$ dB. This can be compared to the measured values of 77 db (Figure 30).

For positions above (or below the halfway point), the attenuation can be modeled as the "sum" of two semi-infinite tubes, one at depth z, the other at z + *h*/2. It can be seen that the axial shielding factor of a superconducting tube is superior to that of a mu-metal tube, whereas the transverse shielding factor of a mu-metal tube is greater than the transverse shielding factor of a superconducting tube. This implies that a combination of superconducting and mu-metal shields may serve to better screen both transverse and axial noise field components than either shield alone.

6.2.4 Active Shielding

MSR shielding factors up to 120 dB (10^6) can be achieved by the use of active shielding [65]. In this situation, external coils surround the exterior of the MSR. A low noise magnetometer (SQUID or fluxgate) is mounted at the interior of the MSR. Its output is used (in a negative feedback mode) to generate a current that is fed into the external coils to cancel the low frequency noise (drift) detected by the magnetometer. By using coils (and detectors) in all three dimensions, 30 - 40+ dB of additional noise reduction can be achieved at low frequencies.

The use of external field coils can allow significant reduction in external noise even without a MSR. Nearly 70 dB attenuation at 60 Hz can be achieved by using a reference magnetometer and appropriate negative feedback electronics to drive a large (2.4 m) set of Helmholtz coils. It is important to use a reference sensor with the same characteristics as the detection coil(s). If the reference sensor has a significantly higher noise level, it will not be possible to achieve sensor noise limited sensitivities.

6.3 Electrical Noise

SQUID magnetometers and gradiometers are highly sensitive to external magnetic noise and radiofrequency interference (rfi). If working with a SQUID specifically designed to measure external fields, it is advisable to perform initial tests in a magnetically shielded environment. If you do not have access to a shielded room, measurements made after midnight or on the weekend can be compared to measurements during the day to see if there are environmental effects. In particularly bad environments, if rfi is of concern, wrapping the dewar in aluminum foil may improve the situation. This acts as an eddy current shield. While it may reduce the

system's bandwidth (depending on the amount of aluminum foil used) and perhaps increase the system's white noise, it can be very effective in attenuating rfi.

During the initial testing, be sure that the system is on a sturdy platform. A flimsy table may cause motion induced noise. Also be sure that the platform (or whatever mounting is being used) is free of any ferromagnetic contaminants. Avoid using conductive metal tables as they can couple in gradient noise.

The instrumentation being used can be a source of generate noise. Another source of rfi is microprocessor clock frequencies. The leads going from the SQUID sensor(s) to the electronics have to be electrically isolated from any other circuitry. Opto-isolation (fiber-optic coupling) can isolate the microprocessor from the experiment. One test to see if there are potential noise problems is to run a hair dryer near the measurement circuit. The carbon brushes will generate large amounts of rfi noise and can help to diagnose potential problems during construction.

Common grounds are to be avoided like the plague—the introduction of powerline frequencies can overwhelm almost any measurement. The leads should be twisted (non-inductively wound) pairs. If rfi pickup is of concern, the leads should be shielded in metal tubing or metallic braid shielding. PbSn tubing between the detection coil and SQUID sensor is preferred because it acts as a superconducting shield below 6 K. If using PbSn tubing, be sure that the leads can not move inside the tubing. Well twisted leads that are properly anchored are better than leads that may move around inside of a superconducting shield tube. Measurements made after midnight or on the weekend can be compared to measurements during the day to see if there are environmental effects.

7 LABORATORY APPLICATIONS

SQUIDs offer the ability to measure at sensitivities unachievable by other magnetic sensing methodologies [1]. However, their sensitivity requires proper attention to cryogenics and environmental noise. SQUIDs should only be used when no other sensor is adequate for the task [66]. This applies to not just laboratory applications, but to every potential use of SQUID sensors. A large number of applications configure the SQUID as a magnetometer. Sections 8 - 10 discuss a number of specific uses.

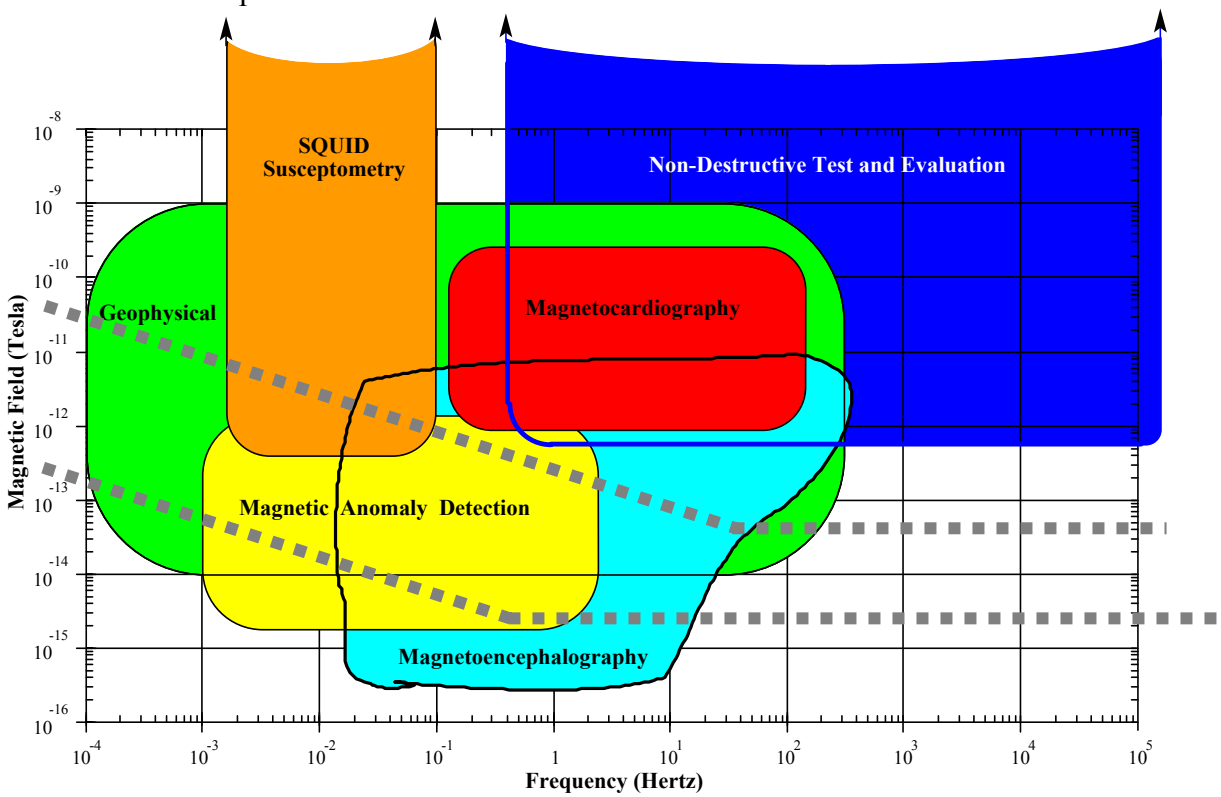

Figure 31 Field sensitivities and bandwidths typical of various applications. The dashed lines indicate the sensitivity of commercially available SQUIDs (lower line LTS - Figure 14d, upper line HTS - Figure 14e)

There are many exotic uses for SQUID sensors. Figure 32 shows how a toroidally wound coil can be used to detect charged particles (in this case anti-protons) in a particle accelerator [67]. Planar gradiometers (Figure 19c) can also be used as a detection coil [68].

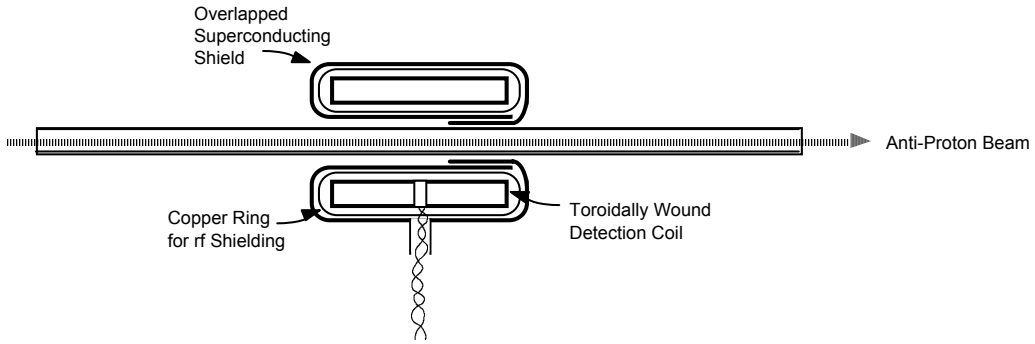

Figure 32 Beam Current meter

SQUIDs can also be configured to measure a wide variety of electromagnetic properties (Figure 33).

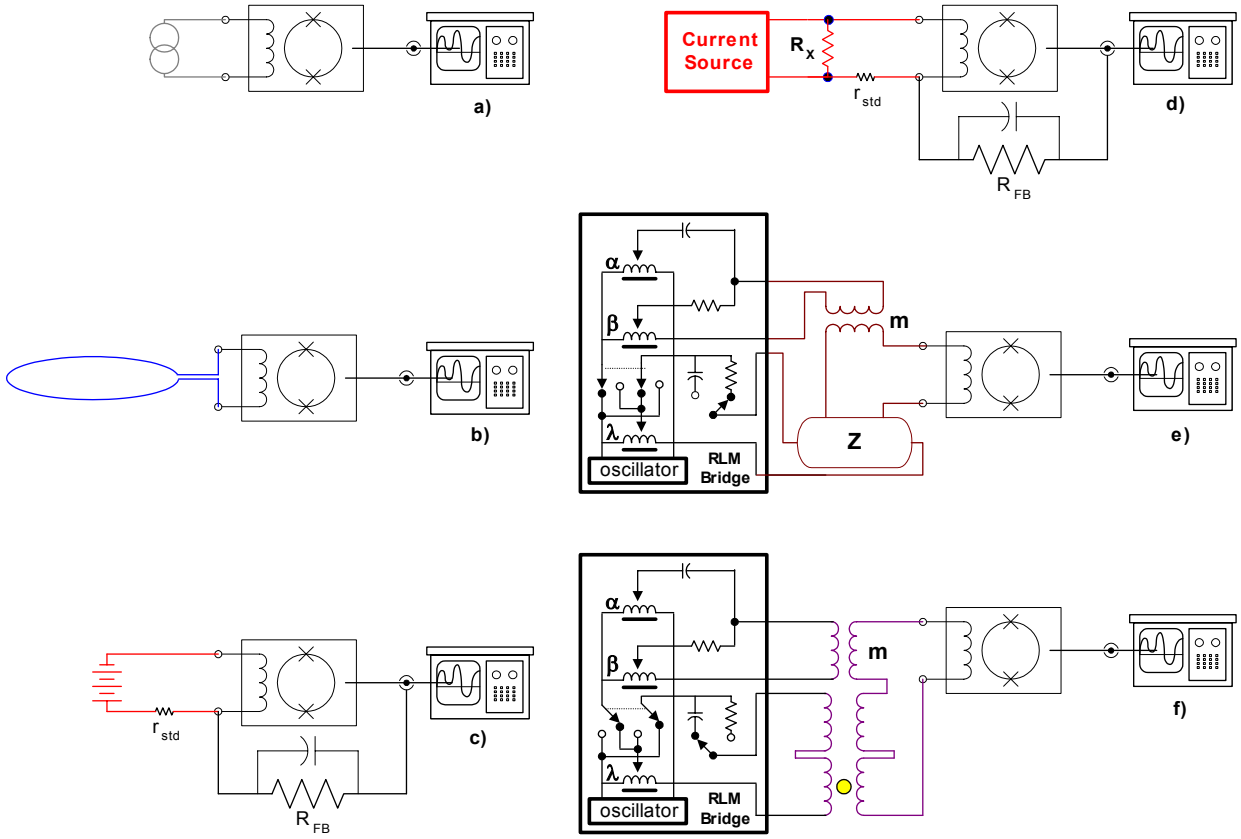

Figure 33 (a) ac and dc Current, (b) Magnetic Field, (c) dc Voltage, (d) dc Resistance, (e) ac Resistance/Inductance Bridge, (f) ac Mutual Inductance (Susceptibility Bridge)

As mentioned in §2.1, there is no method for making true superconducting connections to SQUIDs with HTS wire. As a result, commercially available HTS devices are currently in the form of magnetic sensing (Figure 33b) rather than current sensing devices (Figure 33a, c-f).

Table 3 shows typical capabilities of SQUID-based instruments. The number in the parenthesis refers to the corresponding figure. Additional information on laboratory applications of SQUID systems can be found in references [33, 69, 70].

Table 3 Typical sensitivities of SQUID instruments

Measurement	Sensitivity
Current (24a):	10^{-12} ampere/√Hz
Magnetic Fields (24b):	10^{-15} tesla/√Hz
dc Voltage (24c):	10^{-14} volt
dc Resistance (24d):	10^{-12} Ω
Mutual/Self Inductance (24e):	10^{-12} Henry
Magnetic Moment (24f):	10^{-10} emu

If there is no fundamental reason that requires dc measurements, ac measurements may provide higher signal-to-noise. Moving the effective measurement frequency and using a lock–in amplifier to reject out-of-band noise can significantly improve signal to noise. This can be helpful in situations where $1/f$ noise or external noise sources (*c.f.*, Figure 28) are significant.

7.1 dc measurements

One common use of a SQUID is as an ammeter. dc measurements can be made by directly coupling the current into the input circuit of the SQUID sensor in the case of LTS SQUIDS and inductively coupling (via superconducting transformers) into HTS SQUID sensors. If coupling into a circuit that is at room temperature [71], significant low pass filtering of the input current must be done to prevent rfi interference. A toroidal geometry for the input coil has the advantage of extremely good coupling to the source while having excellent immunity to external sources. Such a configuration has been used to construct an anti-proton beam current meter [72].

There are also a number of applications where the input circuits can be resistive. One example is the detection of extremely small voltage or resistance. Figure 33c shows the schematic of a SQUID picovolt measuring system. When a voltage V_{input} is applied across the input terminals, a current is generated in the SQUID input coil. In this situation, the feedback current (I_{FB}) that would normally be applied to the SQUID loop via the feedback coil (see Figure 13) is fed back via R_{FB} through r_{std} until the voltage drop across r_{std} is equal to V_{input} and there is no net current through the SQUID. The output voltage (V_{output}) measures the voltage drop across R_{FB} and r_{std} with $V_{input} = V_{output} \times r_{std}/(R_{FB} + r_{std})$.

The voltage gain of the system is determined by the ratio of R_{FB}/r_{std}. Typical values for R_{FB} and r_{std} are 3 kΩ and 30 μΩ respectively giving a voltage gain of 10^8. The standard resistor r_{std} is, typically at 4.2 K. The voltage source, however may be at a completely different temperature.

With the addition of an appropriate current source, it is possible to measure resistance (Figure 33d). Replacing V_{input} with a resistor (R_X) and a highly stable constant current source (I_{CCS}) [73] creates a voltage drop across the resistor. The resistance is determined by $R_X = V_{output} \times r_{std}/[(R_{FB} + r_{std}) I_{CCS}]$.

The input noise (~10^{-14} V) of a SQUID picovoltmeter is a function of the source resistance and temperature, the voltage noise due to the standard resistor and the inherent current noise of the SQUID (I_N). The system noise (in volt/√Hz, referred to the input) is given by:

$$V_{rms} = \sqrt{4 k_B T_{source} R_{source} + 4 k_B T_{r_{std}} r_{std} + I_N^2 R_{source}^2} \qquad \text{Equation 14}$$

Measurement of the Johnson noise in a resistor ($\langle V^2 \rangle = 4 k_B T R \Delta f$ where Δf is the bandwidth of the measurement) can be used to determine absolute temperature [11]. Commercially available LTS SQUIDs have equivalent device temperatures < 1 μK and are suitable for noise thermometry [11]. Resolutions of 10^{-11} Ω can be achieved for $R_X < 10^{-2}$ Ω. Other applications of picovoltmeters include measurements of thermopower, thermal EMFs (thermocouples), and infrared bolometers.

7.2 ac measurements

The SQUID can also be used as the null detector in an ac bridge circuit (Figure 33e) to measure both resistive and reactive components of a complex impedance. The unknown impedance **Z** is excited by a current generated by an oscillator voltage which is attenuated by a precision ratio transformer (λ). The difference between the voltage developed across the unknown impedance **Z** and that developed in the secondary of a nulling mutual inductor **m** is applied to the input of the SQUID circuit. The primary current in **m** is proportional to the oscillator voltage and defined by the setting of the ratio transformer (α). An additional reactive current is supplied by a second

ratio transformer (β) which causes the primary current to be passed through a capacitor rather than a resistor thus generating a 90° phase shift in the voltage applied to **m**. The amplified off-balance signal which appears at the output of the SQUID control electronics can be displayed by means of a lock-in amplifier tuned to the oscillator frequency. As mentioned earlier, the sensitivity is limited inherently by Johnson noise in the resistive components of the unknown (including the potential connections) and by the device noise of the SQUID sensor. Assuming $I_N \approx 1$ pA/√Hz, such a system is capable of measuring self and mutual inductances between 10^{-12} H and 10^{-3} H with $1{:}10^6$ part resolution [11, 70].

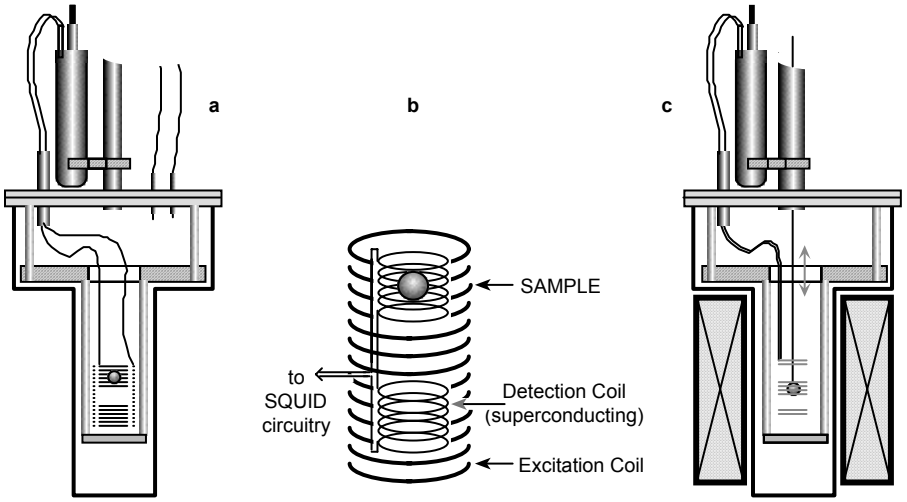

Figure 34 Magnetic Susceptibility measurement apparatus (liquid helium dewar not shown). (a) ac susceptibility, (b) signal and excitation coil details, (c) second derivative oscillating magnetometer for dc measurements with external dc field coils

Figure 34a shows a typical experimental setup for measurement (Figure 33f) of ac susceptibility. Such a configuration can be used for thermometry by measuring the low (mT) field magnetic susceptibility of paramagnetic salts such as $Ce_2Mg_3(NO_3)_{12} \cdot 24\ H_2O$—usually referred to as CMN [72].

It is important not to couple the excitation signal into the detection circuit. The excitation and detection coil should not have the same gradient order. Otherwise, the excitation signal will be applied to the detection coil. For example, using a solenoidal excitation coil (gradient order = 0) with a 1st derivative detection coil (Figure 34b) minimizes the current flowing through the detection coils. Likewise, a 1st order gradient excitation coil will couple no current through a 2nd order detection coil (assuming they have a common center). Since gradiometer coils can not be perfectly wound, the use of external feedback (§4.2) may be needed to further reduce the contribution of the excitation coil into the SQUID detection circuit.

7.3 Variable Temperature SQUID magnetometer/susceptometers

Instead of using a secondary ac excitation coil (Figure 33f and Figure 34b), a dc field can be used to magnetize samples. Typically the field is fixed and the sample moved into the detection coil's region of sensitivity (Figure 34c). The change in detected magnetization is directly proportional to the magnetic moment of the sample.

Commonly referred to as SQUID magnetometers, these systems are properly called SQUID susceptometers. They have a homogeneous superconducting magnet to create a very uniform

field over the entire sample measuring region and the superconducting pickup loops. The magnet induces a moment allowing a measurement of magnetic susceptibility. The superconducting detection loop array is rigidly mounted in the center of the magnet. This array is configured as a gradient coil to reject external noise sources. The detection coil geometry determines what mathematical algorithm is used to calculate the net magnetization. Oppositely paired Helmholtz coils [74] (Figure 35), transverse detection coils, first and second derivative gradiometers (*e.g.*, Figure 19b & d, Figure 34c) have all been successfully used.

Figure 35 shows input circuitry consisting of a superconducting circuit having two opposed Helmholtz detection coils and the SQUID input coil connected in series. The current that flows in response to a change in flux is given by $\Delta I = \Delta\Phi / L$ where ΔI is the current induced in the circuit by the flux change $\Delta\Phi$, and L is the circuit's inductance. This is analogous to the response of a conventional (resistive) detection coils (such as used in a vibrating sample magnetometer)

$$\frac{dI}{dt} = \frac{d\Phi}{dt} \bullet \frac{1}{L} = -\frac{V}{L} \qquad \text{Equation 15}$$

where V is the voltage induced across the coils. The important difference is that for the superconducting case, the induced current is independent of the *rate* of flux change. This provides uniform response at all frequencies (*i.e.*, true dc response) and allows the sample to be moved arbitrarily slowly without degrading performance. In this particular example, the sample is moved between the two counter-wound detection coils. As the sample passes through a coil, it changes the flux in that coil by an amount proportional to the magnetic moment (M) of the sample. The peak-to-peak signal from a complete cycle is thus proportional to twice M. The SQUID sensor (shielded inside a Nb can) is located where the fringe fields generated by the magnet are less than 10 mT. The detection coil circuitry is typically constructed using NbTi. This allows measurements in applied fields of 9 T while maintaining sensitivities of 10^{-8} emu. Thermal insulation (not shown in Figure 35) is placed between the detection coils and the sample tube to allow the sample temperature to be varied.

While persistent mode superconducting magnets are extremely stable, field drift at the 1 ppm/hour level into a magnetometer input coil can be at the nT/sec level. Again, the use of gradient detection coils can reduce this by 2-3 orders of magnitude. The susceptometer shown in Figure 35 had a NbTi shield surrounding the detection coil. When the field was changed, the NbTi shield was heated above T_c, and then cooled when the desired field strength was reached. The NbTi shield trapped the trapped the field supplied by the superconducting magnet and gave the system much greater field stability than if no shield was present. The disadvantage of this method was the time needed to change fields (due to the heating and cooling of the NbTi shield) and its inability to do swept field measurements.

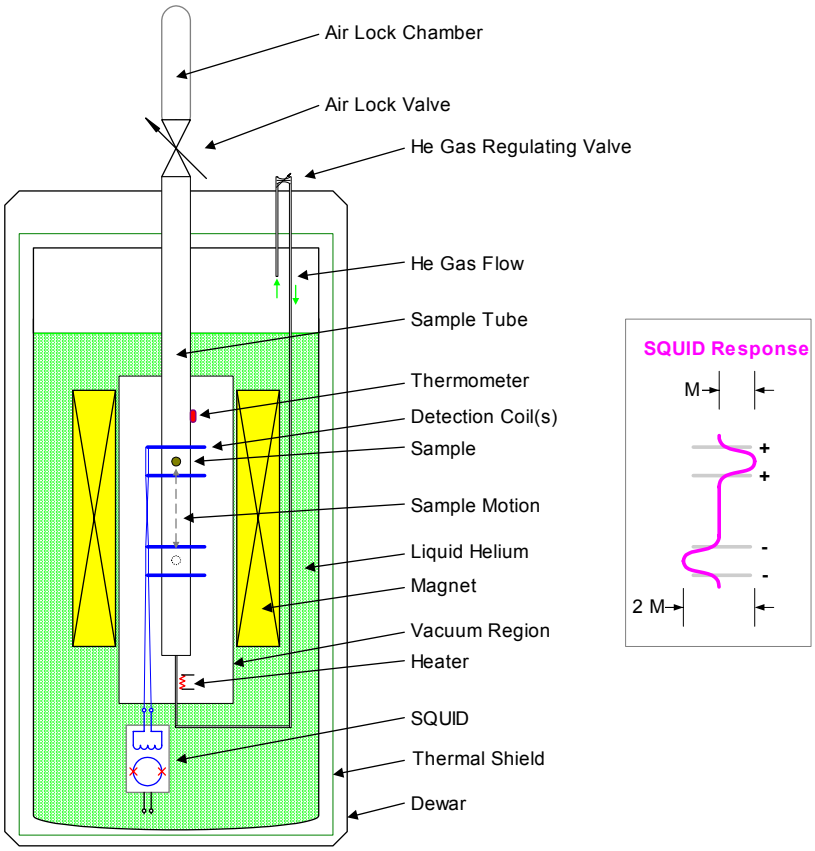

Figure 35 Variable Temperature Susceptometer (various electrical leads omitted for clarity). The trace on the right shows the response of the detection coil(s) as a function of sample position height.

The most popular detection coil configuration is that of a 2nd order coil configuration [75]. In this situation, the detected output is compared with that of an ideal response to determine the magnetization. This technique has the advantage of eliminating noise. Additionally, the intentional choice not to use a NbTi shield allowed swept field scans to be performed. Coupling two axial channels of differing gradient order (*e.g.*, 1st and 2nd) can significantly improve noise rejection. The detection coil does not necessarily need to be in an axial configuration. Planar gradiometers have been used to detect the onset of superconductivity in diamond pressure cells [76]. Placement of secondary excitation coils can allow ac susceptibility measurements approaching 10^{-8} emu to be made in the presence of a significant dc bias field.

The use of a variable temperature insert can allow measurements to be made over a wide range (1.8 K – 400 K). Typically, the sample temperature is controlled by helium gas flowing slyly past the sample (Figure 35). The temperature of this gas is regulated using a heater located below the sample measuring region and a thermometer located above the sample region. This arrangement ensures that the entire region has reached thermal equilibrium prior to data acquisition. The helium gas is obtained from normal evaporation in the dewar and its flow rate is controlled by a precision regulating valve. The use of an oven probe can raise the sample temperature to 800+ K (at the expense of smaller sample measurement volume). If the system is to have top loading access, then the central (sample) tube should be constructed from a low conductivity material (*e.g.*, 300 series SS) rather than high conductivity like Al or Cu (*c.f.*, eq. 13). BeCu is an alternative choice if time constants faster than 10 msec are needed. Rock

magnetometers (§8.3) use sample tubes made from fiberglass/epoxy rather than stainless steel primarily because metallic tubes conduct RFI into the pickup coil region and can cause SQUID noise. This also allows for time constants that approach microseconds. A disadvantage of insulating sample tubes is their very long thermal time constants.

When measuring changes in magnetic moment resulting from a variable other than temperature or magnetic field (*e.g.*, an applied acoustic or rf pulse), the sample is centered in one of the paired detection coils (Figure 35) and the SQUID output monitored as a function of the stimulus. This technique is useful for studying flow/stop-flow reactions, gas adsorption, catalytic processes, optical dissociation or similar time-dependant phenomena. Reference [77] gives a good overview of variable temperature SQUID susceptometer measurements.

A SQUID can also be used as an amplifier in a Vibrating Sample Magnetometer (VSM). The VSM [78] moves the sample though a coil at a fixed frequency. Conventional VSMs use resistive coils and conventional amplifiers to get sensitivities at the 10^{-5} emu level. The use of a SQUID can allow sensitivities at the 5×10^{-9} emu level [79].

7.4 NMR

NMR signals [80]) can be measured by placing a sample (*e.g.*, protons or ^{19}F) in the center of SQUID detection coils and either sweeping the external field or applying an rf excitation to the sample. The same experimental concept can be used to measure electron paramagnetic resonance (EPR) signals. Although limited to 100 ppm field uniformities, SQUID susceptometers (*e.g.*, SHE VTS (Figure 35), Quantum Design MPMS (Figure 34c) or Conductus χMAG) are excellent platforms for basic demonstrations of NMR measurements.

The relationship between the resonant frequency and applied magnetic field is given by the gyromagnetic ratio γ (for protons, γ = 42.6 MHz/T). Higher fields are desirable in order to improve signal-to-noise ($S/N \propto H^2$). For some materials, γ is so small (*e.g.*, ^{39}K where γ = 1.99 MHz/T) that a detection frequency of 383 MHz (equivalent to 9 T for protons) would require an applied field of 193 T. The bandwidth of commercially available SQUID electronics (< 100 kHz) places limits on NMR detection. However, custom made SQUID electronics [22] can allow measurements to be made at MHz frequencies. The use of SQUID detection coils can offer significant improvements over conventional coils at a given field strength or allow equivalent signal-to-noise at lower applied fields (reducing magnet cost).

Similarly, SQUIDs offer improved signal-to-noise for measurements of nuclear quadruple moments [81].

7.5 Other measurement techniques

Because SQUID magnetometers are vector devices, they can detect rotational movement of a magnetometer coil in the Earth's magnetic field (~50 μT) as small as 10^{-3} arc-seconds. SQUIDs have been used for more esoteric applications including temperature measurements with resolution near 10^{-12} kelvin[82] and to measure position for gravity wave detectors with sub Å resolution [83]. SQUIDs are also used as ultra high resolution angular position detectors in the Gravity Probe B program, which aims to test several predictions of Einstein's General Theory of Relativity [84]. Four SQUIDs in an Earth-orbiting satellite measure deviations in gyroscope spin axis direction with nanoradian resolution. SQUIDs have been used in searches for dark matter

such as Weak Interacting Massive Particles (WIMPs) [85] and Axions [86] along with attempts at detecting magnetic monopoles [87] and free quarks [88].

While this review is focused on low frequency applications, there is a need for higher frequency SQUID instruments. In particular, applications such as axion detectors, radio astronomy and NMR (§7.4) are examples where SQUIDs offer superior sensitivity at frequencies that can approach 1 GHz [89].

7.6 Absolute field measurements

7.6.1 Flip-coil magnetometers

As mentioned in §3.5, conventional SQUIDs are sensitive to *relative* changes only. It is possible to make a SQUID magnetometer into an absolute magnetometer by rotating a coil 180° such that the field change (max to min) is twice the total field (in the axis of rotation). To determine the total field, this need to be done in all three axes. Such "flip-coil" magnetometers have been constructed. One example used a cm diameter coil that was rotated using plastic bevel gears actuated from room temperature to achieve field resolution at the pT level. In the case of "large" (*i.e.*, μT total fields if pT resolution is desired) fields, caution must be taken not to exceed the dynamic range of the electronics. If the speed of rotation is slow enough to allow for flux counting (adding the number of resets of the electronics), the dynamic range of the measurement can be extended by orders of magnitude.

7.6.2 Superconducting Quantum Interference Filters

An array of different superconducting loop sizes, either in series or in parallel configuration, acting as grating structures, can be used to form a Superconducting Quantum Interference Filter (SQIF). The effect of the superposition of the signals of the different loops is significant attenuation of all voltage modulation except for zero applied magnetic fields, where a large unique voltage peak evolves. This can allow absolute field measurements to be made at sensitivities approaching a few fT/√Hz [90].

8 GEOPHYSICAL APPLICATIONS

SQUID magnetometers are used to measure the Earth's magnetic field (Figure 28) at frequencies ranging between 1 kHz and 10^{-4} Hz. Geophysical detection can be classified according to the type of energy source used by the method - seismic (acoustic energy), electromagnetic (natural and man-made), electrical (natural and man-made), magnetic (Earth's magnetic field), gravity (Earth's gravitational field), and radiometric (generally gamma ray) emissions from subsurface materials. Measurements made by electrical and electromagnetic methods are primarily sensitive to the resistivity of the subsurface materials at frequencies below 100 kHz. Above 100 kHz, the methods are sensitive to both resistivity and the dielectric constant of the subsurface materials.

In comparison to large induction coils, SQUID magnetometers are easier to deploy and use (allowing SQUID sensors to be placed down boreholes), operate to dc (with flat phase response) and avoid giving undue emphasis to high frequency phenomena such as the ubiquitous lightning induced sferics. Their wide bandwidth allows the use of a single instrument as compared to induction coils where multiple coils may be required. The high dynamic range of SQUIDs can allow dinural range variations (± 100 nT) to be tracked while still maintaining full sensitivity.

The use of SQUIDs in electromagnetic prospecting methods can be divided into passive and active methods:

8.1 Passive Methods

Passive methods such as MT (Magnetotellurics) and AMT (Audio MT) use the interaction of the solar wind in the ionosphere as an electric and magnetic field generator. In general, they cover the frequency range of mHz - 10 Hz and 10 Hz – 1 kHz, respectively.

8.1.1 Magnetotellurics (MT)

Magnetotellurics can be used to determine the electrical conductivity distribution of the Earth's crust by measuring the Earth's electric and magnetic field [91]. Because the Earth is a good electrical conductor compared to the air, the electrical field generated in the ionosphere (due to the solar wind) is reflected at the Earth's surface, with components of both the electric and magnetic field decaying as they penetrate into the Earth. The electric field (as a function of frequency) is related to the magnetic field via an impedance tensor (Z in units of mV/km-nT) where:

$$
\begin{aligned}
&E(\omega) = Z\,H(\omega)\\
&E_x(\omega) = Z_{xx}H_x(\omega) + Z_{xy}H_y(\omega)\\
&E_y(\omega) = Z_{yx}H_x(\omega) + Z_{yy}H_y(\omega)\\
&\rho_{ij} \approx 0.2\left|Z_{ij}\right|^2\tau; \quad \delta \approx 0.5\sqrt{\rho\tau}
\end{aligned}
$$

Equation 16

By measuring E and H, the electrical resistivity of the Earth (ρ in Ω-m) can be calculated (Figure 36). By measuring at different frequencies, the resistivity can be determined as a function of skin (penetration) depth, (δ (in km) ≈ ½√ρτ kilometers, where τ is the period of the electromagnetic wave).

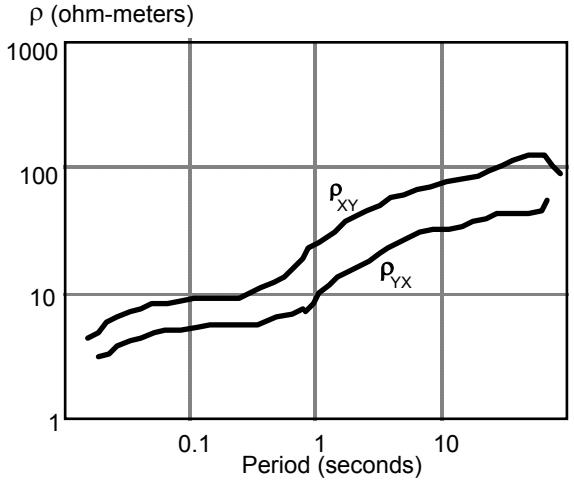

Figure 36 calculated resistivity as a function of frequency

By measuring at multiple positions and combining that information with geologic and geophysical data, it is possible to create a geologic model that can be used to indicate suitable drilling sites (Figure 37).

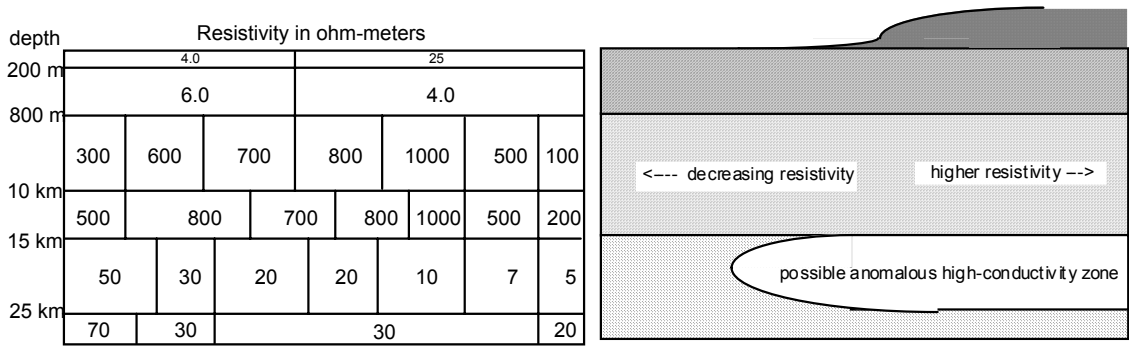

Figure 37 Calculated 2D inversion map and resultant geologic interpretation. Horizontal span ≈ 20 km. After [92]

Magnetotellurics has been used for oil exploration in the overthrust belts of the western United States and deep sediments of the Gulf coast region. The increased conductivity of hot saline regions associated with geothermal sites makes MT well suited for locating hydrothermal reservoirs. The use of multiple magnetometers (*i.e*, remote reference magnetotellurics [93]) can significantly reduce the influence of correlated noise.

SQUID magnetometers for MT are typically 3-axis (B_x, B_y, B_z). Since most MT surveys are done in remote areas, environmental noise is less of a consideration, although the sensitivity desired (< 100 fT/√Hz) still makes even distant power-line frequencies observable.

8.1.2 Magnetic Anomaly Detection (MAD)

Knowledge of the total magnetic field gradient (**∇B**) of an object can allow determination of its magnitude and direction [94]. From Maxwell's Equations, four of the gradients are redundant (*e.g.*, $\partial B_y/\partial x = -\partial B_x/\partial y$). Thus only five gradient components are necessary to determine **∇B** (eq. 17.

$$\begin{pmatrix} \frac{\partial B_x}{\partial x} & \frac{\partial B_x}{\partial y} & \frac{\partial B_x}{\partial z} \\ \frac{\partial B_y}{\partial x} & \frac{\partial B_y}{\partial y} & \frac{\partial B_y}{\partial z} \\ \frac{\partial B_z}{\partial x} & \frac{\partial B_z}{\partial y} & \frac{\partial B_z}{\partial z} \end{pmatrix} \Leftrightarrow \begin{pmatrix} \frac{\partial B_x}{\partial x} & \frac{\partial B_x}{\partial z} \\ \frac{\partial B_y}{\partial x} & \frac{\partial B_y}{\partial z} \\ & \frac{\partial B_z}{\partial z} \end{pmatrix} \qquad \text{Equation 17}$$

An 8-element tensor array can also be made from pure magnetometer elements. This is helpful when axial gradiometers are not feasible (*e.g.*, HTS SQUID sensors).

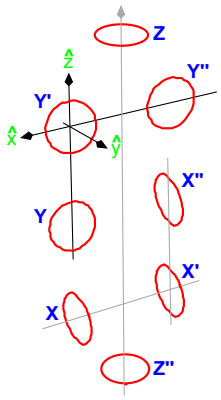

$$\frac{\partial B_X}{\partial x} = X - X'$$
$$\frac{\partial B_X}{\partial z} = X - X''$$
$$\frac{\partial B_Y}{\partial x} = Y' - Y''$$
$$\frac{\partial B_Y}{\partial x} = Y' - Y''$$
$$\frac{\partial B_Z}{\partial z} = Z - Z'$$

$$B_X = \frac{1}{3}(X + X' + X'')$$
$$B_Y = \frac{1}{3}(Y + Y' + Y'')$$
$$B_Z = \frac{1}{2}(X + Z'')$$

Figure 38 Tensor made from discrete magnetometers

It should be noted that superconducting magnetometers are vector devices, and motion in the Earth's magnetic field produces an output that can mask the desired signal. For airborne gradiometer systems, noise cancellation (compensation of motion–induced artifacts) via electronic balancing is the critical technology, not SQUID sensitivity. The detection (distance) limit for such a gradiometer system is proportional to the fourth root of magnetic moment of the object being detected. MAD has potential uses in mineralogical surveys and unexploded ordinance [95]. MAD has also been used for detection of vehicles and naval vessels (Figure 39).

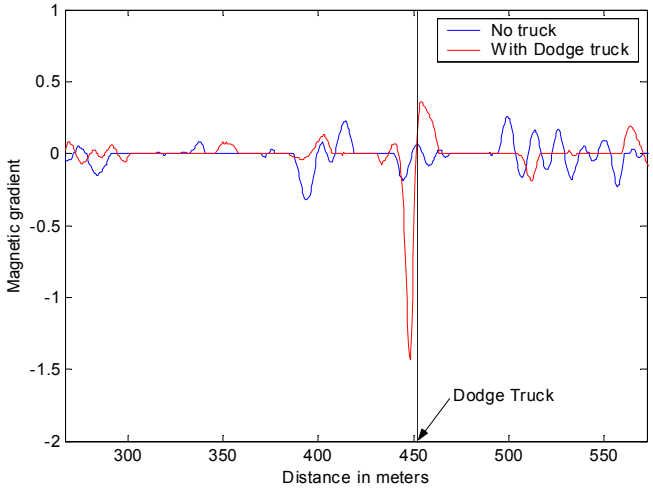

Figure 39 Output of HTS planar gradiometer flying over a commercial vehicle (arbitrary units). The gradiometer was inside a tail mounted stinger on a Cessna Caravan airplane. Courtesy Sky Research.

8.2 Active Methods

Rather than using the electromagnetic field generated by the solar wind, active methods create a time dependant magnetic field generated by a loop driven by an electric current, with the magnetometer detecting the induced field. Measurements can either be in the time (e.g., Transient ElectroMagnetics - TEM) or frequency (e.g., Controlled Source AMT - CSAMT) domains.

Transient ElectroMagnetics (TEM), a time-domain method, uses large excitation coils (covering up to 10^4 m^2) with currents in the order of 10 A. Pulse lengths range from μsec up to 1 sec. Controlled Source AMT (CSAMT), a frequency-domain method, uses current that is fed into the earth by a grounded dipole with several hundred meter lengths.

8.2.1 Transient electromagnetic pulses (TEM)

Transient ElectroMagnetics (TEM), a time-domain method, uses large excitation coils (covering up to 10^4 m^2) with currents in the order of 10 A. Pulse lengths range from µsec up to 1 sec. The magnetic fields generated by the loop can be measured with a three-axis magnetometer or an 8-element tensor array. The advantage of the 8-element tensor array is its ability to locate the object being excited by the electromagnetic pulse. Figure 40 shows the key elements of a TEM measurement using relatively small field excitation coils [96]. Targets were centered in the transmitter coil, which had 3 turns with a current of .01 amp (65 nT effective field).

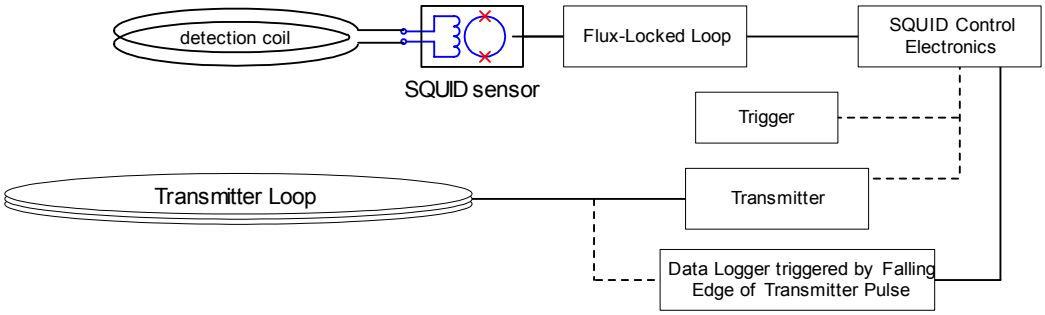

Figure 40 Block diagram of controlled source electromagnetic system

Figure 41a shows the five independent tensor gradients over the 10 cm diameter hollow (30 mil thick) copper sphere. As expected, all of the gradients have defined similar time constants (about 0.5 msec) for the sphere. The longest computed time constant for the copper sphere is 0.9 msec. This variation in the uniformity of the source pulse field over the target leads to an effective shorter time constant than would be expected. Figure 41b shows the tensor gradients over the 30 mm projectile. For this target, it appears that the geometric variation in the source pulse field has resulted in some distortion of the gradient response. However, it does illustrate that the tensor gradients from the 30 mm target are significantly different which can be used for discrimination of target type.

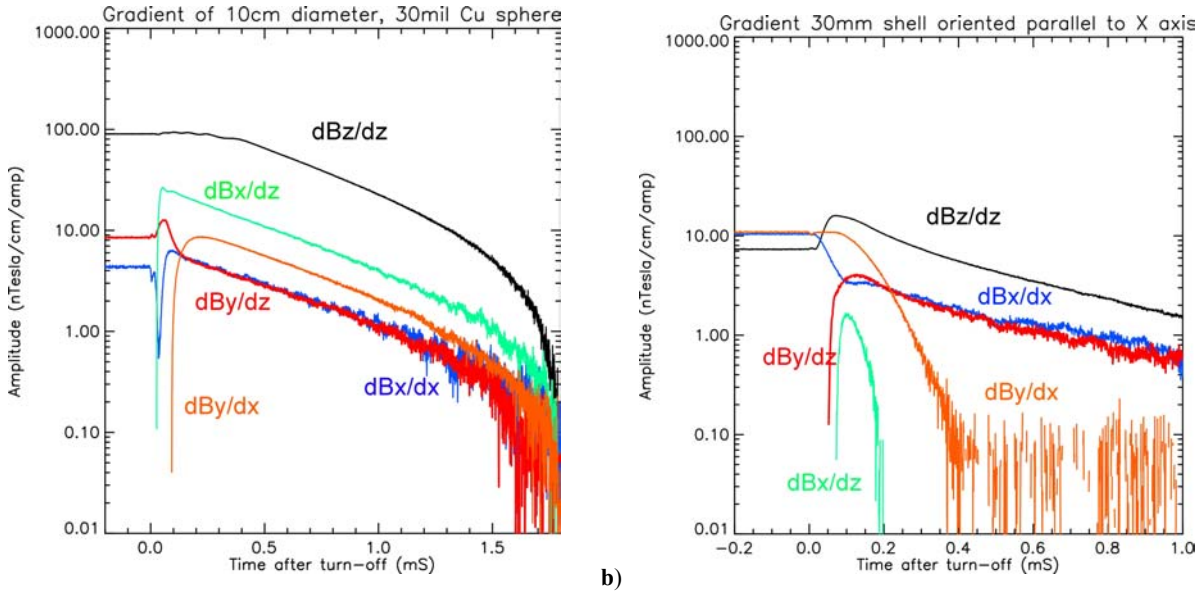

Figure 41 1 µsec interval data from for a) copper sphere and b) artillery shell

Reference [97] is a good introduction to TEM using a using a 3-axis coil array. Because of the vector nature of SQUID magnetometers, the use of SQUIDs in mobile applications requires special attention to motion-induced noise. Reference [98] discusses a "hand held" system while [99] discusses an airborne system.

8.3 Rock Magnetometry

Knowledge of the magnetic field orientation of a rock or core sample can give information as to how the rock was formed. By changing the thermal history of the sample, it may be possible to determine the Curie and/or Néel temperature of the rock's constituents. By raising the applied field above the saturation field of any ferromagnetic components, it may be possible to study paramagnetic components. Normally a 3-axis rock magnetometer is used for paleomagnetic measurements. By using orthogonal field coils (B_x, B_y, B_z) or rotating the sample in a single coil, the anisotropy of the sample can be determined. Time dependant behavior can also be studied after rapid changes in either temperature or applied field.

There are multiple ways to measure the remnant magnetic moment of ore samples. The most convenient way is to place the sample inside orthogonal field coils. The use of LTS SQUID sensors allow sensitivities of 10^{-10} emu (10^{-13} Am^2) to be reached, equivalent to 10^{-8} A/m for a 10 cc rock sample. Room temperature access to the measurement region is desirable. SQUID rock magnetometers are quite similar to SQUID susceptometers (§7.3) in terms of their basic design. The main differences are larger sample tube bore size (7.6+ cm rather than 1 cm), a more limited temperature range (usually fixed at room temperature rather than variable temperature, and measurement at zero applied field (although measurements in applied fields can be made). If the region of sensitivity of the detection coil(s) is small relative to the sample size, it may be possible to measure the magnetization as a function of position by slowly moving it through the coil's sensitive region. A major advantage of the LTS rock magnetometer is its ability to shield environmental noise. This is in part due to the use of long metallic (usually stainless steel) sample tubes and a sample region that is surrounded by either a superconducting shield, a superconducting magnet or both.

A variation on the traditional rock magnetometer is the spinner magnetometer. In this case, the sample is rotated beneath a SQUID magnetometer. By rotating the sample on two axes, the orientation and magnitude of the rock's magnetization can be determined. Sensitivities of 4×10^{-5} A/m have been achieved [100].

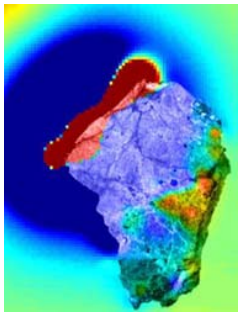

Figure 42 Magnetic microscope image of Martian meteorite ALH84001.

SQUID microscopes (§9.3) can also be used to image magnetic domains (Figure 42) in slices taken from rock and ore samples [101] with sub-mm spatial resolution. This can yield highly detailed maps with the ability to resolve a single grain in a rock.

9 NON-DESTRUCTIVE TEST AND EVALUATION

Magnetic sensing techniques (Figure 43) such as eddy current testing have been used for many years to detect flaws in structures. A major limitation on their sensitivity is the skin depth, λ (the distance where the field is attenuated by a factor 1/e) of metallic materials. For a sinusoidal varying wave, $\lambda = \sqrt{\rho/\pi\mu_o f}$ where f is the frequency of the applied field, ρ the electrical resistivity and μ_0 is the magnetic permeability of free space. Because SQUID sensors have true dc response and superior sensitivity, they can see "deeper" into metallic structures. dc response also means that they can detect remnant magnetization—without the need for externally applied magnetic fields. Their flat frequency response and zero phase distortion allow for a wide range of applications.

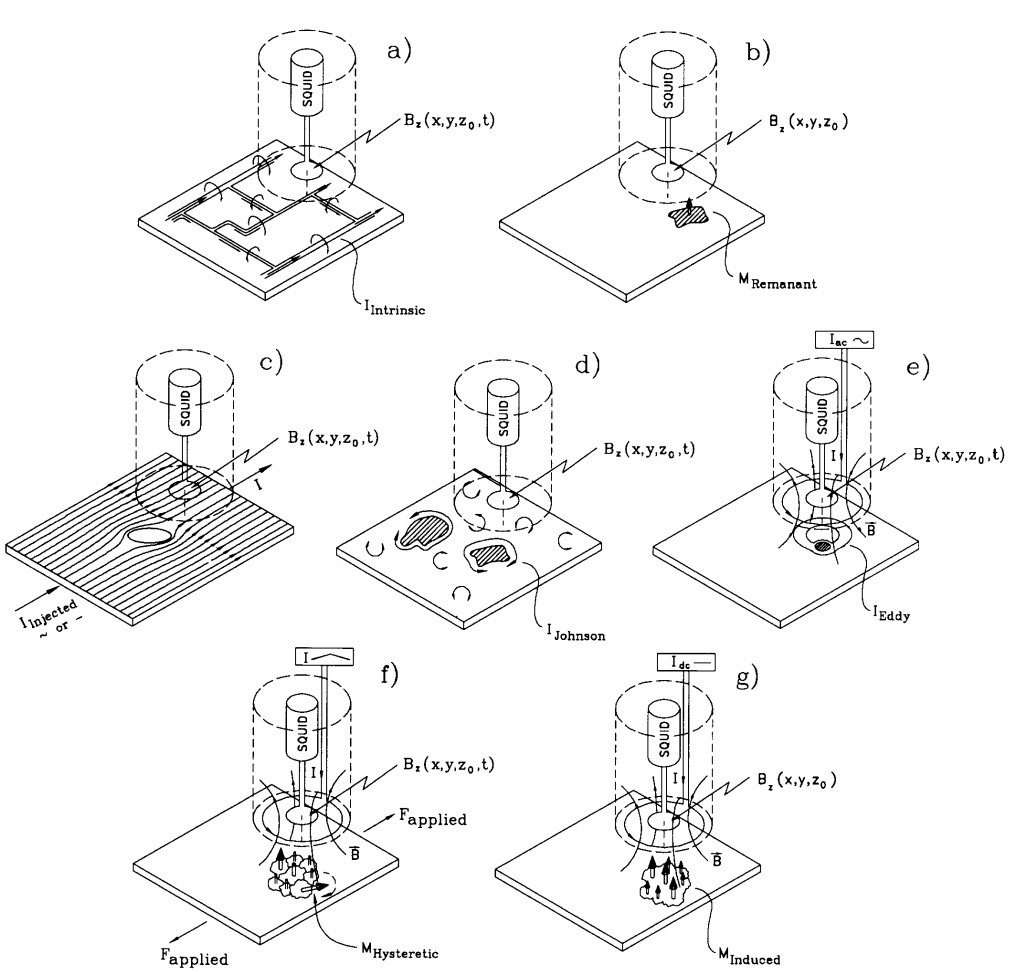

Figure 43 Measurement configurations for SQUID NDE: a) intrinsic currents, b) remnant magnetization, c) flaw-induced perturbations in applied currents, d) Johnson noise or corrosion activity in conductors, e) eddy currents induced by an applied ac magnetic field, f) hysteretic magnetization by application of stress or an applied field), g) diamagnetic and/or paramagnetic materials in an applied field. Courtesy J. P. Wikswo

The presence or absence of magnetic materials makes it possible to detect perturbations or flaws. Figure 44 shows the magnetic field due to holes in a ferromagnetic plate. This leads to the

potential application of SQUIDs is in detection of stress or corrosion in reinforcing rods (rebar) used in bridges, aircraft runways or buildings.

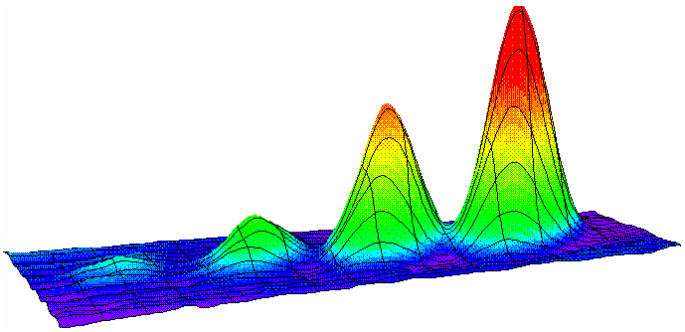

Figure 44 Scan of 1, 3, 5, and 10 mm holes in a steel plate

9.1 Measurement Techniques

Magnetic susceptibility is normally measured by applying an external magnetic field (**H**) in the same orientation as the detection coil(s). If the material being studied is isotropic, the response of the material to the applied field will be sufficient to determine the material's magnetic properties. For the purposes of this discussion, let us assume that that both the field and detection coils are oriented vertically (in the z-direction).

If the material is anisotropic, there will be field components generated in directions other than the (z-axis) orientation of the field coil. In this situation, transverse detection coils (*e.g.*, coils oriented in the x- or y-directions) would be needed to detect the anisotropic response. Figure 45 shows the tail section of a microSQUID™ system with "vector" (B_x, B_y and B_z) detection coils.

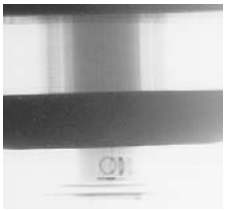

Figure 45 X-ray of vector set (B_x, B_y, B_z) of detection coils (2 mm diam.)

Alternatively, the field (*e.g.*, H_x or H_y or both) could be generated transverse to the (B_z) detection coil(s). Any anisotropic response would be detected in the vertically oriented detection coil.

Superconducting magnets can generate dc fields > 0.1 T a few cm beneath the end of the magnet. Placing the superconducting magnet in a persistent mode minimizes or eliminates field drift. This can allow detection at or near the theoretical sensitivity of the detection coil. Because of the inductance of multi-turn coils of sufficient turns to generate large fields, the maximum field strength of ac magnets are significantly smaller (fractions of a mT rather than fractions of a T) than persistent mode superconducting magnets. Thus the ultimate sensitivity of a dc susceptibility measurement system will be greater than an ac susceptibility measurement system.

In flaw detection, it may be desirable to have the a uniform current flow that creates a uniform magnetic field. Any distortions (cracks, imperfections, inclusions, etc.) will cause the current path(s) to be distorted with a resultant non-uniform magnetic field. Imaging of the non-uniform magnetic field will allow identification of the causal distortion(s). A sheet inducer (Figure 46) can be used to generate horizontal currents [102].

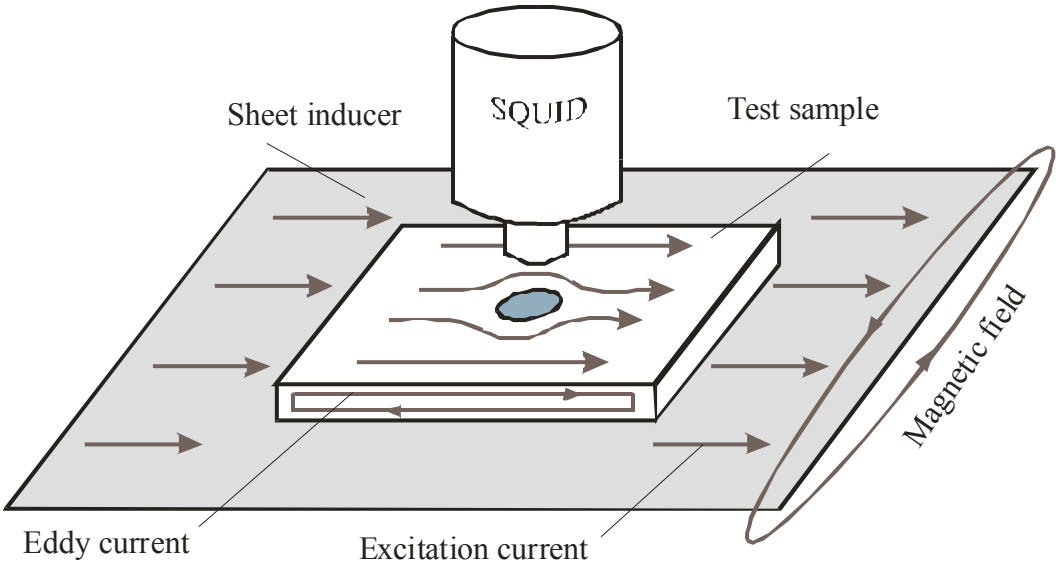

Figure 46 Sheet Inducer

9.1.1 Magnetization and Strain

Stress and strain can have significant effects on the magnetic properties of materials.

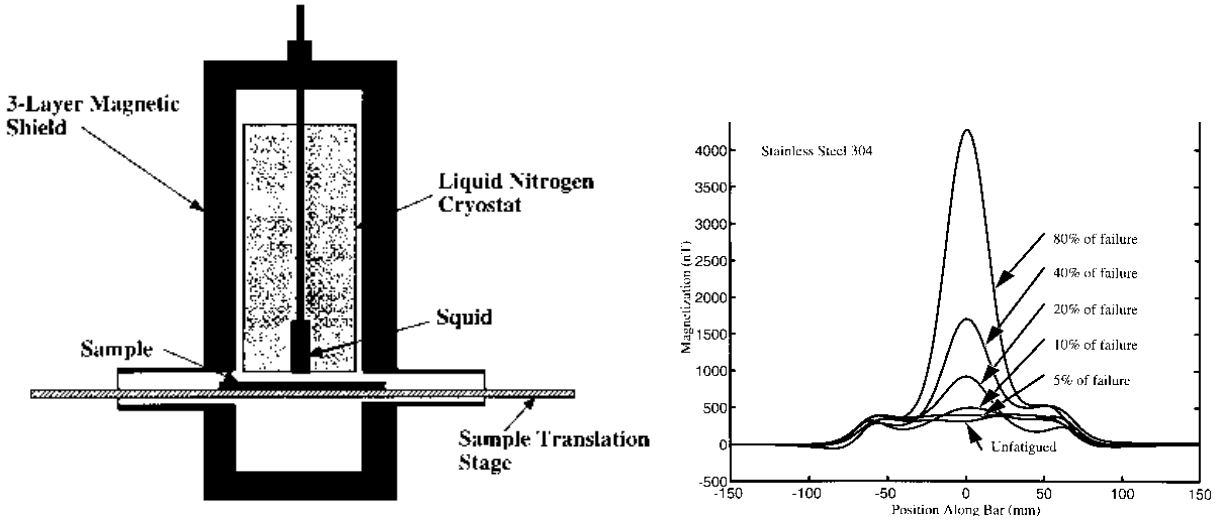

Figure 47 Side view of NLD-510 dewar in MS-830 showing customer constructed sample translation stage and measurements of 304 stainless steel as a function of % of failure [103]

A particular advantage of magnetic sensing is in examining defects beneath insulating barriers. For example, a cladded pipe with asbestos lagging can be quickly examined because the insulating barriers are virtually invisible to magnetic detection—the asbestos need not be removed or cut into. A similar use would be to detect corrosion underneath paint or other opaque coverings.

Another potential application of SQUIDs is in detection of stress or corrosion in reinforcing rods used in bridges, aircraft runways or buildings. Certain types of steel (*e.g.*, Tripp steel) take on an increasing magnetic dipole character as it is strained (Figure 48). At zero strain, the strain sensor has a multipole nature (looking like a sine wave with numerous maxima and minima and an

amplitude of a few volts. When the sensor is strained, the magnetic field pattern becomes pure dipolar in nature with the amplitude proportional to the applied strain.

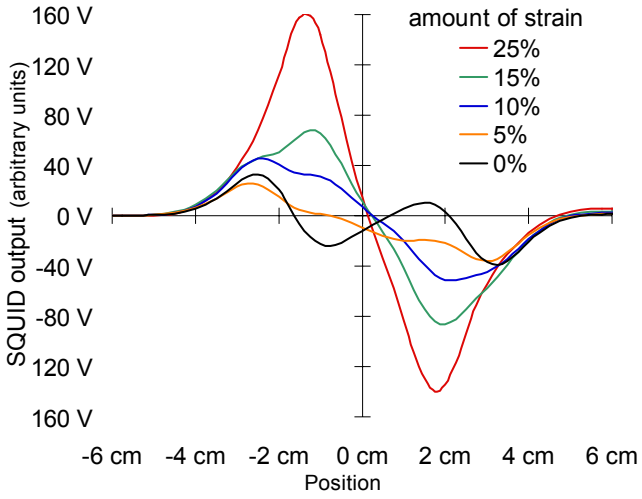

Figure 48 On-axis Magnetization of Strain Sensor

9.1.2 Effect of Intervening Materials

Unlike eddy current measurements, which have a skin depth that is frequency dependant, the true dc response of a SQUID magnetometer allows measurements with little, if any, effect from intervening materials. Figure 50 shows a linear scan of a Tripp steel strain sensor whose relative strain is estimated at ~10%.

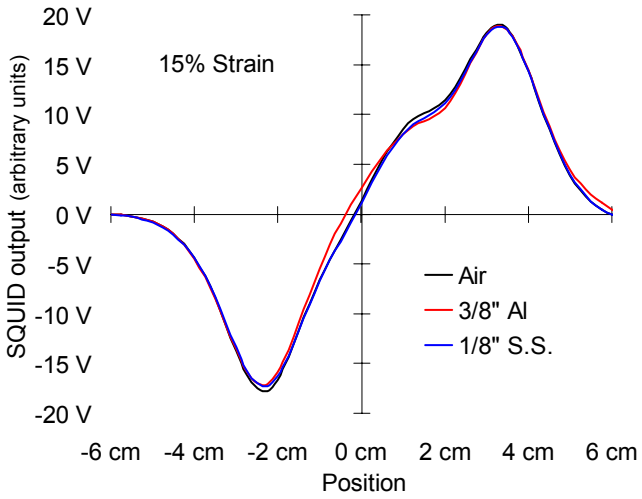

Figure 49 effect of intervening materials

The strain sensor was measured by a LTS SQUID gradiometer in an unshielded environment, first with an air gap between the sensor and the SQUID magnetometer (black trace). A 3/8" aluminum plate was then placed gap between the sensor and the SQUID magnetometer yielding the red trace. Finally a 1/8" stainless steel plate was placed between the sensor and the SQUID magnetometer giving the blue trace. As can be seen, the dc response of SQUID magnetometers allow penetration depths not possible with eddy current or other ac measurement techniques.

Intervening materials can also be non-metallic. Figure 50 shows 2-D magnetic field maps of the same embedded strain sensor measured beneath a variety of intervening materials.

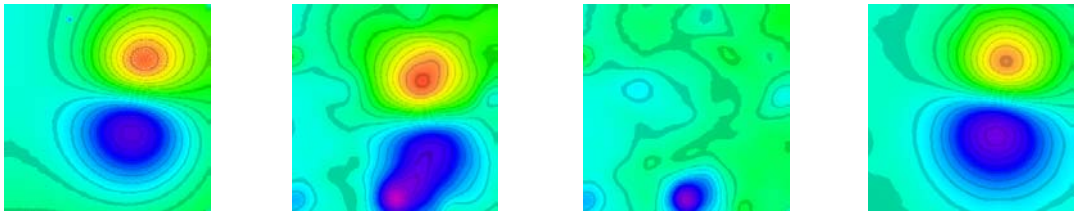

Figure 50 Magnetic field maps of a room temperature embedded strain sensor under a 4 cm thick concrete overcoating. **A** - bare sensor showing dipole characteristics, **B** - sensor under concrete, **C** - bare concrete. Image **D = B – C** is a digital subtraction of B and C showing that it is possible to image objects deep underneath magnetically complex coverings. The scans cover a 6 cm x 6 cm area.

It should be noted that the peak-to-peak heights of the maxima and minima in Figure 50A and Figure 50D are the same indicating no attenuation of the detected signals.

9.2 Sensitivity Calculations

In reality, the purpose of NDE measurements of most samples is not to determine the magnetic field emanating from the sample, but to determine the magnetic moment(s) of the sample's constituents. Thus, the best figure of merit in assessing magnetic scanners and microscopes is the minimum detectable magnetic moment $\boldsymbol{M}_{min}$. For purposes of calculating $\boldsymbol{M}_{min}$, we can model small samples as a small loop where the magnetic moment is the equivalent current in the loop times the area of the loop (A-m^2). For a bare SQUID with no input coupling coil (typical of HTS SQUIDs used in magnetic microscopes), the flux in the SQUID is given by:

$$\Phi_{SQUID} = B_{SQUID}\, A_{SQUID} = m_{SQ\text{-}sample}\, I_{Sample}, \qquad \text{Equation 18}$$

where B_{SQUID} is the field in the SQUID loop, A_{SQUID} is the area of the SQUID loop, $m_{SQ\text{-}sample}$ is the mutual inductance between the SQUID loop and the sample (which is modeled as a tiny loop) and I_{Sample} is the equivalent current of the sample. Rearranging eq. (18) by substituting the minimum detectable field change and replacing I_{Sample} by $\boldsymbol{M}_{min}/A_{Sample}$, where A_{Sample} is the area of the sample gives:

$$B_N\, A_{SQUID} = m_{SQ\text{-}sample}\, \boldsymbol{M}_{min} / A_{Sample} \qquad \text{Equation 19}$$

$$\text{Thus, } \boldsymbol{M}_{min} = B_N\, A_{SQUID}\, A_{Sample} / m_{SQ\text{-}sample} \qquad \text{Equation 20}$$

If a SQUID with an input coil and a separate detection coil (*e.g.*, Figure 18) is used, then,

$$\boldsymbol{M}_{min} = I_N\, (L_{SQUID} + L_{Detection\ Coil})\, \mathrm{A_{Sample}} / m_{SQ\text{-}sample} \qquad \text{Equation 21}$$

with the SQUID's input current noise set to be equal to the current induced in the coil. Using the notation of §4.4 - 4.6 for an axial gradiometer detection coil, eq. (21) becomes

$$\boldsymbol{M}_{min} = I_N\, (L_{signal} + L_{comp} + L_{input} + L_{lead})\, A_{Sample} / \mathrm{m_{SQ\text{-}sample}} \qquad \text{Equation 22}$$

For samples smaller than the detection coil ($A_{Sample} < ¼\ A_{SQUID\ loop}$), the size of the sample being does not affect the sensitivity calculations. Further analysis will show that maximum sensitivity occurs when the coil (or SQUID loop) diameter ≈ 1.7x the coil-to-sample (lift-off) distance. Thus—if field sensitivity is important (to achieve a reasonable signal-to-noise)—reducing coil

diameter to less than 60% of the dewar gap will not be of great benefit and may actually result in a less desirable (or more expensive) instrument.

9.3 Magnetic Microscopes

Since electrical currents create magnetic fields (Figure 43a), the ability to measure small magnetic fields offers the potential to locate the causes of semiconductor failures.

In failed integrated circuits (IC), a short circuits would appear as a small area of intense magnetic flux. By overlaying a magnetic map (created by scanning a SQUID sensor over an IC) onto a CAD map of an IC's features (Figure 51), it is possible to locate where faults occur in a device. Knowledge of where faults are can allow determination why the fault occurred.

SQUID magnetometers have been used to make non-contact measurements of electronic circuits [104]—one instrument has better than 10 μm resolution [105]. Such instruments with MHz bandwidths could be used for circuit board and IC mapping. Reference [106] gives an excellent overview of SQUID NDE research. Using commercially available HTS SQUID microscopes, it is possible to detect 10 nA currents flowing in a conductor that is 100 μm from the sensor.

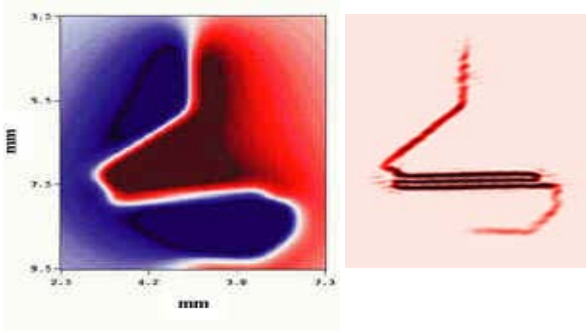

Figure 51 Magnetic field map generated by current flow and its deconvolved current map. Courtesy of Neocera.

Key to deciding on the type of instrument to be used is the required sensitivity and spatial resolution. Since these tend to be mutually exclusive for a given device, the user needs to decide what requirements are most critical. For example, micron resolution is meaningless if there is not sufficient sensitivity to detect the features being scanned.

The figures of merit used to assess these devices include:

- The spacing between magnetic features

  This is a key concern. A single dipole can be localized ten times better than resolving two closely spaced dipoles. The smaller **and** closer the detection coil, the better.

- How close you can get to the magnetic feature

  Getting closer will improve signal-to-noise, but getting much closer than a detection coil diameter gives no significant improvement in spatial resolution, especially for multiple sources. In essence, the detectable feature size is—to first order—a product of coil area and standoff distance.

Desired spatial resolution can also affect scan time. A 100 x 100 point scan can take nearly 3 hours to complete if the magnetometer acquires data for 1 second at each data point. Shorter acquisition times can speed up scan time, but at the expense of field sensitivity (since SQUID noise is proportional to the square root of the measurement time).

Let us consider scanning magnetic microscopes based on differing technologies:

1) Conventional LTS SQUID scanner
2) Scanning LTS SQUID Microscope
3) Conventional HTS SQUID scanner
4) HTS SQUID microscope

9.3.1 LTS SQUID Scanning System

This system uses a niobium liquid helium (LTS) SQUID sensor and a separately wound detection coil (or coils). It requires the detection coil to be either immersed in liquid helium or in vacuum, but thermally anchored to a 4.2 K bath. Conventional coils can be wound with less than 2 mm diameter. Combined with a 2 mm stand-off, spatial resolutions (for a single dipole) < 250 μm are possible. The ability to use a three-dimensional structure for the detection circuit allows significant external noise rejection. Another advantage of niobium–based superconductors is the ability of the detection coils to operate in tesla fields. This gives the LTS microscope the ability to make susceptibility measurements on the same spatial resolution scale. In addition, these systems can operate in multi-gauss ac fields with dc - 50 kHz bandwidths for eddy current measurements. The LTS SQUID scanner has the best field sensitivity (< 10 fT/√Hz) of any magnetic field microscope. Versions of the LTS SQUID scanner have been available for more than 20 years [104].

A variation on traditional LTS scanner is the use of sub-mm diameter coils or fractional turn SQUIDs combined with mm or smaller lift-off distances [49]. In this ultra high resolution scanning SQUID microscope, the detection coil was a 500 μm-diameter NbTi pickup coil wound on a sapphire bobbin. The coil is located in the vacuum space of the cryostat separated by a 25-μm-thick sapphire window from the room-temperature samples, with a distance of ~250 μm between the coil and sample. Thermal anchoring of the sapphire bobbin to the helium bath kept the detection coil well below the transition temperature of NbTi. External noise required full sensitivity (< 100 fT/√Hz) measurements to be done in a magnetic shield. Alternate versions of this scanner could use smaller diameter bobbins, monolithic or fractional turn SQUIDs for higher spatial resolution.

9.3.2 LTS Scanning Magnetic Microscope (SMM)

This system [107] uses a monolithic array of SQUID sensors and LTS coils. Up to nine (linear array) 14 μm x 14 μm coils are at the end of a cantilever that is suspended over the sample. The sample is cooled to allow the detection coils to be within a few μm of the sample, yielding 2 μm spatial resolution. While that accuracy not be sufficient to locate a specific submicron transistor, it can place defects in a particular region so other tests can be performed. The use of superconducting stepper motors allow 0.16 μm X-Y resolution on the scanning stage. Since the sample and coils are cooled, superconducting shielding can be used to eliminate all external noise sources. Sample loading requires the cryostat to be warmed up, but the use of load-locks may allow SEM style sample handling. It is

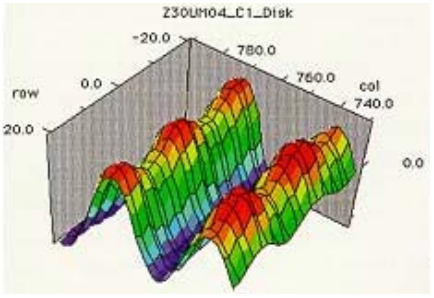

Figure 52: Magnetic image of data on a hard disk. Measurements were made at a vertical standoff of 30 μm. The bit spacing is 10 μm and the inter-track spacing is 15 μm (courtesy UCSD).

also possible to add field generation coils to apply small dc and ac fields for susceptibility and eddy current measurements.

The LTS Scanning Magnetic Microscope has a field sensitivity < 100 x 10^{-12} T/√Hz. A relatively mature technology, it has a low risk factor in terms of technology development. One such system [107] has been operating for over ten years.

9.3.3 HTS SQUID Scanning System

The high temperature (HTS) version of the LTS Scanner (§9.3.1), this uses a YBCO HTS SQUID sensor. The inherent anisotropic nature of the HTS superconductors require that the planar detection coil be integral or inductively coupled to the sensor, unlike the LTS scanner that can use 3-dimensional gradiometer coils for improved noise rejection. Commercially available HTS sensors have typically consisted of a single turn coil with a 8 mm hole with sensitivities as low as 20 x 10^{-15} T/√Hz.

If operated outside a shielded room, environmental noise may exceed the available dynamic range of the higher sensitivity magnetometers. Decreasing the HTS coil size (which can improve spatial resolution—see Figure 54) to decrease sensitivity may allow unshielded operation. The fixed dynamic range and decreased input sensitivity translates to a higher maximum input signal. Unshielded operation can also be achieved by using a planar (*e.g.*, dB_z/dx) gradiometer. The typical 500:1 balance attenuates the rfi and powerline interference sufficiently for the flux-locked loop to hold lock. A typical sensitivity for a 10 mm baseline planar gradiometer is 50 x 10^{-15} T/cm√Hz. Obviously, the system output will reflect that of a planar gradiometer rather than that of a magnetometer.

Unlike LTS SQUIDS, HTS SQUIDs do not have the ability to operate in tesla fields. It is possible to operate a HTS scanning system in millitesla fields. HTS systems have been operated in milligauss ac fields with dc – 20 kHz bandwidths. This makes them the preferred (HTS) device for susceptibility and eddy current measurements on macroscopic samples. Typically, sensor-to-sample distances are < 1 cm, although dewars can be made with 2 mm standoff distances.

9.3.4 HTS Scanning SQUID Microscope (SSM)

Conceptually identical to the LTS Scanning Magnetic Microscope (§9.3.2), the SSM typically uses the bare SQUID loop (~50 μm) as the detection coil. Operating in the dewar vacuum space (but thermally anchored to the liquid nitrogen bath or closed cycle refrigerator) stand-off distances <100 μm are possible [47]. The SSM (because of its smaller detection "coil") has a sensitivity ~ 10^{-11} T/√Hz. SSM's normally achieve close spacing by either fixing the SQUID sensor to the bottom of the dewar or having a mechanism that allows for external adjustment of the coil position to compensate for thermal contraction [108].

Unfortunately, its magnetometer detection coil configuration may make it susceptible to external noise sources (depending on the local environment). Operation in a shielded environment can improve noise immunity. By using phase sensitive detection (injecting an ac current into the device under test), background noise can be filtered out. The addition of external field coils can make susceptibility measurements (dc or ac) possible.

The use of a ferromagnetic flux transporter [109] can offer significant improvement in spatial resolution in HTS microscopes, but at a loss in ac response.

One use for a SSM is measurement of current traces. By overlaying SSM images on a CAD map of an IC or circuit board features, it is possible to locate where actual faults occur. Under ideal conditions, a SQUID can detect as little as 10 nA flowing in a conductor that is 100 μm from the sensor. Other uses are in magnetoimmunoassay (§9.6), paleoarcheology (§8.3) and detection of counterfeit currency (Figure 53).

Figure 53 SSM scan of the ink in the region around George Washington's right eye on a one dollar bill.

9.4 Sample Movement and Scan time

To avoid motion induced noise (caused by moving the SQUID sensor in the Earth's magnetic field); the sample is moved underneath the SQUID sensor. The typical measurement sequence in SQUID microscopy is serpentine step and measure. After each movement, there is a short (usually user specified) settling time after which the measurement is made (again for a user specified interval) after which the sample is moved to the next measurement position. Total scan time is a product of the number of measurements and the distance between each step, the speed of the sample translation stage, the wait) time and the measurement time at each step.

Assuming 1 second between measurements, a scan of a 1 cm^2 area with a 100 μm step size will take nearly 3 hours. Obviously, shortening the measurement time (*e.g.*, by continuously measuring with moving the sample) will reduce the scan time, but with the penalty of increased noise ($B_{noise} \propto \sqrt{}$measurement time). In many situations, sample variations will be significantly higher than system noise. It may be worthwhile to prescan the sample with a short measurement time and a step size significantly greater that the desired spatial resolution to identify which parts of the sample will require higher resolution scans. Subsequent scans can be done in selected regions with the much smaller step sizes; this avoids excessively long measurement times.

9.5 Microscope Selection

Environmental noise can have a significant effect on microscope operation. Many HTS microscopes operate unshielded because of their significantly reduced sensitivity compared to LTS microscopes. Even so, care must be taken to ensure that the microscope is not placed in an environment where external noise sources dominate to the point of preventing the SQUIDs from being able to operate. One way to avoid this is to enclose the microscope in a magnetic shield. Alternatively, use of gradiometers can allow unshielded operation. This is especially true for LTS devices. For HTS devices where high (sub-mm) spatial resolution is not as important as field sensitivity, planar gradiometers offer a way to operate unshielded and avoid the complexity of a shielded enclosure.

The choice of which microscope system depends on the needed spatial resolution and magnetic field sensitivity. Resolution (the minimum separation between two magnetic features) is dependent on both the distance from the sensor to the sample (liftoff) and detection coil size. If a

SQUID microscope can place its sensor very close to the sample (< 2 coil diameters), then the coil size is the limiting factor to resolution.

Because the flux sensitivity of SQUID sensors is roughly constant (for a given type of SQUID sensor), there is an inverse relationship between sensitivity and spatial resolution. Figure 54 shows the trade off between sensitivity and spatial resolution for a number of different SQUID sensors.

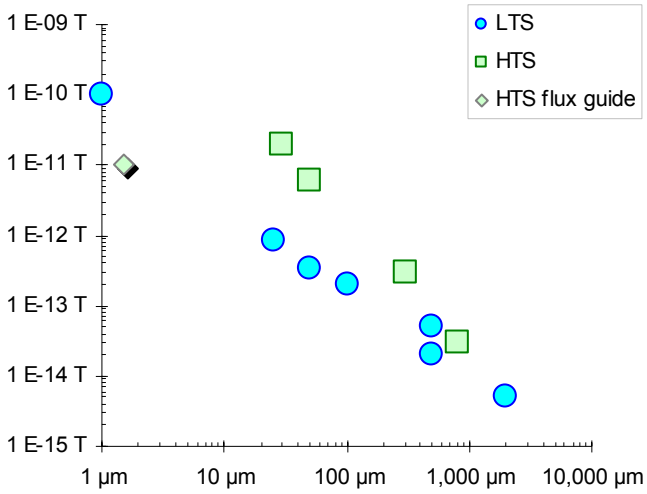

Figure 54 Sensitivity (tesla/√Hz) and Spatial Resolution of a number of SQUID microscopes

9.6 Magnetic Assays (Immunoassays)

Similar to tagging molecules with radioactive isotopes (radioimmunoassay), fluorescent molecules, light scattering particles, and enzymes for the production of chemiluminescent signals, magnetic particles tens of nm in size can be used to tag molecules to investigate biological and chemical reactions. These tagged particles can be localized after paper chromatography or other such separation process by measuring their remnant magnetic field(s). SQUID based magnetic microscopes are well suited to this task. Subjecting the magnetic nanoparticles to an external magnetic field and (after switching off the field), measuring the relaxation of the magnetization can give information about the nanoparticles by differentiating between the differing relaxation times due to the movement of entire particles (Brownian motion ~ 10^{-5} sec for a 20 nm particle) and rotation of the magnetization vector inside the particle (Néel relaxation: 0.01 – 10 sec). This use of magnetorelaxometry can allow identification of bound and unbound molecules by discriminating between the different relaxation mechanisms. Reference [110] describes a LTS system utilizing a planar gradiometer for magnetorelaxometry measurements.

Figure 55 shows one method of magnetoimmunoassay. An antibody is attached to a marker that is tagged with magnetic particles (*e.g.*, γ-Fe_2O_3) embedded in a polymer core. For the detection of an antigen, an antibody that selectively couples to the antigen is used. Figure 55 illustrates a capture surface with an immobilized capture molecule for one domain (epitope) of the target and a free label conjugated to another detection molecule, specific for another epitope of the target.

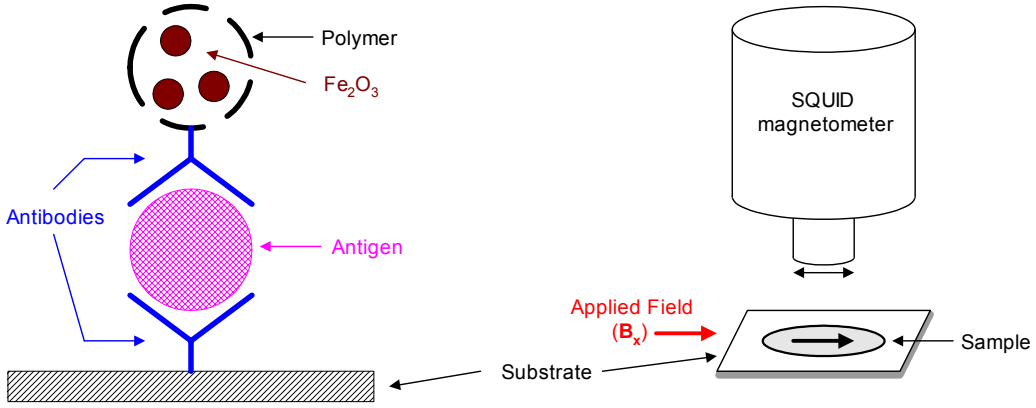

Figure 55: a) binding reaction between antibody and antigen in magnetoimmunoassay, b) schematic diagram of magnetoimmunoassay measurement

In the presence of the target, the label is attached to the capture surface and in the absence of the target, the unbound label can be washed away. Detection occurs after measuring the presence (or absence) of the label on the capture surface.

Issues that affect signal-to-noise are things like non-specific binding (NSB) and interfering signals from other sample materials. The magnetic detection approach suffers from very little outside interference, unlike many of the other non-radioactive (optical) methods. The approach of magnetorelaxation is a unique means to address the issue of non-specific binding and washing. The idea is that specifically bound labels will not be free to undergo Brownian rotations as will the free and non-specifically bound labels. So if the label is designed so that its Néel relaxation time is long compared with its Brownian relaxation time, then the relaxation measurements can potentially distinguish specifically bound labels, even with no washing. Approaches which do not rely on a wash step to separate specifically from non-specifically bound labels are called “homogenous”.

10 MEDICAL APPLICATIONS OF SQUIDS

Electrical measurements of physiological potentials are well established in clinical diagnostics. Essentially every phenomenon in electrophysiology has a magnetic analog since a magnetic field is associated with every electric current. Analogous measurements of physiological magnetic fields, however, are relatively unknown to researchers and clinicians. Biomagnetic research encompasses many of the major organs of the body, including the heart, brain, liver, lungs and muscles. Several new diagnostic procedures and instruments have resulted from this work. These measurements are proving to be of considerable significance [*c.f.*, see proceedings of the various international biomagnetism conferences such as [43]).

As shown in Figure 57, biomagnetic signals range from essentially dc to several hundred Hertz, and the field intensities range from about 50 fT to 10^6 fT. The sources of these fields vary from localized groups of neurons in the brain, to more dispersed muscle tissues in the heart, to magnetic particles distributed throughout the lungs.

There are two key technical advantages to employing magnetic—as opposed to electrical—sensors for measuring biological ion currents:

1) The generators of electrical activity in the body can be precisely localized to within a few millimeters from their magnetic signals, because magnetic signals are not strongly dependent upon variations in the body's tissue conductivity as are electrical signals. Furthermore, the body's tissue is effectively transparent to magnetic fields in the biological frequency range.
2) Measurement of dc and low-frequency phenomena is feasible because of the inherent dc response and low noise of SQUID magnetometers, and because there is no artifact due to changing electrical contact with the body, as is the case when measuring biological potentials with electrodes.

The use of bioelectric signals as a diagnostic tool is well known in medicine, *e.g.*, the electrocardiogram (EKG) for the heart and the electroencephalogram (EEG) for the brain [55].

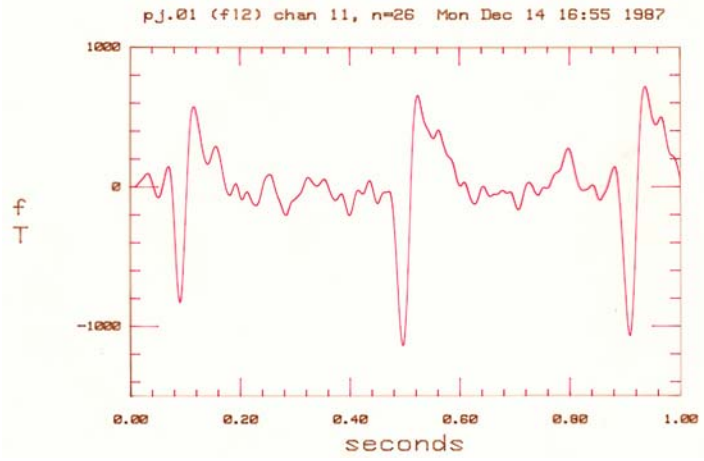

Figure 56 magnetocardiogram of fetus (29 week gestation)

The electrical activity that produces the surface electrical activity that is measured by EEG and EKG also produce magnetic fields. The analogous magnetic measurements are known as the

magnetocardiogram (MCG) and the magnetoencephalogram (MEG) (Figure 57). Other physiological processes also generate electrical activity with analogous magnetic fields.

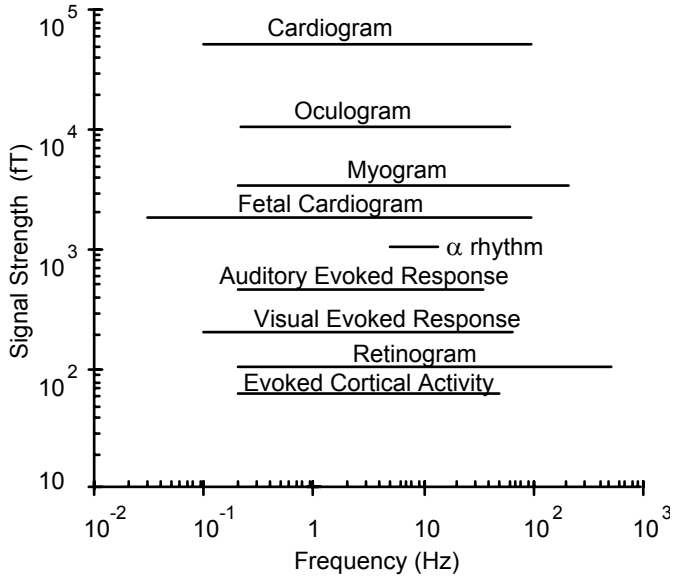

Figure 57 Typical amplitudes and frequency ranges for various biomagnetic signals (based on a ~1 cm tail gap). add spinal cord 5 Hz – 30 Hz at 15 fT and squid axon 1 Hz – 1 kHz at 100 pT, neonate δ rhythm 10 pT at 1.5 – 4 Hz

The development of the SQUID has allowed the development of non-invasive clinical measurements of biomagnetic fields (Table 4). The use of gradiometers can allow measurements to be made in unshielded environments at sensitivities below 20 fT/√Hz. However, neuromagnetic measurements are typically made in room-sized MSR's [111] that will allow measurements of the magnetic field of the brain over the entire surface of the head (>250 positions simultaneously).

Table 4 areas in which SQUID magnetometers are being used in medical research

Studies of the Brain—Neuromagnetism
- Epilepsy
- Presurgical Cortical Function Mapping
- Drug Development and Testing
- Stroke
- Alzheimer's
- Neuromuscular Disorders
- Prenatal and neonatal Brain Disorders
- Performance Evaluation

Studies of the Heart—Magnetocardiography
- Arrhythmia
- Heart Muscle Damage
- Fetal Cardiography

Other Medical Applications
- Non-invasive *in-vivo* Magnetic Liver Biopsies (Ferritometry)
- Studies of the Stomach—Gastroenterology
- Intestinal and Mesenteric Ischemia
- Lung Function and Clearance Studies
- Peripheral and Single Nerve Studies
- Organ Transplant Rejection Risk
- Blood Flow Disorders

Animal Systems
- Drug development

10.1 Measurement Techniques

Magnetic fields associated with different physiological functions and conditions vary widely in their intensities, frequencies and spatial distributions (Figure 57). Consequently different techniques and instruments must be used in their measurement.

Magnetic fields from active electrical sources in the body are measured completely passively and external to the body by placing the detector in close proximity to the body's surface. This technique is applicable to the heart, brain and skeletal muscles. It has been shown in the case of the brain, for example, that a neuron can be modeled as a current dipole [112] which generates a well defined magnetic field profile (Figure 58). Measurement of this profile can be used to infer the location of the neuron with considerable accuracy. Using evoked response techniques, the location of signal pathways and information processing centers in the brain can be mapped at different delay times (latencies) following the stimulus. For this purpose, the field is mapped around the surface of the head (Figure 60).

Systems for measurement of the brain require that the head be surrounded by detection coils. Unlike whole head measurement systems, most other biomagnetometers utilize flat tail dewars. The channel count and coil arrangement are dependant on the application. If measurements are being made in a MSR, typically the detection coils are 1st derivative gradiometers. Measurements in unshielded environments require 2nd order gradiometers with a high balance (~1:10^6) or in conjunction with reference channels. Unshielded operation also requires careful attention be paid to rfi immunity.

Systems for susceptibility measurements use magnets, either integral to the detection coils (*c.f.*, §10.7) or immediately prior to the measurement (*c.f.*, §10.8). Care must be taken not to couple field generated noise into the detection coil(s).

10.1.1 Magnetic Mapping

Magnetic fields from active electrical sources in the body can be measured passively and external to the body by placing the magnetometer in close proximity to the body's surface. It has been shown that a population of neurons in the brain can be modeled as a current dipole that generates a well-defined magnetic field profile (Figure 58). Reference [113] gives an excellent review of magnetic source imaging.

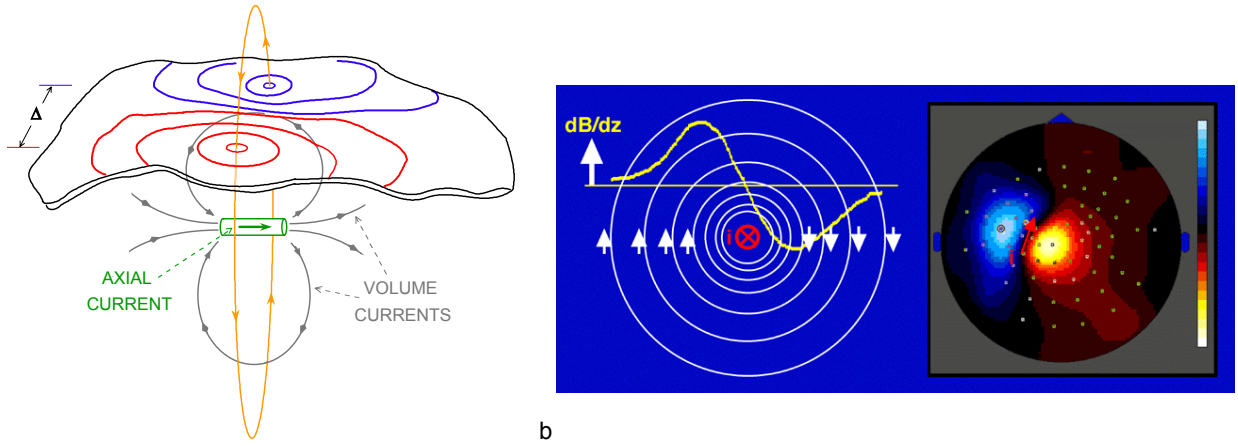

a b

Figure 58 Magnetic field generated by a current dipole. For a sphere, the dipole is located at midpoint of the maxima and minima at a depth = distance Δ ÷ √2. Figure 58b courtesy of CTF.

To generate a contour map, measurements are taken at a number of points (upper left of Figure 59) and the magnetic field values are determined at a given point in time at each grid point (upper right of Figure 59). Isofield contours are then generated to yield a field map (lower left of Figure 59). Time sequenced contour maps can be generated by looking at subsequent time slices

(lower right of Figure 59). The distance between measurements (equivalent to the inter-coil spacing on multi-channel systems) is dependant on the depth of the source and the spatial resolution desired.

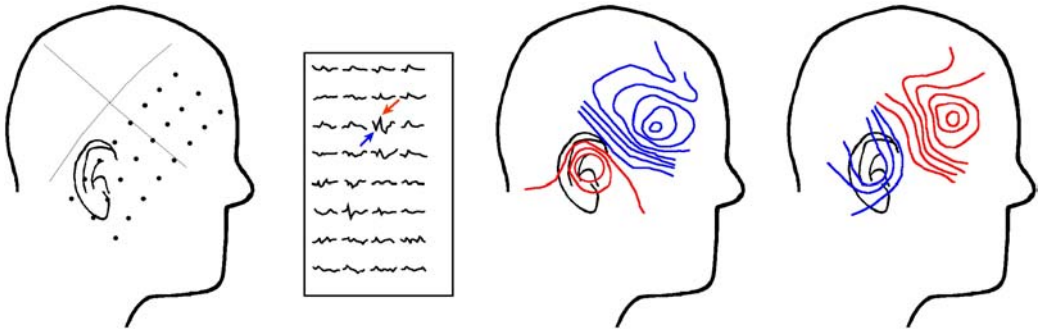

Figure 59 Field contour map generation. Data courtesy of W. Sutherling, 1983.

Mapping of these field profiles can be used to infer the location of the equivalent active dipole site region to within millimeters. Using evoked response techniques, the location of signal pathways and information processing centers in the brain can be mapped at different delay times (latencies) following the stimulus (Figure 60).

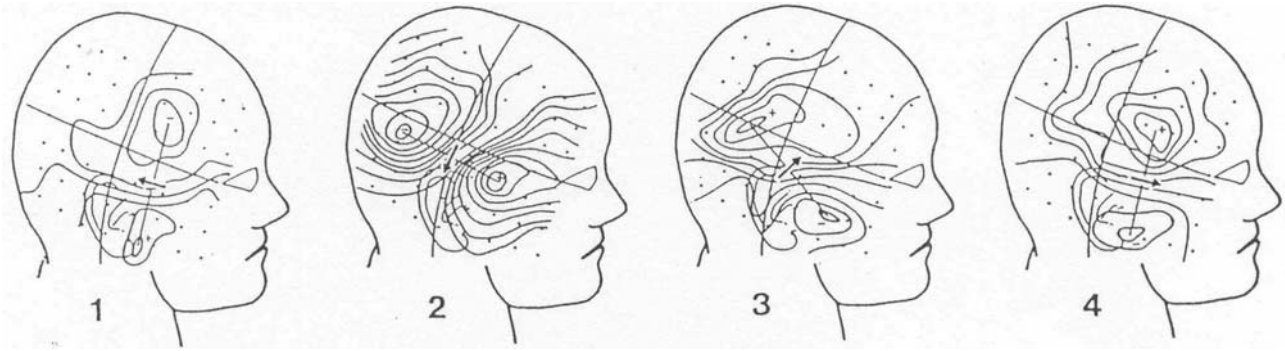

Figure 60 Neuromagnetic patterns generated by the interictal spike complex in a patient with a partial epileptic seizure disorder. The individual patterns are measured at intervals of approximately 20 msec. Data courtesy of W. Sutherling, 1983.

There are also magnetic measurements for which there are no electrical analogs [114]. These are measurements of static magnetic fields produced by ferromagnetic materials ingested into the body and measurements of the magnetic susceptibility of materials in the body. In particular, information on the quantity and depth of diamagnetic or paramagnetic materials (such as iron stored in the liver) can be obtained by using magnetizing and detection coils of differing sizes in the same instrument and measuring the induced field as a function of distance. This technique is being used to clinically monitor patients suffering from iron overload diseases such as hemochromatosis, thalassemia and sickle cell anemia.

10.1.2 Magnetic Source Measurements

Para/Diamagnetic Sources. Fields from paramagnetic or diamagnetic materials are measured while a low intensity external magnetic field is applied to a local region of the body and compared with the background field when the subject is removed from the sensitive range of the instrument. Information on the depth of these materials can be obtained by using magnetization

and detection coils of differing sizes in the same instrument or by measuring the field as a function of distance from the body.

Ferromagnetic Sources. The location and quantity of ferromagnetic materials in the body, typically due to contaminants in the lungs (Magnetopneumography-§10.8), are determined by measuring the magnetic field external to the body before and after a low intensity magnetic field (typically 0.1 Tesla) is applied to magnetize the ferromagnetic material. the distribution of these materials can be determined by applying the field to only a small region of the body at a time.

10.2 Sensitivity

As mentioned, the choice of detection coil design is very much dependent on what is to be measured. Although many systems for biomagnetic measurements are described in terms of their ability to detect magnetic fields—a valid assumption when considering noise sources—or magnetic dipole sources, the magnetic dipole does not provide a good model of neurological sources. The most common source model in electrophysiology is that of the current dipole (Figure 58). The strength Q of a current dipole has the dimension of current times length and the unit of ampere-meter. It is represented by a vector whose direction coincides with the direction of the current. The current dipole is a simplified representation for much more complex patterns of current which exist at the cellular level [112]. The current dipole is useful in that more elaborate extended sources can be represented by an array of individual current dipoles. The response of a simple magnetometer to a current dipole in free space can be expressed by [37]

$$Q_{\min} = \frac{\pi \, \Phi_{\min} \sqrt{m}}{\mu_o \sqrt{\frac{r}{\rho}} \left\{ \left[1 - \frac{m}{2} \right] K(m) - E(m) \right\}} \qquad \text{Equation 23}$$

where $m = 4r\rho/\sqrt{[(r + \rho)^2 + z^2)]}$ and $Q_{\min}$ is the smallest current dipole that can be detected, Φ_{MIN} is the minimum detectable magnetic flux in the pickup coil (see eq. 3), μ_o is the permittivity of free space (= $4\pi \times 10^{-7}$ henries/meter), r is the radius of the pick-up coil, ρ is the off-axis distance (in cylindrical coordinates), z is the axial distance of the current dipole below the bottom of the pick-up coil and K and E are elliptical integrals of the first and second kind. For a gradiometer, one must sum the response of all the coil windings and take into account the baseline of the gradiometer. The tail spacing of the dewar must not be neglected when determining z. Figure 61 shows minimum detectable current dipole as a function of coil-to-dipole distance. Unlike the response of a magnetic dipole which goes as $1/z^3$, the response of a current dipole goes as $1/z^2$.

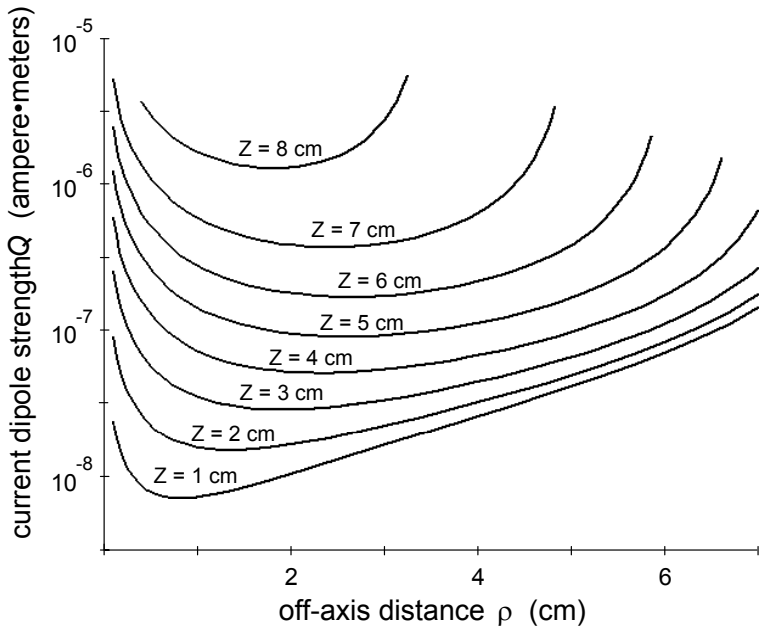

Figure 61 Minimum detectable current dipole for a 1st derivative, six turn, 5 fT/√Hz gradiometer with a coil diameter of 2 cm as a function of off-axis position (ρ) and depth (z) [115].

As can be seen, the sensitivity for a current dipole goes as $1/r^2$, rather than the $1/r^3$ expected for a magnetic dipole. Also, the maximum sensitivity is not located directly beneath the detection coils, but offset (consistent with Figure 58).

10.3 Magnetoencephalography – Measurements of the Brain

The magnetoencephalogram (MEG) is the magnetic counterpart of the more familiar electroencephalogram (EEG). The amplitude of the MEG signals is quite small, amounting to approximately 1000 fT peak-to-peak over the back of the head. Spontaneous brain activity is readily observed using SQUID magnetometers, without resorting to signal averaging. By making MEG measurements from an array of magnetic sensors, it has been demonstrated that sources of brain activity can be localized to within a few millimeters. By contrast, it is sometimes difficult to localize brain activity to the correct hemisphere when using EEG.

Since magnetoencephalography can be used to associate brain function with the underlying anatomic structure, it may eventually be beneficial in the diagnosis of neurological disorders such as epilepsy, Parkinson's disease, Alzheimer's disease, stroke, and head trauma. The overall anatomic distribution (pattern) of brain activity may also be useful in providing objective measurements relating to psychiatric disorders and their treatment with psychoactive drugs.

The ability of MEG to localize brain activity has prompted clinical research studies of epilepsy [116]. When neurosurgery is indicated in the treatment of epilepsy, the surgeon requires information as to the location and extent of the brain tissue generating the seizures, as well is detailed information of where various brain functions are mapped (the latter to guide where *not* to cut!). Presently, the clinically acceptable method for obtaining this information is by implanting electrodes on or within the patient's brain. Preliminary findings have shown that localization of epileptic centers by MEG is in close agreement with findings using invasive electrodes. Pre-surgical functional mapping is another example were MEG has been used to

delineate where various brain functions are mapped. Intensive testing will be required to determine if MEG is reliable enough to stand alone as a guide to the neurosurgeon. Because of its non-invasive nature, MEG promises to reduce both risk and cost to the patient in the pre-surgical diagnosis of epilepsy.

The first MEG measurements were made with single channel magnetometers. This required multiple placements over the subjects head (Figure 59) and often took days to complete. Present day MEG systems provide whole head coverage that require hundreds of sensor channels. This allows real-time acquisition of data.

Noise reduction is achieved through the use of MSRs and 8-element tensor reference arrays. The first multi-channel (N = 5 - 7) neuromagnetometers used fixed superconducting tabs to improve gradiometer balance from $1{:}10^2$ to $1{:}10^4$. Because of the labor associated with placing superconducting tabs on hundreds of channels, their use on high channel count systems has been abandoned. Instead, MSRs are used to provide shielding of external noise. Typically, the detection coils of MEG systems are first order gradiometers, either hand-wound axial (dB_z/dz) or planar (paired dB_x/dz and dB_y/dz). The advantage of planar coils is their intrinsic balance is superior to hand-wound axial coils. The disadvantage of planar coils is their baseline is much shorter than axial coils; this gives axial coils an advantage when measuring deep sources. While pure magnetometers have been used (to maximize sensitivity), their inability to reject common mode noise makes them much more susceptible to low frequency noise in drift (*e.g.*, elf (< 10 Hz) signals generated by high speed rail lines). The MSR (Figure 30) gives 30 - 80 dB of attenuation and the reference arrays another 60+ dB.

Another advantage of the high channel count of whole head systems is the ability to use the array of sensors to image the MEG signals using methods analogous to those applied to radio astronomy. One such method, synthetic aperture magnetometry (SAM) is a constrained minimum-variance beamformer [117]. SAM minimizes all signals seen by the sensor array, subject to a constraint for an equivalent current dipole at a specified coordinate. As a result, this beamformer has a gain of unity for signals arising from the specified location, while attenuating all other signals. Thus, SAM can be thought of as "spatially-selective noise reduction". This property permits functional imaging of brain activity without requiring signal averaging, and without the need to delete artifacts from eye movement, heart signal (MCG), or environmental magnetic noise.

The large surface area (hundreds of cm^2) and complex shape of a whole-head dewar (Figure 62) usually means thick tail pieces and dewar gaps > 20 mm. Putting the dewar cavity at an angle to allow the dewar to be positioned for either seated or supine (lying down) patents increases the design and fabrication complexity. Dewar motion for whole head systems is usually only in the tilt (θ) direction. The patient is located by movement of a 3-axis (x, y, z) bed and/or chair.

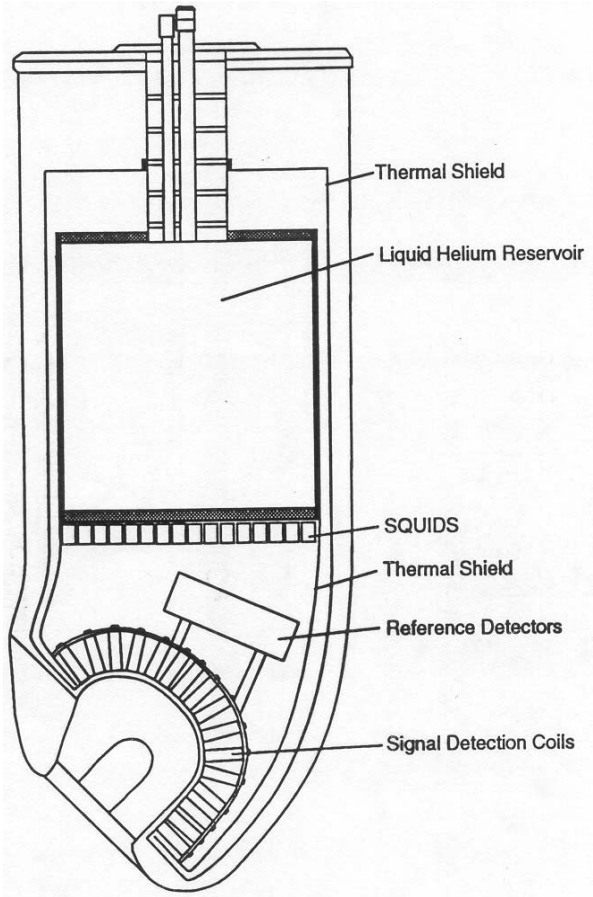

Figure 62 whole-head neuromagnetometer (coil-in-vacuum construction), courtesy W. Black, BTi.

If infants are to be measured, significantly closer spacing can give significant improvement in signal to noise. It should be noted that the scalp and skull of newborns are thin. This make it possible to measure MEG signals at a distance less than 1 cm from the brain surface [118]. This shorter distance will result in a large increase in the amplitude of MEG signals from the infant, since the magnetic field is inversely proportional to the square of the distance (*c.f.*, §10.2). The shorter distance and a high density of detectors can also result in higher spatial resolution.

Ancillary equipment (*e.g.*, patient bed, dewar gantry, etc.) need to have no time varying magnetic signature. Ferromagnetic components are to be avoided because of their relatively large (μT or mT) remnant fields. Non-ferrous metallic components (which can cause scattering of gradient interference) may be acceptable if sufficiently far from the detection coils [119].

10.4 Magnetocardiography– Measurements of the Heart

The magnetocardiography (MCG) is the magnetic signal generated by the heart's electrical activity. The MCG is homologous to the electrocardiogram (ECG). A peak MCG signal of 50 pT can be measured over the heart. This signal is easily measured by SQUID magnetometer, with excellent signal-to-noise ratio.

Measurement of the heart's conduction system is important in the diagnosis of diseases in which the heart has an abnormal rhythm, reduced mechanical performance, and higher susceptibility to sudden failure. Direct current (dc) MCG measurements have shown that a "current of injury" flows in the heart as a result of myocardial infarction. Although a current of injury signal can

also be seen in the ac-coupled electrocardiogram, the magnitude of the injury and the location of the injured region cannot be determined with precision. Using MCG, it may be possible to determine both the location and extent of the injured heart tissue. Clinical studies are underway to test this hypothesis [120].

The SQUID magnetometer is sensitive enough to non-invasively detect the fetal magnetocardiogram (Figure 56). The fetal electrocardiogram is often used by physicians as a measure of fetal distress, but detection of this fetal heart beat is often unreliable. This is because, later in gestation, the fetus is coated with a oily substance called the vernix caseosa. The vernix tends to electrically insulate the fetus, greatly attenuating the fetal ECG. By contrast, the fetal MCG is not attenuated by the vernix, making it possible to monitor the fetal heart through all phases of gestation, including labor. Another advantage of magnetic (as compared to electrical) methods is that the spatial resolution of MCG allows it to better isolate the fetal heart in the presence of the maternal heartbeat.

MCG has also been used to measure the specialized conduction system of the heart. To obtain electrical measurements, it is necessary for the patient to swallow an electrode, which is passed down the esophagus to the level of the heart. Measurement of the heart's conduction system is important in the diagnosis of diseases in which the heart has an abnormal rhythm, reduced mechanical performance, and higher susceptibility to sudden failure.

Cardiac measurements need only a single channel if just the time series MCG (Figure 56) is of interest. If real time dipole mapping is desired, additional channels (either in a hexagonal, square or other arrangement) to more than cover the extrema of the field patterns (Figure 58b) will be required. Figure 63 shows a 19 channel axial gradiometer system with sufficient coverage for single placement measurements.

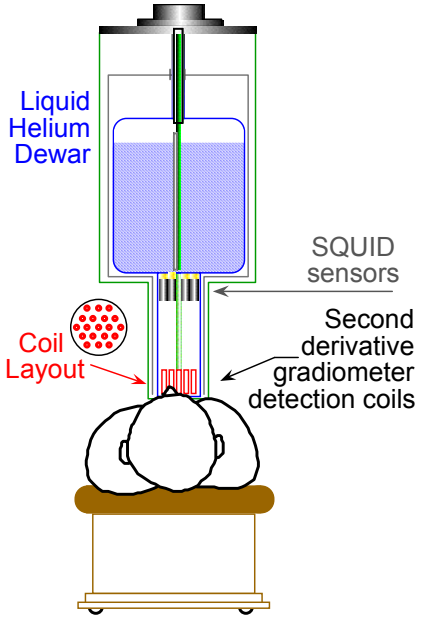

Figure 63 MCG biomagnetometer components (gantry and electronics not shown)

Typically, MCG systems measure only the vertical (B_z) field component. Dewar tails are normally flat with ~10 mm gaps. The use of a 2nd order gradiometer is preferred over a 1st order gradiometer in fetal MCG because of its superior rejection of the maternal MCG.

10.5 Magnetomyography and Magnetoneurography – Muscle and Peripheral Nerve Measurements

The electrical activity of muscles and peripheral nerves can readily be detected using magnetic sensors [121]. Here the chief advantage of biomagnetometry is its contactless non-invasive nature. In order to make equivalent electrical measurements, it is necessary to pass needle electrodes through the skin into the vicinity of the nerve or muscle.

Measurement systems for spinal cord or peripheral nerve activities are defined by the temporal characteristics and quasi-one dimensional geometry of the signal. Neurological events are typically on a 10 msec time scale while spinal cord and peripheral nerve events are typically on a 1 msec (or faster) time scale. Placement of axial coils directly over the nerve will result in a net zero signal (*c.f.*, Figure 58). Thus, vector coils (B_x and/or B_y) may be desirable. The ideal sensor placement for spinal cord measurements may be that of a long rectangular array rather than the hexagonal arrays that are used in MEG or MCG studies. Figure 64 shows the result of an electrical stimulation of the medial nerve. The measurement system consisted of 37 axial (B_z) and 13 pairs of vector (B_x and B_y) detection coils laid out in a hexagonal array.

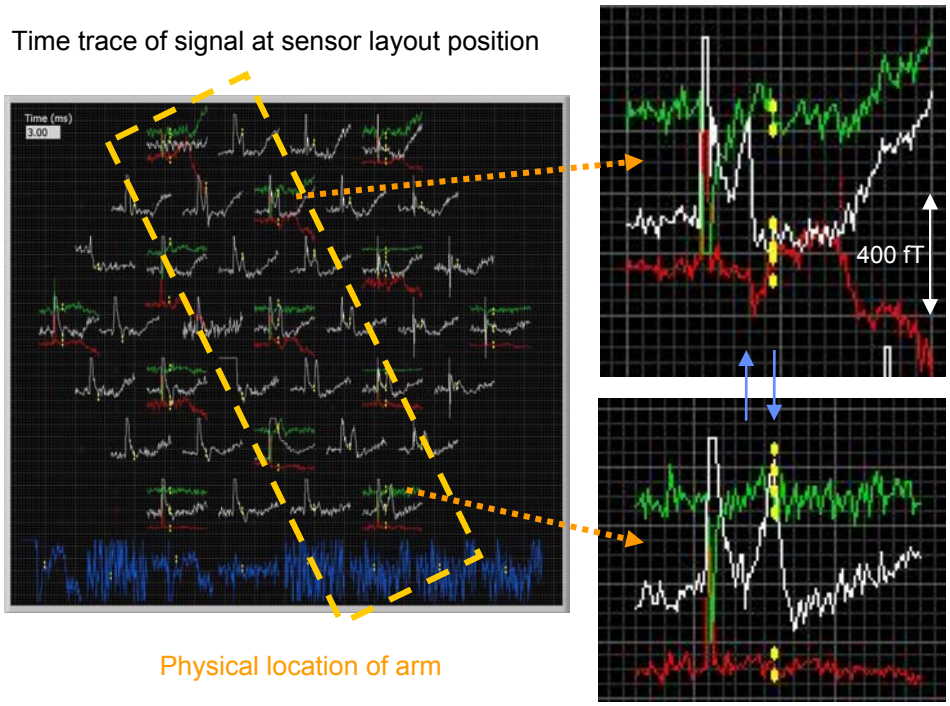

Figure 64: Peripheral nerve signals generated by an electrical shock at the medial nerve (white is B_z, green is B_x, red is B_y). The forearm location is shown by the outlined box. The first (vertical) peak is the stimulus artifact. The next peak is the detected peripheral nerve as it travels up along the forearm. The distance between the two (expanded) sensor locations is 5 cm. The peak (B_Z) of the detected signal between the upper and lower expanded time display has shifted by 2 msec.

10.6 Magnetoenterography – Measurements of the stomach and Intestines

Blockage of arterial blood flow (ischemia) in the gastrointestinal tract can lead to intestinal necrosis. Treatment requires surgical intervention to removed or bypass any necrotic intestinal tissue. If diagnosis is delayed, the mortality rate can exceed 50%. Conventional diagnosis of mesenteric artery narrowing or blockage is by an arteriogram that requires a catheter and X-ray dye. Because of the limits of X-ray resolution, arteriograms can only see blockages of blood vessels 1 mm or larger.

The gastrointestinal (GI) tract exhibits two types of electrical activity: a high frequency (in the Hz regime) spiking associated with muscle contraction and low frequency oscillations (CPM - cycles/minute) known as the Basic Electric Rhythm (BER). While the BER can be detected using electrodes, this is a highly invasive procedure. Typically, the signal strength of a BER signal is at the pT level. As shown in Figure 65, ischemic episodes show a marked reduction in the BER [122]. SQUID technology offers the possibility of detection of ischemia by monitoring the BER frequency.

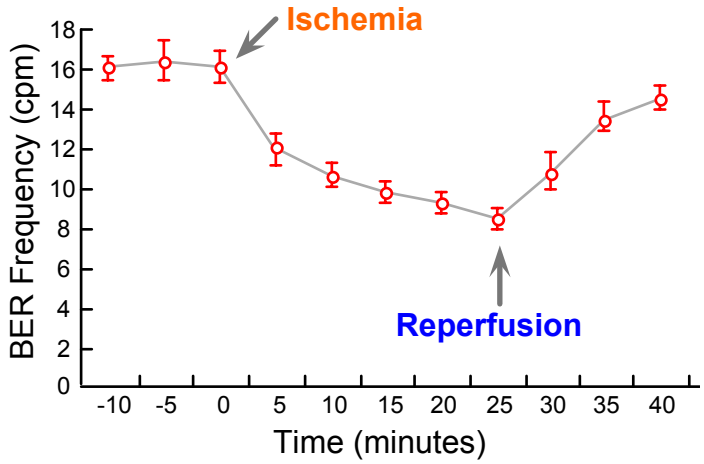

Figure 65: Shift in BER before and after chemically induced occlusion of a mesenteric (intestinal) artery. The BER frequency varies as a function of position within the GI tract. The gastric BER is typically 3.2 ± 0.1 CPM whereas the small intestine BER is 11.3 ± 0.1 CPM and the duodenum BER is ~12 CPM. . Data courtesy of W. Richards.

Instrumentation for magnetoenterography is similar to some magnetocardiography systems in channel count. Typically a low to medium (19 – 37) channel count with sensitivity better than 50 fT/√Hz is sufficient to detect and localize the BER. However, since the GI tract has a complex shape that cause the current paths to be in different directions, vector (B_x and B_y) detection coils are recommended in addition to the normal axial (B_z) detection coils found in MCG systems. Because of the very low frequency nature of the BER, significant attention must be paid to noise reduction. Highly balanced gradiometers and the use of an 8-element reference array are recommended, especially if unshielded operation is desired. Non-magnetic ancillary equipment (dewar gantry, patient bed, etc.) is also required to avoid coupling in environmental noise that could mask the very low frequency pT level BER signals.

10.7 Ferritometry – Magnetic Susceptibility Measurements

Although most body tissue is diamagnetic, organs rich in iron–notably the liver–can be strongly paramagnetic due to the iron storage compounds ferritin and hemosiderin. The magnetic

susceptibility of an organ can be determined by measuring the small changes in an applied magnetic field when the body is brought into the vicinity of the magnetometer. Diamagnetic tissue will cause a small decrease in the sensed magnetic field, while paramagnetic tissue results in a larger increase in the sensed field. The magnitude and extent to which the body perturbs the applied field is used to estimate tissue iron concentration.

Figure 66 shows a SQUID susceptibility system (referred to as a Ferritometer®) for measuring liver iron stores. The system detects the dc change in flux as a function of position beneath the magnet and detection coils [123]. The applied field is ~ 30 mT directly beneath the dewar tail, decreasing to a few mT a few cm beneath the dewar tail. The waterbag simulates the diamagnetic contribution of body tissue ($\chi_{water} \approx \chi_{tissue}$), essentially allowing the detection coils only to "see" the movement of the paramagnetic liver. The net change in the dc level of detected flux is related to the organ's iron concentration and has proven useful in evaluating the treatment of patients with iron overload disorders. Ferritometer® measurements of liver iron agree well (r ~ 0.98) with those obtained by liver biopsy—the only other quantitative measure of iron concentration.

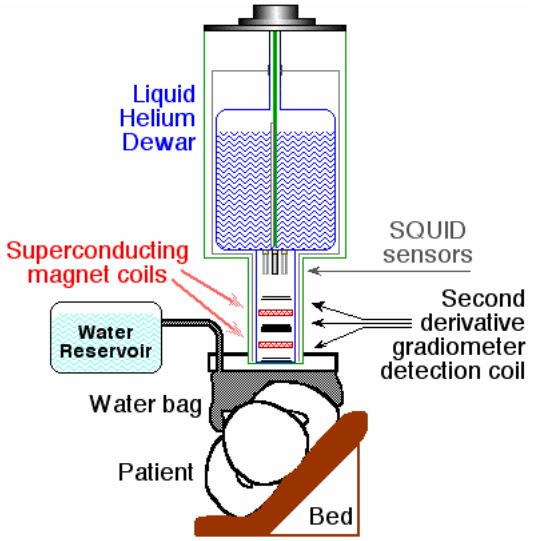

Figure 66 Ferritometer® components. Typical patient movement is 10 cm vertically. The combination of a 2nd order detection coil and a 1st order magnetizing coil gives excellent near field sensitivity while rejecting distant sources.

Ac fields have been be used to magnetize the liver [124]. In this situation, a Helmholtz coil set surrounds the patient. The advantage of the ac technique is that it can reject environmental noise better than dc methods. However, only the dc methodology (which allows significantly higher fields to be applied to the patient than ac methods, *c.f.*, §9.1) has been shown to have sufficient sensitivity and repeatability to be clinically useful.

10.8 Magnetopneumography – Magnetic Remnance Measurements of the Lung

The human body is normally diamagnetic or paramagnetic; there are no naturally occurring ferro- or ferrimagnetic constituents. Magnetic dust is the principle component of ferrous welding fume. It is also a significant part of asbestos dust, coal mine dust and coal fly ash. Ferrimagnetic materials associated with particulate contaminates such as dust in the lungs of coal miners, welders and asbestos workers can be detected by magnetizing these ferrimagnetic components.

Magnetopneumography (MPG), the measurement of magnetizable material within the lungs has been an important tool for measuring welding dust exposure in the ship building industry in Sweden and Finland. The remnant field outside the chest after exposure to a magnetizing field can be as great as 1 nT [112]. Magnetic dust is also used as a tracer for measuring lung dust clearance [125]. An inhaled dosage of one milligram is sufficient to follow clearance over one year and later. Alveolar clearance half time is about 4 month in healthy non-smokers and increases in smokers and in patients with interstitial lung diseases [126]. Recently it has been shown that particle clearance in the airways has a long-term phase [127].

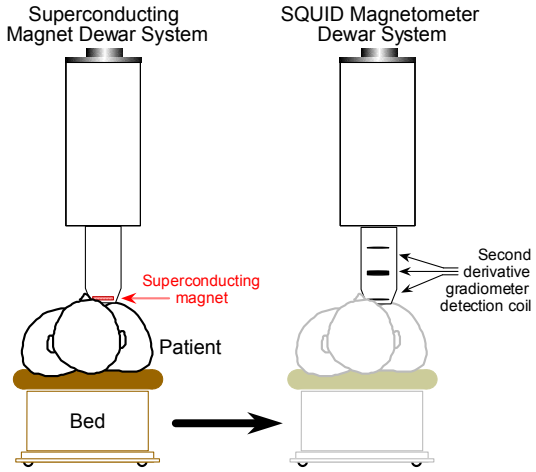

Figure 67 Magnetopneumography measurement system

The SQUID magnetometer is sensitive enough to detect particles of magnetite in the lung at levels totalling as little as 20 µg equivalent to 0.5 nanograms per cubic centimeter of lung tissue [128]. By exposing the chest to an external magnetic field of about 0.1 T, the magnetic particles become aligned and the lungs weakly magnetized. After the magnetization field is removed, the pattern of magnetization, as sensed by magnetometers, can be used to deduce the quantity and location of the magnetic particles. Exposure to a 70 mT dc field for 5 milliseconds is sufficient to achieve 90% saturation of ferrimagnetic particles.

In the lung the magnetic particles are phagocytized within hours by alveolar macrophages. Intracellular transport will cause the magnetic polarization to decay with a characteristic time constant, $M_H = m_s\left(1 - e^{-\tau/\tau_H}\right)$, where M_H is the magnetization measured by the SQUID gradiometer (Figure 67), m_s is the moment of the ferromagnetic particle and τ_H is the time constant of decay, typically a few minutes. In addition, the remnant magnetic particles can be twisted in weak (mT) magnetizing fields, which reveals viscoelastic properties of alveolar macrophages. Both relaxation and twisting are an indicator for the function of alveolar macrophages in the human lung [129].

10.9 Animal Systems

Research instruments for animal measurements have been typically low channel count systems with smaller detection coils. The higher spatial resolution desired for animal measurements (sometimes as small as 100 µm) also require closer spacing. The use of adjustable tail dewars (Figure 26) and coil-in-vacuum technology can allow moderate count (7-37) small diameter (1 – 4 mm) detection coil arrays to be built without having to use excessively thick dewar tail pieces.

The actual design of an animal system is very much dependant on the size and shape of the animal being measured. For mice and other small animals, physical constraints (and budgets) often limit the measurement system to a few channels of mm scale detection coils inside a flat tail dewar. A system for MEG measurements on a macaque monkey could be a scaled down version of an adult whole-head system (§10.3) with an equivalent cost. SQUID magnetometers can also be used for measurements of action potentials [130] and tissue slices. The technology developed for magnetic microscopy (§9.3.1) has also influenced the development of animal systems designed for *in-vitro* measurements [131].

10.10 Biomagnetic Instrumentation Concerns

In summary, when building or purchasing a SQUID system for biomagnetic measurements, in addition to cost, delivery time and the vendor's reputation, the following design areas must be considered:

- Number of Channels: How many are needed (be sure not to overestimate, cost is a function of channel number).
  Are multiple (multi-position) measurements acceptable (slower, but requires less channels) or must the measurement(s) be done in a single measurement?
- Signal-to-Noise: What is the sensitivity required? Should sensitivity be specified as minimum detectible changes in field (fT/√Hz) or current dipole (Am/√Hz)?
- Detection Coil Design: What are characteristics of source (current dipole, linear (*e.g.*, peripheral nerve), magnetic dipole, etc.)? This will indicate if single orientation (*e.g.*, B_z) or vector (*e.g.*, B_z, B_x, B_y) orientation detection coils are needed.
  What coil diameter will give the needed sensitivity?
  What coil layout (hexagonal, square, etc.) is best?
  What coil-to-coil spacing is needed?
- Magnetometer vs. Gradiometer: Does environmental noise require the use of gradiometers? If so, what style (axial vs. Planar), order and baseline is needed?
- Noise Reduction: What is the environmental noise? Have you accounted for ground loops, EMI, vibration (*e.g.*, nearby traffic, human or vehicle)?
  Will magnetic shielding be needed? If so, what type (MSR vs. eddy current room)?
  Will reference channels be used for Electronic Noise Cancellation? If so, will pre- or post-processing algorithms be used?
- Cryogenics:
  What is the needed coil-to-subject distance(s)?
  Is liquid helium suitable or is closed-cycle refrigeration required?
- Data Acquisition rates:
  At what rate is data to be gathered?
  What is the total amount of data to be gathered in a single session?
  Must the data be processed real-time?

How is the data to be interpreted?
How is the data to be displayed?
Will the data be correlated with other methodologies (*e.g.*, EEG, MRI, CT, ECG, PET)?

11 ACKNOWLEDGEMENTS

The author gratefully acknowledges helpful discussions with F. Bedard, John Clarke, Duane Crum, Michael Faley, the late Robin Giffard, Mark Kennedy, Larry Maltin, Winfried Möller, Jochen Mannhart, Marty Nisenoff, Doug Paulson, Stephen Robinson, Ray Sarwinski, Mike Simmonds, Bill Sutherling, Harold Weinstock, the late Sam Williamson and P.J. Zarecky.

12 REFERENCES

1 Ripka, P., Magnetic sensors and magnetometers , Boston: Artech, 2001

2 Kamerlingh-Onnes, H., *Akad. van Wetenschappen, Amsterdam*, **14:113**, 818 (1911)

3 Bardeen, J, Cooper, L.N. and Schrieffer, J.R., "Theory of Superconductivity", *Phys. Rev*. **108**, 1175-1204 (1957)

4 Bednorz, J. G. and Müller, K. A., "Possible high Tc superconductivity in the Ba-La-Cu-O system", *Z. Phys*., **B64**, 189-193 (1986)

5 Meissner, W. and Oschsenfeld, R., "Ein Neuer Effekt bei Eintritt der Supraleitfahigkeit, *Naturwissenschaften*, **21**, 787-788 (1933)

6 Quin, D.J. and Ittner, W.B., "Resistance in a Superconductor"*, J. Appl. Phys*., **33**, 748-749 (1962)

7 Feynman, R. P., Leighton, R. B. and Sands, M., "The Feynman Lectures on Physics", **III**, 21-10, Addison-Wesley, 1965

8 Josephson, B. D., "Possible new effect in superconductive tunneling," *Phys. Lett*., **1,** 251-253 (1962)

9 Faley, M.I., Poppe, U., Urban, K. Zimmerman, E, Glass., W., Halling, H., Bick, ,.Krause, H.-J , Paulson, D. N., Starr, T. and Fagaly, R. L. , "Operation of HTS dc-SQUID Sensors in High Magnetic Fields", *IEEE Trans. Appl. Superconductivity*, **9**, 3386-3391 (1999)

10 Tesche, C. D. and Clarke, J., "DC SQUID: noise and optimization," *J. Low Temp. Phys*,. **29**, 1982, pp. 301-331.

11 Giffard, R. P., Webb R. A., and Wheatley J. C., "Principles and Methods of Low-Frequency Electric and Magnetic Measurements Using an rf-Biased Point-Contact Superconducting Device," *J. Low Temp. Phys*., **6**, 533-610 (1972)

12 Van Duzer, T. and Turner, C. W., Principles of Superconductive Devices and Circuits, New York: Elsevier, 1981

13 Orlando, T. P. and Delin, K. A., Foundations of Applied Superconductivity, Reading, MA: Addison-Wesley, 1991

14 J. Clarke and A. I. Braginski, "The SQUID Handbook: Volume 1: Fundamentals and Technology of SQUIDs and SQUID Systems", Wiley, 2004

15 Stephens, R. B. and Fagaly, R. L., "High Temperature Superconductors for SQUID Detection Coils", *Cryogenics,* **31**, 988-992 (1991)

16 Koelle, D. , R. Kleiner, F. Ludwig, E. Dantsker, and J. Clarke, "High-transition-temperature superconducting quantum interference devices", *Rev. Mod Physics*, **71**, 631-686 (1999)

17 Ketchen, M. B. and Jaycox, J. M., "Ultra-low-noise tunnel junction dc SQUID with a tightly coupled planar input coil", *Appl. Phys. Lett*. **40**, 736-738 (1982)

18 Zimmerman, J.E., "Sensitivity enhancement of superconducting quantum interference devices through the use of fractional-turn loops", *J. Appl. Phys.* **42**, 4483-4487 (1971)

19 Zimmerman, J. E., Thiene, P. & Harding, J. T., "Design and operation of stable RF-biased superconducting point-contact quantum devices, and a note on properties of perfectly clean metal contacts", *J. Appl. Phys*. **41**, 1572–1580 (1970).

20 Clarke, J., "SQUID Fundamentals," In SQUID Sensors: Fundamentals, Fabrications and Applications, pp. 1-62, Weinstock, H. (ed.), Dordecht/Boston/London: Kluwer Academic Publishers, 1997

21 Drung, D, Cantor, R., Peters, M., Scheer, H.J. and Koch, H, "Low-noise high-speed dc superconducting quantum interference device magnetometer with simplified feedback electronics", *Appl. Phys. Lett*., **57**, 406 (1990)

22 LI, J., Lusher, C.P., Digby, M.E., Cowan, B., Saunders, J., Drung, D. and Schurig, T., "DC SQUID spectrometers for NMR", *J. Low. Temp. Phys*., **110**, 261-267 (1998)

23 Drung, D., "High-T_c and low-T_c dc SQUID electronics", *Supercond. Sci. Technol*., **16**, 1320-1336 (2003)

24 Hollenhorst, J.N. and Giffard, R.P., "High Sensitivity microwave SQUID", *IEEE Trans. Mag.*, **15**, 474-477 (1999)

25 SHE model 330X rf SQUID electronics

26 Quantum Design model 2000 rf SQUID electronics

27 Wakai, R.T. and Van Harlingen, D.J., "Signal and white noise properties of edge junction dc SQUID's", *Appl. Phys. Lett*. **52**, 1182-1184 (1988).

28 Schneider, C.W., Hammerl, G. Logvenov, G. Kopp, T. Kirtley, P.J. Hirschfeld, P.J., and Mannhart, J., "Half-h/2e Critical Current-Oscillations in SQUIDs", *Europhys. Lett*., **68**, 86-92 (2004)

29 Ohta, H., Matsui, T. and Uchikawa, T., "Whole-head SQUID System in a Superconducting Magnetic Shield", Proceedings of the 14th International Conference on Biomagnetism (Biomag2004), , pp. 634-635, Halgren, E., Ahlfors, S., Hämäläinen, M. and Cohen, D. (eds), Biomag 2004 Ltd., Boston, 2004

30 Simmonds, M. B. and Giffard, R. P., "Apparatus for reducing low frequency noise in dc biased SQUIDs.", United States Patent No. 4,389,612, 1983

31 John Clarke, personal communication

32 Ray Sarwinski, personal communication

33 Fagaly, R. L., "Superconducting magnetometers and instrumentation," *Sci. Prog., Oxford*, **71**, 1987, pp. 181-201.

34 Mück, M., Kycia, J.B., and Clarke, J., "Superconducting quantum interference device as a near-quantum-limited amplifier at 0.5 GHz", *Appl. Phys. Lett.*, **78**, 967-969 (2001)

35 Grover, F. W., Inductance Calculations, Working Formulas and Tables, New York: Dover, 1962

36 Simmonds, M.B., Fertig, W.A. and Giffard, R.P., "Performance of a Resonant Input SQUID Amplifier System", *IEEE Trans. Magn.* **MAG-15**, 478-481 (1979).

37 Wikswo, Jr., J. P., "Optimization of SQUID differential magnetometers', in Future Trends in Superconductive Electronics, Deaver BS, Falco CM, Harris JH, Wolf SA eds, AIP Conference Proceedings, **44**, pp. 145-149, New York: Am. Inst. Phys, 1978;

38 Ilmoniemi, R., Knuutila, J., Ryhänen, T. and Seppä, H., "Multi-SQUID devices and their applications," In Progress in Low Temperature Physics, **XII**, pp. 1-63, Brewer, D. F., (ed.), Amsterdam: Elsevier, 1989

39 Jaworski, F. B. and Crum, D. B., "Sources of gradiometer imbalance and useful balancing techniques", in SQUID Applications to Geophysics, pp. 19-25, Weinstock, H. and Overton, W. C. (eds.), Society of Exploration Geophysicists, Tulsa, OK, 1981

40 Vrba, J., "SQUID gradiometers in real environments," In SQUID Sensors: Fundamentals, Fabrications and Applications, pp. 117-178, Weinstock, H. (ed.), Dordecht/Boston/ London: Kluwer Academic Publishers, 1997

41 Ornelas, P.H., Bruno, A.C., Hall Barbosa, C., Andreade Lima, E., and Costa Ribeiro, P., "A survey of calibration procedures for SQUID gradiometers", *Supercond. Sci. Technol*., **16**, S427-S431 (2003)

42 D. E. Farrell, C. J. Allen, P. N. Arendt, S. R. Foltyn, D. N. Paulson, R. L. Fagaly and G. M. Brittenham, "High-Tc SQUID Susceptometer", *Bulletin of the American Physical Society*, **44**, 1553 (1999)

43 Robinson, S. E. "Environmental noise cancellation for biomagnetic measurements," in Advances in Biomagnetism, pp. 721-724, Williamson, S.J., Hoke, M., Stroink, G., and Kotani, M., eds., New York, Plenum Press, 1989

44 Wöltgens, P.J.M. and Koch, R.H., "Magnetic background noise cancellation in real-world environments", *Rev. Sci. Instrum.*, **71**, 1529-1533 (2000)

45 Timmerhaus, K.D. and Flynn, T.M., Cryogenic Process Engineering, Chapter 7, New York: Plenum Press, 1989

46 Lynam, P., Proctor, W. & Scurlock, R. G., "Reduction of the Evaporation Rate of Liquid Helium in Wide-necked Dewars", *Cryogenics*, **9**, 242-247 (1969)

47 Mathai, A., Song, D., Gim, Y., and Wellstood, F.C., "Magnetic microscopy using a liquid nitrogen cooled $YBa_2Cu_3O_7$ superconducting quantum interference device", *Applied Physics Letters* **61**, 598-600 (1992).

48 Buchanan, D. S., Paulson, D. N. and Williamson, S. J., "Instrumentation for clinical applications of neuromagnetism," In Advances in Cryogenic Engineering, 33, pp. 97-106, R. W. Fast, (ed.), New York: Plenum, 1988

49 Baudenbacher, F., Fong, L.E., Holzer, J.R., and Radparvar, M., "Monolithic low-transition-temperature superconducting magnetometers for high resolution imaging magnetic fields of room temperature samples", *App. Phys. Lett*, **82**, 3487-3489 (2003)

50 Walker, G, Miniature Refrigerators for Cryogenic Sensors and Cold Electronics, Oxford: Clarendon Press, 1989

51 Walker, G, Cryocoolers, Vols. 1 & 2, New York: Plenum Press, 1982

52 Wang, C. and Gifford, P.E., "Development of 4 K Pulse Tube Cryocoolers at Cryomech", in: *Advances in Cryogenic Engineering*, **47B**, 641-648 (2002)

53 Sata, K., "A Helmet-Shaped MEG Measurement System Cooled by a GM/JT Cryocooler," in Recent Advances in Biomagnetism, pp. 63-66, Yoshimoto, T., Kotani, M., Juriki, S., Karibe, H. and Nakasato, N., (eds.), Sendai, Tohoku University Press, 1999

54 Heiden, C., "Pulse tube refrigerators: a cooling option," In SQUID Sensors: Fundamentals, Fabrications and Applications, pp. 289-306, Weinstock, H. (ed.), Dordecht/Boston/London: Kluwer Academic Publishers, 1997

55 Romani, G-L., Williamson, S. J. , and Kaufman, L., "Biomagnetic instrumentation", *Rev. Sci. Instrum*., **53**, 1815-1845 (1982)

56 Hoburg, J.F., "Principles of quasistatic magnetic shielding with cylindrical and spherical shields", *IEEE Trans. Electromagnetic Compatibility,* **37**, 575-579 (1995)

57 Stroink, G., Blackford, B., Brown, B., and Horacek, M., "Aluminum shielded room for biomagnetic measurements", *Rev. Sci. Instrum.*, **52**, 463-468 (1981)

58 Cohen, D., "Large-volume conventional magnetic shields", *Rev de Physique Appliquee*, 53-58. (1970)

59 Cohen, D., Edelsack, E.A., and Zimmerman, J.E., "Magnetocardiograms taken inside a shielded room with a superconducting point-contact magnetometer", *Appl. Phys. Lett.,* 16*,* 278-280, (1970).

60 Cohen, D., Magnetoencephalography: detection of the brain's electrical activity with a superconducting magnetometer. *Science,* **175**, 64-66 (1972)

61 Bork, J., Hahlbohm, H.-D., R. Klein, R., and Schnabel, A., "The 8-layered magnetically shielded room of the PTB: Design and construction", In Biomag 2000, Proc. of the 12th International Conf. on Biomagnetism, pp 970-973

62 Baum, E. and Bork, J., "Systematic design of magnetic shields', *Journal of Magnetism and Magnetic Materials* **101**, 69-74 (1991)

63 "The definitive guide to magnetic shielding", Amuneal Corporation, Philadelphia, PA 19124

64 Claycomb, J.R. and Miller, J. H., "Superconducting magnetic shields for SQUID applications", *Rev. Sci. Instrum.*, **12**, 4562-4568 (1999)

65 Cohen, D., Schläpfer, U., Ahlfors, S., Hämäläinen, M., Halgren, E., "New Six-Layer Magnetically-Shielded Room for MEG",. Proceedings of the 13th International conference on biomagnetism; Nowak H. *et al*, eds., VDE Verlag GmbH, Berlin, 2002

66 H. Weinstock, personal communication. This is often referred to as Weinstock's law.

67 Kuchnir, M, McCarthy, J.D. and Rapidis, P.A., "SQUID Based Beam Current Monitor," *IEEE Trans. Magn.*, **MAG-21**, 1985, pp. 997-999.

68 Watanabe, T., Watanabe, S., Ikeda, T., Kase, M., Sasaki, Y. Kawaguchi, T. and Katayama, T., "Prototype of highly sensitive cryogenic current comparator with HTS SQUID and HTS magnetic shield", *Supercond. Sci. Technol*., **17**, S450-S455 (2004)

69 Fagaly, R. L., "Superconducting Sensors: Instruments and Applications", *Sensors*, **13**, 1996, pp. 18-27

70 Sarwinski, R. E., "Superconducting instrumentation", *Cryogenics*, **17**, 1977, pp. 671-679

71 Wikswo, J. P., "Improved instrumentation for measuring the magnetic fields of cellular action currents", *Rev. Sci. Inst.*, **53**, 1846-1850 (1982)

72 Lounasmaa, O., Experimental Principles and Methods below 1K, London, Academic Press, 1974

73 Levy, B. and Greenfield, A.J., "Constant-current supply of 3 ppm stability and resettability; application for a SQUID", *Rev. Sci. Instrum.*, **50**, 655-658 (1979)

74 Philo, JS and Fairbank, WM, "High-sensitivity magnetic susceptometer employing superconducting technology", *Rev. Sci. Instrum.,* **48** 1529-1536 (1977)

see also: Day, E.P., Kent, T.A., Lindahl, P.A., Munck, E., Orme-Johnson, W.H., Roder, H. and Roy, A., "SQUID measurement of metalloprotein magnetization. New methods applied to the nitrogenase proteins", *Biophysical Journal*, **52**, 837-853, (1987)

75 Model MPMS, Quantum Design, 6325 Lusk Boulevard, San Diego, CA 92121 USA

76 Amaya, K., Shimizu, K, Eremets, M.I., Kobayashi, T.C. and Endo, S., "Observation of pressure-induced superconductivity in the megabar region", *J. Phys.: Condens. Matter*., **10**, 11179-11190 (1998)

77 McElfresh, M., "Fundamentals of Magnetism and Magnetic Measurements", Quantum Design Technical Document, http://www.qdusa.com/resources/techdocs.html (1994)

78 Foner, S., "Versatile and sensitive vibrating-sample magnetometer", *Rev. Sci. Instrum.*, **30**, 548-557 (1959)

79 Pelizzione, M. and Teyvaud, A., "A SQUID Susceptometer for Fields up to 8.5 Tesla", *Applied Physics*, **24**, 375-379 (1981)

80 Webb, R. A., "New technique of improved low-temperature SQUID NMR measurements", *Rev. Sci. Instrum.*, **48**, 1585-1594 (1977)

81 Hilbert, C., Clarke, J., Sleator, T. and Hahn, E.L. "Nuclear quadrupole resonance detected at 30 MHz with a dc superconducting quantum interference device", *Appl. Phys. Lett.*, **47**, 637-639 (1985)

82 Klemme, B.J., Adriaans, M.J., Day, P.K., Sergatskov, D.A., Aselage, T.L. and Duncan, R.V., "PdMn and PdFe: New Materials for Temperature measurement near 2 K", *J. Low Temp. Phys.*, **116**, 133-146 (1999)

83 Solomonson, N., Hamilton, W.O., Johnson, W. and Xu, B., "Construction and performance of a low noise inductive transducer for the Louisiana State University gravitational wave detector", *Rev. Sci. Instrum.* **65**, 174-181 (1977)

84 Lockhart, J.M, Muhlfelder, B. *et al*., "Optimization of a SQUID System for Space," *IEEE Trans. Appl. Supercon*., **7**, 2354 (1997). *A discussion of the SQUID readout and superconducting shielding can be found in:* Lockhart, J.M., "SQUID Readout and Ultra-Low Magnetic Fields for Gravity Probe-B (GP-B)", *SPIE Proceedings*, **619**, 148 (1986)

85 D. S. Akerib, *et al* (CDMS Collaboration), "First results from the cryogenic dark matter search in the Soudan underground laboratory", *Phys. Rev. Lett.* **93**, 211301 (2004).

86 Bradley, R., Clarke, J., Kinion, D., Rosenberg, L.J., van Bibber, K., Matsuki, S., Mück, M., and Sikivie, P., "Microwave cavity searches for dark-matter axions". *Rev. Mod. Phys.*, **75**, 777-817 (2003)

87 Cabrera, B., "First results from a superconductive device for moving magnetic monopoles", *Phys. Rev. Lett*., **48**, 1378 (1982)

88 Hebard, A.F and Fairbank, W.M, in *Proceedings of the Twelfth International Conference of Low Temperature Physics* (Keigaku Publishing Co., Tokyo, 1971), 855; see also: Jones, L. W., "A review of quark search experiments", *Rev. Mod. Phys.,* **49**, 717–752 (1977)

89 Mück, M. and Clarke, J., "Flux-bias stabilization scheme for a radioastronomy amplified based on a superconducting quantum interference device", *Rev. Sci. Instrum.*, **72**, 3691-3693 (2001)

90 Oppenländer, J., Häussler, Ch., Träuble, T., and Schopohl, N., "Highly sensitive magnetometers for absolute magnetic field measurements based on quantum interference filters", *Physica C*, **368**, 119-124 (2002)

91 Kaufman, A.A. and Keller, G.V., The Magnetotelluric Sounding Method, (Elsevier, New York, 1981)

92 Ander, M.E., Goss, R., Strangway, D., Hillebrand, C., Laughlin, A.W., and Cassandra, H., "Magnetotelluric/audiomagnetotellurics study of the Zuni hot dry rock geothermal prospect, New Mexico", in Geothermal: Energy for the Eighties, *Geothermal Resources Council Transactions*, **4**, 5-8 (1980)

93 Gamble, T.D., Goubau, W.M. and Clarke, J., "Magnetotellurics with a remote magnetic reference", *Geophysics*, **37**, 98-114 (1979)

94 Wynn, W., Frahm, C., Carroll, P., Clark, R. Welhoner, J. and Wynn, M., "Advanced Superconducting Gradiometer/Magnetometer Arrays and a Novel Signal Processing Technique", *IEEE Trans. Magn.*, **11**, pp. 701-707. (1975)

95 Clem, T.R., KeKelis, G.J., Lathrop, J.D., Overway, D.J., and Wynn, W., "Superconducting magnetic gradiometers for mobile applications with an emphasis on ordnance detection", In SQUID Sensors: Fundamentals, Fabrications and Applications, pp. 517-586, Weinstock, H. (ed.), Dordecht/Boston/London: Kluwer Academic Publishers, 1997

96 Wold, R., Weichman, P., Tondra, M., Lange, E., Nordman, C., Paulson, D., Starr, T., Johnson, J., Wilkinson, D., "Development of a standoff UXO detection system using SDT and high temperature SQUID sensor arrays." UXO Forum '2000, Anaheim, May, 2000.

97 Panatov, G., Bick, M., Zhang, Y., and Krause, H-J., "Effect of repetitive transmitter signals on SQUID response in Geophysical TEM" *IEEE Trans. Appl. Superconductivity*, **11**, 888-891 (2001)

98 Zakosarenko, V., Chwala, A. Ramos, J., Stolz, R., Schultze, V. Lütjen, H., Blume, J. and Schüler, T., "HTS dc SQUID systems for geophysical prospection", *IEEE Trans. Appl. Superconductivity*, **11**, 896-899 (2001)

99 Foley C P, Leslie K E, Binks R, Lewis C, Murray W, Sloggett G J, Lam S, Sankrithyan B, Savvides N, Katzaros A, Muller K H, Mitchell E E, Pollock J, Lee J, Dart D L, Barrow R R, Asten M, Maddever A, Panjkovic G, Downey M, Hoffman C, and Turner R, "Field trials using HTS SQUID magnetometers for ground-based and airborne geophysical applications", *IEEE Trans. Appl. Supercond*. **9**, 3786-3792 (1999)

see also: Leslie, K E, Binks R, Foley C P, Thorn, R.G., Roberts, M.J., Du, J., Mitchell E.E., Lam S.K.H., Lewis, C.J., Millar, C., and Osmond, R.T., "Operation of a Geophysical HTS SQUID system in Sub-Artic Environments", *IEEE Trans. Appl. Supercond*. **13**, 759-762 (2003)

100 Leslie, K.E.; Binks, R.A.; Lewis, C.J.; Scott, M.D.; Tilbrook, D.L.; Du, J.; "Three component spinner magnetometer featuring rapid measurement times", *IEEE Trans. Appl. Superconductivity*, **11**, 252-255 (2001)

101 Weiss, B.P., Kirschvink, J.L., Baudenbacher, F.J., Vali, H., Peters, N.T., Macdonald, F.A., Wikswo, J.P., "A low temperature transfer of ALH84001 from Mars to Earth", *Science*, **290**, 791-795 (2000)

102 Ma, Y.P. and Wikswo, J.P., "SQUID Magnetometers for Depth-selective, Oriented Eddy Current Imaging", *Review of Progress in Quantitative Nondestructive Evaluation*, **17**, 1067-1074 (1998)

103 Unpublished data, http://www.inel.gov/env-energyscience/materials/telschow/squid.shtml, courtesy, K. Telschow

104 Fagaly, R. L., "SQUID Detection of Electronic Circuits," *IEEE Trans. Magn.*, **MAG-25**, 1216-1218 (1989)

105 Kirtley, J., "Imaging magnetic fields," *IEEE Spectrum*, **33**, 40-48 (1996)

106 Jenks, W. G., Sadeghi, S. S. H., and Wikswo, J.P., "SQUIDs for nondestructive evaluation", *J. Phys. D: Appl. Phys*., **30**, 293-323 (1997)

107 Anderberg, J., Cloclough, M., Crum, D.B., Paulson, D.N. and Fagaly, R.L., "Scanning SQUID Microscope with Micron Resolution", *IEEE Trans. Appl. Superconductivity*, **13**, 231-234 (2003)

108 Wikswo, J. P., "High-resolution measurements of biomagnetic fields", In Advances in Cryogenic Engineering, **33**, pp. 107-116, R. W. Fast, (ed.), New York: Plenum, 1988

109 Gerber, Ch., Hilgenkamp, H., and Mannhart, J., "Apparatus for Use in Magnetic-Field Detection and Generation Devices", US Patent 6,211,673 B1 (3. 4. 2001).

110 Schambach, J, Warzemann, L, Weber, P, Kötitz, R, and Weitschies, W, "SQUID gradiometer measurement system for magnetorelaxometry in a disturbed environment", *IEEE Trans. Appl. Superconductivity,* **9**, 3527-3530 (1999)

111 Fagaly, R. L., "Neuromagnetic Instrumentation", In Advances in Neurology, **54**: Magnetoencephalography, pp. 11-32, Sato, S. (ed.), New York: Raven Press, 1990

112 Williamson S. J. and Kaufman L., Biomagnetism", *J. Magn. Mag. Mat*. **22**, 129-202 (1981)

113 Kado, H., Ogata, H., Haruta, Y., Higuchi, M., Shimogawara, M., Kawai, J., Adachi, Y., Bertrand, C. and Uehara, G., "The imaging of a magnetic source", in Biological Imaging and Sensing, pp. 117-204, T.Furukawa, Ed., Berlin-Heidelberg-New York: Springer, 2004

114 Robinson, S. E. and Fagaly, R. L., "Biomagnetic Instrumentation: Current Capabilities & Future Trends", *Proc. ASME*, **AES-9**, 7-12 (1989)

115 Knuutila, J., Ahlfors, S., Ahohen, A., Hällström, J., Kajola, M, Lounasmaa, O.V., Vilkman, V, and Tesche, C., "Large-area low-noise seven-channel dc SQUID magnetometer for brain research", *Rev. Sci. Instrum*., **58**, 2145-2156 (1987)

116 Sato, S. Magnetoencephalography: Comparison with Electroencephalography and Clinical Applications, Advances in Neurology, **54**, Raven Press, New York 1990

117 Robinson, S.E. and Vrba, J., "Functional Neuroimaging by Synthetic Aperture Magnetometry (SAM)," in Recent Advances in Biomagnetism, pp. 302-305, Yoshimoto, T., Kotani, M., Juriki, S., Karibe, H. and Nakasato, N., (eds.), Sendai, Tohoku University Press, 1999

118 Okada, Y., Atwood, C., Pratt, K and Paulson, D., "BabySQUID®: A High-Resolution, Mobile, Multichannel MEG System for Neonatal Brain Assessment", Proc. 14th Intl. Conf. on Biomagnetism, Boston, 2004

119 Engelhardt, R., Fung, E.B., Kelly, P., Biehl, T.R., Pakbaz, Z., Nielsen, P., Harmatz, P. And Fischer, R., "Interaction of Artificial Metallic Objects with Biosusceptometric Measurements", *Neurology and Clinical Neurophysiolog*, **32**, 1-4 (2004)

120 Brisinda D., Meloni A.M., and Fenici R., "Magnetocardiographic Study of Ventricular Repolarization in Hypertensive Patients with and without Left Ventricular Hypertrophy", Proc. 14th Intl. Conf. on Biomagnetism, 389-390, Boston, 2004

121 Hashimoto, I., Mashiko, T., Mizuta, T., Imada, T., Iwase, K., and Okazaki, H., "Visualization of moving quadrupole with magnetic measurements of peripheral nerve action fields", *Electroencephalogr. Clin. Neurophysiol*., **93**, 459-467 (1997)

122 Bradshaw, L.A., Ladipo, J.K., Staton, D.J., Wikswo, J.P. Jr., and Richards, W.O., "The Human Vector Magnetogastrogram and Magnetoenterogram", *IEEE Transactions on Biomedical Engineering*, **46**, 959-970 (1999)

123 Brittenham, G.M., Farrell, D.E., Harris, J.W., Feldman, E.S., Danish, E.H., Muir, W.A., Tripp, J.H., Bellon, E.M., "Magnetic-Susceptibility of Human Iron Stores", *New England Journal of Medicine,* **307,** 1671 (1982)

124 Bastuscheck, C.M. and Williamson, S.J., "Technique for measuring the ac susceptibility of portions of the human body or other large objects", *J. Appl. Phys.*, **58**, 3896-3906 (1985)

125 Cohen, D., Arai, S. F., and Brain, J. D., "Smoking impairs long-term dust clearance from the lung", Science 204, 514-517(1979)

126 Möller, W., Barth, W., Kohlhäufl, M., Häussinger, K., Stahlhofen, W., and Heyder, J., "Human alveolar long-term clearance of ferromagnetic iron-oxide microparticles in healthy and diseased subjects", *Exp. Lung Res*. **27**, 547-568 (2001)

127 Heyder, J., "Mucociliary and long-term particle clearance in the airways of healthy non-smokers", *J. Appl. Physiol*. **97**, 2200-2206 (2004)

128 Stahlhofen, W. and Möller, W., "Behaviour of magnetic micro-particles in the human lung", Radiat. Environ. Biophys. **32**, 221-238 (1993).

129 Möller, W., Kreyling, W. G., Kohlhäufl, M., Häussinger, K., and Heyder, J., "Macrophage functions measured by magnetic microparticles in vivo and in vitro*", J. Magn. Magn. Mater.* **225**, 218-225 (2001)

130 Wikswo, J.P. Jr, "High-resolution Magnetic Imaging: Cellular Action Currents and other Applications", in SQUID Sensors: Fundamentals, Fabrication and Applications, H. Weinstock, Ed., (Kluwer Academic Publishers, The Netherlands), 307-360 (1996)

131 Baudenbacher, F., Peters, N. T., Baudenbacher, P., Wikswo, J. P., "High Resolution Imaging of Biomagnetic Fields Generated by Action Currents in Cardiac Tissue using a LTS-SQUID microscope", *Physica **C*** **368**, 24-31 (2002